Lattice dynamics of γ-Ce

by

Theresa Ann Gould

A Thesis Submitted to the

Graduate Faculty in Partial Fulfillment of

The Requirements for the Degree of

MASTER OF SCIENCE

Department: Physics

Major: Solid State Physics

Iowa State University
Ames, Iowa

1978

TABLE OF CONTENTS

CHAPTER I. INTRODUCTION

Properties of Cerium

Cerium metal exists in five established allotropic forms under various temperature and pressure conditions (1). These allotropic forms are designated as α, β, γ, δ, and α'. The α' phase exists only at pressures greater than 50 kb (2), and the δ phase exists only near the melting temperature, 1072°K (3). Therefore the α, β, and γ phases are those most frequently encountered under common experimental conditions. Initial structure studies of cerium indicated that both face-centered cubic (fcc) and hexagonal close-packed (hcp) phases existed at room temperature and ambient pressure (4). The fcc structure was confirmed by subsequent studies and is currently identified as γ-Ce. (See Table 1.1 for additional crystallographic data.) The α phase was identified next both at room temperature and moderate pressure (5), and at low temperature and atmospheric pressure (6). This phase was found to be a collapsed fcc structure with a volume decreased by nearly 17% from that of γ-Ce. β-Ce was the last of the common allotropes to be identified (7). This phase has a double-hexagonal close-packed (dhcp) structure.

The transformation behavior of cerium hampered experimental investigation for many years. β-Ce forms from γ-Ce as the sample is cooled below 250°K. This transformation is incomplete and impurity dependent, however, and at 116°K the remaining γ-Ce in the sample transforms to α-Ce. Further cooling will cause the β-Ce portion to be partially transformed into α-Ce. The fractions of α and β cerium in a specimen at low temperature depends largely on the cooling rate and the thermal

Table 1.1. Properties of cerium

Atomic Mass		140.12 amu
Lattice Parameters		
α-Ce[a] (8)	fcc	a = 4.824 Å
β-Ce (9)	dhcp	a = 3.6810 Å
		b = 11.857 Å
γ-Ce (9)	fcc	a = 5.1610 Å
Thermal Neutron Data (10)		
Nuclear Scattering Length		$b = .48 \times 10^{-12}$ cm
Nuclear Cross Sections		$\sigma_{coh} = 2.7 \times 10^{-24}$ cm^2
		$\sigma_{incoh} = 0.01 \times 10^{-24}$ cm^2
		$\sigma_{abs} = .48 \times 10^{-24}$ cm^2

[a]Value given is room temperature, high pressure data.

and mechanical history of the sample (1,7,11). There is also large hysteresis in the transition temperatures during a thermal cycle. During warming the β phase does not completely transform to γ-Ce until a temperature of ∿500°K is attained (12,13,14).

Due to these allotropic transformation properties many early experiments were performed on samples containing mixed phases. Care must be taken in interpretation of the results, particularly when the sample was subjected to thermal cycling. This point will be explored more fully in Chapter III in the comparison of the present results to the results of former experiments.

Recent measurements performed on pure phases are more reliable. A cerium sample which has not previously been cooled below the β transition temperature will contain only the γ phase. Methods have also been developed for the preparation of allotropically pure α and β cerium (15,16).

Reliable measurements of the properties of the cerium allotropes are of interest in their own right, but much of the experimental work has been motivated by the intriguing isostructural α-γ transformation. The first explanation given by Zachariasen and Pauling (quoted in Reference 5 and 6, respectively) invoked a simple transfer of the localized 4f electron into the valence band to produce the observed volume collapse. Thus, one would expect to find a valence of three in γ-Ce and four in α-Ce. Later work by numerous investigators suggested various fractional valences for the two phases. In an extensive survey of all available data made in 1963 it was concluded that at ambient pressure valences of

3.06 for γ-Ce and 3.67 for α-Ce were most consistent with the data (17). It should be noted, however, that large inconsistencies exist, particularly with regard to more recent positron annihilation measurements (18). Apparently the electronic structure of cerium is too complicated to be described well by a simple valence scheme.

Neutron Scattering

When large single crystals of γ-Ce were successfully prepared at Ames Laboratory (19) it provided an opportunity to study this allotrope using neutron scattering. Various neutron scattering techniques yield a variety of valuable information. Elastic nuclear scattering provides structural information. Inelastic nuclear scattering yields the spectrum of lattice vibrations. The neutron possesses an intrinsic magnetic moment and is therefore subject to magnetic scattering also.

Magnetic scattering of neutrons is fundamentally different from nuclear scattering. In magnetic scattering the neutron scatters from the localized electrons of the atoms. Since the electron cloud is of the same order of magnitude as the neutron wavelength, interference effects in the scattering region occur. This gives rise to an observable form factor governing magnetic scattering. Magnetic excitations can be studied using inelastic magnetic scattering. (Nuclear and magnetic inelastic neutron scattering are discussed further in Chapter II). In some materials magnetic ordering gives rise to a "magnetic lattice structure" which can be determined from magnetic elastic scattering.

Polarized neutron scattering identifies the magnetic contribution to elastic scattering. From these measurements the magnetic form factor

and the magnetic susceptibility due to the localized electrons can be calculated.

Recent polarized neutron scattering measurements on γ-Ce (20) have shown the scattering to be of a 4-f nature, indicating that the 4-f electron is localized in this allotrope. However, comparison of the calculated susceptibility to bulk susceptibility measurements indicates that there may be a partial delocalization of the 4-f electron even in the γ-phase (21).

The dynamical properties of a lattice can be studied using inelastic nuclear scattering. This technique yields the lattice vibrational spectrum and the elastic constants. From the observed spectrum one obtains the interatomic force constants from which various elastic and thermodynamic properties can be calculated. In addition, insight into structural transformations can be obtained since these transformations are intimately related to interatomic forces. Therefore, one would expect the vibrational spectrum of γ-Ce to provide insight into the α-γ transformation.

Given the preceding rationale, the present study was undertaken. The main thrust of the work was geared to obtaining the lattice vibrational spectrum as well as information regarding the magnetic excitations of γ-Ce using inelastic scattering techniques. A brief review of the elementary fundamentals of lattice dynamics is given below. Chapter II deals with basic principles of inelastic neutron scattering and the details of the experiment. Chapter III presents analysis and discussion of the experimental results.

Review of Lattice Dynamics

Lattice dynamical studies allow prediction of macroscopic physical properties of a solid in terms of microscopic models. These models are based on the observed thermal vibration spectrum of the crystal lattice. For the most intuitive picture, one may regard phonons[1] as normal modes of the vibrating lattice. Thermal neutron scattering is ideal for studying the frequency spectrum because the energies of the neutrons and phonons are of the same order of magnitude. Therefore, creation or annihilation of a phonon by a neutron produces a change in neutron energy which is easily measurable. The change in direction of the scattered neutron gives the momentum transfer. Knowledge of the frequency and momentum of the phonons allows construction of the phonon dispersion relation from which the interatomic forces can be calculated.

The phenomenological approach to the theory of lattice dynamics is to set up and solve the equations of motion of a vibrating lattice. In the original theory formulated by Born and Huang (22) the adiabatic approximation was invoked with ionic crystals in mind. The approximation states that since the frequency of motion of the electrons is much faster than the frequency of motion of the vibration of the ions, the electrons may be assumed to follow the nuclear motion "adiabatically". In other words the electron state is deformed smoothly as the nuclei move and the electrons do not make transitions from one state to another. Thus the

---

[1] A phonon is defined as a quantum of energy in a vibrational wave in a lattice. It has become commonplace to refer to the wave itself using the same term.

effective potential for the motion of the nuclei depends only on the instantaneous nuclear coordinates and contains the energy of the electrons explicitly. The electrons do not individually participate in the propagation of a lattice wave but serve as a medium through which the internuclear forces are exerted. The application of the adiabatic approximation to metals has been questioned since the electronic ground states in metals form a quasi-continuum and nuclear and electronic motions will be coupled. However, a quantum mechanical analysis reveals that "non-adiabatic" terms can be safely neglected (23,24). Therefore, a standard Born-von Kármán analysis has been applied in the current work and will be briefly reviewed below.

For a given crystal, if the origin of the coordinate system is the equilibrium position of one of the atoms, then the equilibrium position of the origin of the ℓ-th primitive cell is given by

$$\vec{R}(\ell) = \ell_1\vec{a}_1 + \ell_2\vec{a}_2 + \ell_3\vec{a}_3 \qquad (1.1)$$

with the ℓ_i's integers and the a_i's primitive translation vectors. $\vec{R}(k)$ gives the equilibrium position of the k-th atom in the ℓ-th primitive cell. Therefore, the total vector from the origin to a given atom in the lattice is

$$\vec{R}(\ell, k) = \vec{R}(\ell) + \vec{R}(k) \quad . \qquad (1.2)$$

The displacement of an atom from its equilibrium position is given by $\vec{U}(\ell, k)$. The total kinetic energy of the crystal is therefore,

$$T = \tfrac{1}{2} \sum_{\ell} \sum_{k} \sum_{\alpha} M_s \dot{U}_\alpha^2(\ell, k) \quad , \tag{1.3}$$

where α denotes the x, y and z components of $\vec{U}(\ell, k)$.

Within the context of the adiabatic approximation the total potential energy of the crystal is assumed to be a function of the instantaneous positions of all the atoms. In most cases of interest it is safe to assume that the atomic displacements $\vec{U}(\ell, k)$ are small compared to the lattice spacing. Therefore, the potential energy, Φ, can be expanded in a Taylor's series of $\vec{U}(\ell, k)$.

$$\begin{aligned} \Phi &= \varphi_0 + \varphi_1 + \varphi_2 + \varphi_3 + \ldots \text{ (higher order terms)} \\ &= \varphi_0 + \sum_{\ell} \sum_{k} \sum_{\alpha} \varphi_\alpha(\ell, k) U_\alpha(\ell, k) + \tfrac{1}{2} \sum_{\ell,\ell'} \sum_{k,k'} \sum_{\alpha,\beta} \varphi_{\alpha\beta}(\ell k, \ell' k') \\ &\quad \times U_\alpha(\ell, k) U_\beta(\ell', k') + \ldots \end{aligned} \tag{1.4}$$

where

$$\varphi_\alpha(\ell, k) = \left. \frac{\partial \Phi}{\partial U_\alpha(\ell, k)} \right|_0 \tag{1.5}$$

$$\varphi_{\alpha\beta}(\ell k, \ell' k') = \left. \frac{\partial^2 \Phi}{\partial U_\alpha(\ell, k) \partial U_\beta(\ell', k')} \right|_0 \quad . \tag{1.6}$$

The first term in Equation (1.4) is an energy reference level and may be taken as zero. The second term also vanishes because the displacements are taken about equilibrium lattice positions. Therefore,

$$\left. \frac{\partial \Phi}{\partial U_\alpha(\ell, k)} \right|_0 = 0 \quad . \tag{1.7}$$

All the remaining terms are finite and non-vanishing but in the harmonic approximation only φ_2 is retained. Anharmonic effects arising from higher order terms do exist in crystals but they are usually small enough to be neglected. These effects produce a finite phonon lifetime thereby broadening the one phonon peak (25). Anharmonic effects also shift the position of the peak slightly, usually to lower frequency (26). In some rare gas solids the vibrational displacement of the atoms is nearly half the interatomic distance. Anharmonic effects are large in such cases (27). However, under the conditions of the present experiment the harmonic approximation can be applied.

The system is assumed to be conservative so that the Hamiltonian operator, H_{op}, may be equated to the total energy function.

$$H_{op} \rightarrow H = T + \Phi \tag{1.8}$$

$$H = \tfrac{1}{2} \sum_{\ell} \sum_{k} \sum_{\alpha} M_k \dot{U}_\alpha^2(\ell, k) + \tfrac{1}{2} \sum_{\ell,\ell'} \sum_{k,k'} \sum_{\alpha,\beta} \varphi_{\alpha\beta}(\ell k, \ell' k') \times U_\alpha(\ell, k) U_\beta(\ell', k') \quad .$$

The α component of the force acting on atom (ℓ, k) is given by

$$F_\alpha = \dot{P}_\alpha = - \frac{\partial H}{\partial U_\alpha(\ell, k)} \quad , \tag{1.9}$$

where P_α is the momentum equal to $M_k \dot{U}_\alpha(\ell, k)$. Thus the equations of motion for a vibrating lattice are given by

$$F_\alpha = M_k \ddot{U}_\alpha(\ell, k) = - \sum_{\ell'} \sum_{k'} \sum_{\beta} \varphi_{\alpha\beta}(\ell k, \ell' k') U_\beta(\ell', k') \quad . \tag{1.10}$$

The $\varphi_{\alpha\beta}$ are called interatomic force constants by analogy with the classical harmonic oscillator spring constants.

Since translational invariance must be satisfied, the potential cannot be affected by the displacement of every atom by the same amount, U. In other words the entire body of material is moved as a unit. This corresponds to a phonon with wave vector $\vec{q} = 0$ (i.e., infinite wavelength). For this kind of displacement the sum of the forces on every atom must be zero.

$$0 = \left[\sum_{\ell'} \sum_{k'} \varphi_{\alpha\beta}(\ell k, \ell' k') U(\ell', k')\right]_{\vec{q}=0} \quad . \tag{1.11}$$

$$0 = \left[(\varphi_{\alpha\beta}(\ell k, \ell k) + \sum_{\ell' \neq \ell} \sum_{k \neq k'} \varphi_{\alpha\beta}(\ell \ell', k k') U(\ell', k')\right]_{\vec{q}=0} \quad . \tag{1.12}$$

Therefore, one obtains

$$\varphi_{\alpha\beta}(\ell k, \ell k) = - \sum_{\ell' \neq \ell} \sum_{k' \neq k} \varphi_{\alpha\beta}(\ell k, \ell' k') \quad . \tag{1.13}$$

The "self force constant", $\varphi_{\alpha\beta}(\ell k, \ell k)$, is given by the negative of the sum of the force constants describing the forces acting on atom (ℓ, k) due to every other atom in the lattice.

Another constraint arises from rotational invariance. The potential will not be affected if the entire crystal is subjected to an infinitesimal rotation.

An infinitesimal rotation can be expressed by a vector

$$\vec{\theta} = \vec{\theta}_x + \vec{\theta}_y + \vec{\theta}_z \quad . \tag{1.14}$$

$\vec{\theta}_\alpha$ is a unit vector directed along the α axis and represents an infinitesimal rotation about the α axis. The displacement, $\vec{U}(\ell, k)$, generated

by such a rotation acting on a position vector, $\vec{R}(\ell, k)$, is perpendicular to both $\vec{R}(\ell, k)$ and $\vec{\theta}_\alpha$. It is perpendicular to $\vec{\theta}_\alpha$ because α is the axis about which the rotation is performed and $\vec{\theta}_\alpha$ is directed along that axis. It is perpendicular to $\vec{R}(\ell, k)$ because it is an infinitesimal rotation. A finite rotation would cause $\vec{R}(\ell, k)$ to sweep out a circular arc. An infinitesimal rotation produces a displacement tangent to this arc. Hence, the displacement is perpendicular to $\vec{R}(\ell, k)$.

Thus, the displacement produced by an infinitesimal rotation can be represented by a cross product.

$$U(\ell, k) = [\vec{\theta} \times \vec{R}(\ell, k)] \quad . \tag{1.15}$$

Consider a rotation about the x axis. Then,

$$\begin{aligned} U(\ell, k) &= \vec{\theta}_x \times \vec{R}(\ell, k) \\ &= \theta_x R_y(\ell, k)\hat{z} - \theta_x R_z(\ell, k)\hat{y} \quad . \end{aligned} \tag{1.16}$$

The θ_α's are unit vectors and therefore have a magnitude equal to unity. This displacement becomes

$$U(\ell, k) = R_y(\ell, k)\hat{z} - R_z(\ell, k)\hat{y} \quad . \tag{1.17}$$

Substituting into Equation (1.10) yields

$$0 = - \sum_{\ell'} \sum_{k'} \varphi_{\alpha z}(\ell k, \ell' k') R_y(\ell, k) - \varphi_{\alpha y}(\ell k, \ell' k') R_z(\ell, k) \tag{1.18}$$

for an infinitesimal rotation about the x axis. Since the crystal is undistorted there are no restoring forces and the expression is set equal to zero. Similar constraints arise from rotations about the y and z axes. All of these terms may be expressed compactly by using the

Levi-Civita symbol $\varepsilon_{\alpha\beta\gamma}$ defined as follows:

$\varepsilon_{\alpha\beta\gamma}$ = 0 if any two Cartesian indices α, β, γ are zero;

= 1 if (α, β, γ) are a cyclic permutation of x, y, z;

= -1 otherwise.

Using this notation Equation (1.18) may be generalized to

$$0 = \sum_{\ell'} \sum_{k'} \sum_{\mu} \sum_{\nu} \varphi_{\alpha\nu}(\ell k, \ell' k') R_{\mu}(\ell', k') \varepsilon_{\beta\mu\nu} \tag{1.19}$$

for all α, β, and k.

The force equation, which is subject to the two invariance constraints discussed above, has plane wave solutions of the form

$$U_{\alpha}(\ell, k) = e_{k,\alpha}(\vec{q}) e^{i[\vec{q}\cdot\vec{R}(\ell, k) - \omega t]} \tag{1.20}$$

where $\vec{q}$ is the phonon wave vector. Substituting into Equation (1.10) one obtains

$$M_k \omega^2 e_{k,\alpha}(\vec{q}) = \sum_{\ell'} \sum_{k'} \sum_{\beta} \varphi_{\alpha\beta}(\ell k, \ell' k') e^{-i\vec{q}\cdot[\vec{R}(\ell, k) - \vec{R}(\ell', k')]} e_{k',\beta}(\vec{q}) \tag{1.21}$$

Equation (1.21) may be rewritten as

$$M_k \omega^2 e_{k,\alpha}(\vec{q}) = \sum_{k'} \sum_{\beta} D_{\alpha\beta}^{kk'}(\vec{q}) e_{k',\beta}(\vec{q}) \quad , \tag{1.22}$$

where

$$D_{\alpha\beta}^{kk'}(\vec{q}) = \sum_{\ell'} \varphi_{\alpha\beta}(\ell k, \ell' k') e^{-\vec{q}\cdot[\vec{R}(\ell, k) - \vec{R}(\ell', k')]} \tag{1.23}$$

and is called the dynamical matrix.

Notice that $D^{k,k'}_{\alpha,\beta}(\vec{q})$ is independent of ℓ because the ℓ dependence in $\Phi_{\alpha\beta}(\ell k, \ell' k')$ appears only as a difference, $\vec{R}(\ell) - \vec{R}(\ell')$. Therefore, the frequency solutions to the equation of motion are periodic functions of $\vec{q}$, and all unique normal mode frequencies may be found by using a reduced set of wave vectors. This reduced set define a region of $\vec{q}$ space around $\vec{q} = 0$ called the reduced Brillioun zone (28).

Equation (1.22) is a set of 3n linear homogeneous equations in 3n unknowns, where n is the number of atoms in a primitive cell. To obtain a non-trivial solution

$$\det \left| D^{kk'}_{\alpha\beta}(\vec{q}) - M_s \omega^2 \delta_{\alpha\beta} \delta_{kk'} \right| = 0 \quad . \tag{1.24}$$

Solving the secular equation yields 3n eigenfrequencies of vibration,

$$\omega = \omega_j(\vec{q}) \qquad j = 1, 2, 3, \ldots, 3n \tag{1.25}$$

and 3n accompanying eigenvectors,

$$e_{k',\beta}(\vec{q}, j) \quad . \qquad j = 1, 2, 3, \ldots, 3n \tag{1.26}$$

These eigenvectors must satisfy orthogonality,

$$\sum_k \sum_\alpha e^*_{k,\alpha}(\vec{q}, j) e_{k,\alpha}(\vec{q}, j') = \delta_{jj'} \tag{1.27}$$

and closure

$$\sum_j e^*_{k',\beta}(\vec{q}, j) e_{k,\alpha}(\vec{q}, j) = \delta_{\alpha\beta} \delta_{kk'} \quad . \tag{1.28}$$

The equation of motion [Equation (1.22)] together with the definition of the dynamical matrix [Equation (1.23)] is the formal

statement of the Born-von Kármán theory of lattice dynamics. These equations may be specialized for the monatomic case of the present study. The primitive fcc lattice has only one atom per unit cell (see Figure 1.1). $\vec{R}(\ell)$, given by Equation (1.1) is sufficient to describe the location of every atom in the lattice. Therefore, throughout the preceding development the k and k' indices may be omitted. The equation of motion becomes

$$M_s \omega^2 e_\alpha(\vec{q}) = \sum_\beta D_{\alpha\beta}(\vec{q}) e_\beta(\vec{q}) \quad , \tag{1.29}$$

and the dynamical matrix is now given by

$$D_{\alpha\beta}(\vec{q}) = \sum_{\ell'} \varphi_{\alpha\beta}(\ell, \ell') e^{-i\vec{q}\cdot[\vec{R}(\ell)-\vec{R}(\ell')]} \quad . \tag{1.30}$$

Solving the secular equation yields three eigenfrequencies,

$$\omega = \omega_j(\vec{q}) \qquad j = 1, 2, 3 \tag{1.31}$$

and three eigenvectors,

$$e_\alpha(\vec{q}, j) \quad . \qquad j = 1, 2, 3 \tag{1.32}$$

In principle one can calculate the frequencies of all the normal modes of the lattice if the interatomic force constants are known. The number of independent force constants is significantly reduced by the symmetry of the crystal. Specifying the interaction to be of a given type, such as axially symmetric, places additional constraints on the force constants. In spite of the simplifications introduced by symmetry, for practical calculations the number of force constants must be

limited in some way. Usually practical calculations are performed by taking into consideration only the force constants up to a few nearest neighbors.

Application of fcc symmetry conditions to first neighbor force constants is discussed in the following section. (Reduction of the number of independent force constants out to eight neighbors is completed in Appendix A.) A discussion of constraints imposed by two types of central force models concludes Chapter I.

Symmetry Considerations

The number of independent force constants in a given problem may be reduced by crystal symmetry (29). However, for any system a preliminary reduction may be obtained from permutation symmetry. Assuming that Φ is a well-behaved function, the order of differentiation in Equation (1.6) is unimportant. Therefore, in general,

$$\varphi_{\alpha\beta} = \varphi_{\beta\alpha} \quad . \tag{1.33}$$

All symmetry operations which leave a lattice invariant may be represented by

$$\mathcal{S}_m = \{\underline{\underline{S}}|\vec{X}(m) + \vec{V}(S)\} \quad . \tag{1.34}$$

$\underline{\underline{S}}$ is a matrix representing a proper or improper rotation.[1] $\vec{X}(m)$ is a lattice translation and $\vec{V}(S)$ is a translation by some fraction of the

---

[1] An improper rotation is a pure rotation followed by a reflection or inversion.

lattice parameter. All operations which bring the lattice into coincidence with itself can be obtained from a combination of these three basic operations. If $\vec{R}(\ell, k)$ locates an atom in the undistorted crystal, the effect of $\mathfrak{S}_m$ on the crystal is defined by

$$\mathfrak{S}_m \vec{R}(\ell, k) = \overrightarrow{SR}(\ell, k) + \vec{X}(m) + \vec{V}(S) = R(L, K) \quad . \tag{1.35}$$

Here $\overrightarrow{SR}(\ell, k)$ is a vector resulting from the application of the rotation matrix $\underline{\underline{S}}$ to $\vec{R}(\ell, k)$. The components of $\overrightarrow{SR}(\ell, k)$ are obtained from the matrix product,

$$\begin{pmatrix} S_{xx} & S_{xy} & S_{xz} \\ S_{yx} & S_{yy} & S_{yz} \\ S_{zx} & S_{zy} & S_{zz} \end{pmatrix} \begin{pmatrix} R_x(\ell, k) \\ R_y(\ell, k) \\ R_z(\ell, k) \end{pmatrix} \quad .$$

Symmetry operations may also be applied to a distorted crystal with atomic positions given by

$$\vec{r}(\ell, k) = \vec{R}(\ell, k) + \vec{U}(\ell, k) \quad . \tag{1.36}$$

Then the application of $\mathfrak{S}_m$ to $\vec{r}(\ell, k)$ is given by

$$\mathfrak{S}_m \vec{r}(\ell, k) = \overrightarrow{SR}(\ell, k) + \overrightarrow{SU}(\ell, k) + \vec{V}(S) + \vec{X}(m) \quad . \tag{1.37}$$

Substituting from Equation (1.35) we have

$$\mathfrak{S}_m \vec{r}(\ell, k) = \mathfrak{S}_m \vec{R}(\ell, k) + \overrightarrow{SU}(\ell, k) \quad , \tag{1.38}$$

which may be written as

$$\mathfrak{S}_m \vec{r}(\ell, k) = \vec{R}(L, K) + \vec{U}'(L, K) \quad . \tag{1.39}$$

Therefore, when $\mathfrak{g}_m$ is applied to a distorted crystal it carries the displacement $\vec{U}(\ell, k)$ to the equivalent position (L, K). The displacement $\vec{U}'(L, K)$ at (L, K) is given by $S\vec{U}(\ell, k)$. Similarly if $\vec{U}(\ell', k')$ is carried by $\mathfrak{g}_m$ to (L', K'), then

$$\vec{U}(\ell', k') \xrightarrow{\mathfrak{g}_m} \vec{U}'(L', K') = S\vec{U}(\ell', k') \quad . \tag{1.40}$$

The potential energy of the pair (ℓk, $\ell' k'$) must be equal to the potential energy of the equivalent pair (LK, L'K'). Therefore, from Equation (1.8),

$$\sum_{\alpha\beta} U_\beta(\ell', k')\varphi_{\alpha\beta}(\ell k, \ell' k')U_\alpha(\ell, k) = \sum_{\mu\nu} U'_\nu(L', K')\varphi_{\mu\nu}(LK, L'K')U'_\mu(L, K) \quad . \tag{1.41}$$

Recall that according to a matrix product,

$$U'_\nu(L', K') = \sum_\beta S_{\nu\beta}U_\beta(\ell', k') \tag{1.42a}$$

and

$$U'_\mu(L, K) = \sum_\alpha S_{\mu\alpha}U_\alpha(\ell, k) \quad . \tag{1.42b}$$

Substituting into Equation (1.41) one obtains

$$\varphi_{\alpha\beta}(\ell k, \ell' k') = \sum_{\mu\nu} S_{\nu\beta}\varphi_{\mu\nu}(LK, L'K')S_{\mu\alpha} \quad . \tag{1.43}$$

In matrix notation this may be represented as

$$\underline{\underline{\varphi}}(\ell k, \ell' k') = \underline{\underline{S}}\underline{\underline{\varphi}}(LK, L'K')\tilde{\underline{\underline{S}}} \tag{1.44}$$

where $\tilde{\underline{\underline{S}}}$ is the transpose of the rotation matrix $\underline{\underline{S}}$.

If a symmetry operation leaves a given pair of sites unchanged, Equation (1.44) becomes

$$\Phi(\ell k, \ell' k') = \underline{\underline{S}}\Phi(\ell k, \ell' k')\tilde{\underline{\underline{S}}} \quad . \tag{1.45}$$

Therefore, by applying the symmetry operations which do not change a given pair of atoms, or which leave their positions reversed, one can compare the original and transformed matrices to obtain the independent force constants.

Before applying fcc symmetry operations to a first neighbor pair, it is useful to examine a relation which provides the number of independent force constants to be expected for a given pair of atoms. The equation is derived from group theory (30) and only the result is presented here.

$$N = \frac{1}{g}\{\Sigma[\chi(S)]^2 + \Sigma\,\chi(S'^2)\} \quad . \tag{1.46}$$

Here g is the total number of symmetry operations which leave the bond between an atom pair invariant or reversed.[1] $\Sigma[\chi(S)]^2$ is the sum of the squares of the characters of the "invariant" operations. $\Sigma\,\chi(S'^2)$ is the sum of the characters of the squares of the "reversal" operations. In other words, the "reversal" operations are applied twice and the characters of the resultant total operations are summed.

Characters of a symmetry operation may be obtained from tables in standard group theory books. The character is equal to the trace of a

---

[1] While it may be inappropriate to refer to a directional "bond" between atoms in a metal crystal, the term will be used to designate the line joining the atom pair for lack of a better word.

three dimensional matrix representation of an operation. Therefore, characters may also be obtained by writing the matrix for a given operation explicitly and finding the trace.

To reduce independent force constants by crystal symmetry one first finds all the symmetry operations which leave the bond between a given pair of atoms invariant or reversed. The number of independent force constants can then be calculated according to Equation (1.46). Next one applies the symmetry operations according to Equation (1.45) until the number of independent force constants is reduced to the predetermined number.

For example, the number of independent first neighbor force constants for a monatomic fcc lattice may be determined as follows. Consider the fcc structure shown in Figure 1.1. Let ℓ be length measured along the cubic cell edge. Take the origin at ℓ = (0, 0, 0) and the first neighbor of interest at ℓ' = $(\frac{1}{2}, \frac{1}{2}, 0)$.

Operations which leave that bond invariant are (1) reflection in the $(1\bar{1}0)$ plane; (2) reflection on the (001) plane; (3) a two-fold rotation about the bond axis (the [110] direction); (4) the identity. Operations which reverse the bond are (1) a two-fold rotation about the z axis ([001] direction); (2) a two-fold rotation about an axis perpendicular to both the z axis and the bond axis ($[\bar{1}10]$ direction); (3) reflection in the (110) plane; (4) inversion of coordinates. Using the appropriate characters, Equation (1.46) becomes,

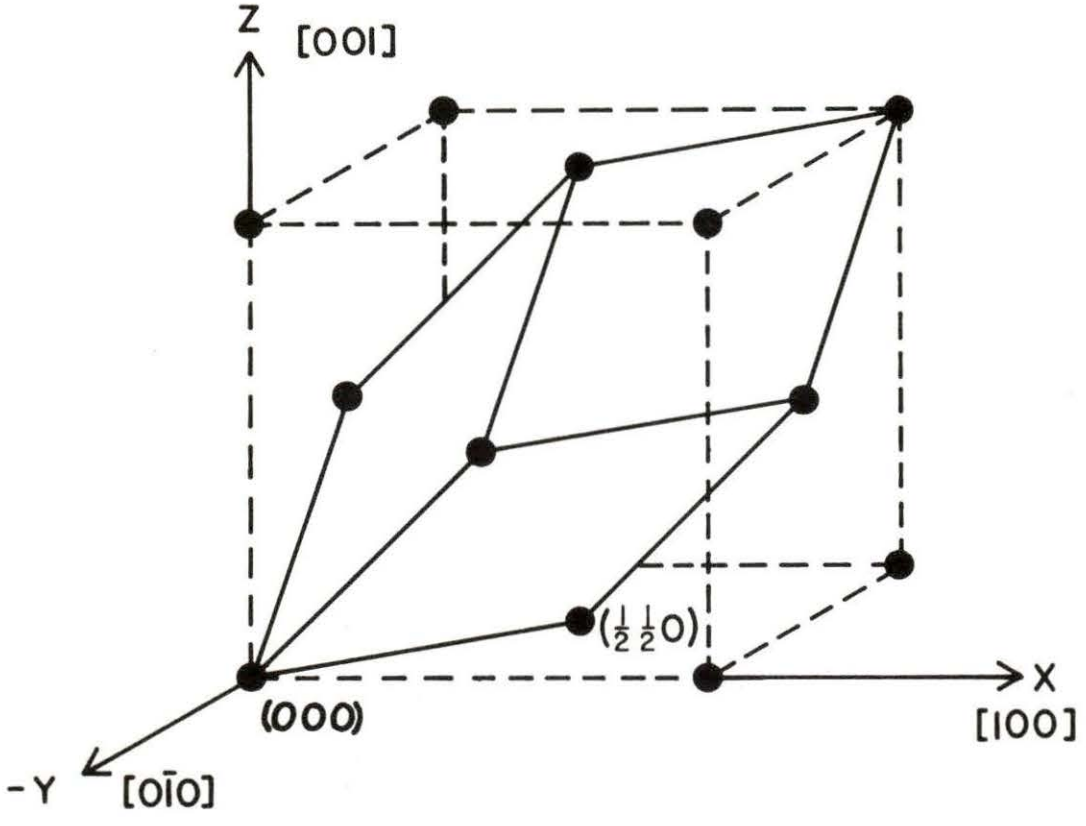

Figure 1.1. Cubic and primitive unit cells of a monatomic fcc lattice. Coordinates of the designated first neighbors are given in terms of the cubic cell length

$$N = \frac{1}{8}\{[(1)^2 + (-1)^2 + (1)^2 + (3)^2] + [(3) + (3) + (3) + (3)]\} \qquad (1.47)$$

$N = 3$.

Therefore, there are three independent first neighbor force constants.

Recalling permutation symmetry the initial force constant matrix may be written

$$\varphi(000, \tfrac{1}{2}\tfrac{1}{2}0) = \begin{pmatrix} xx & xy & xz \\ xy & yy & yz \\ xz & yz & zz \end{pmatrix} \quad . \qquad (1.48)$$

Permutation symmetry alone gives six independent force constants. Let a mirror reflection in the $(1\bar{1}0)$ plane be applied first.

$$\underline{\underline{S}}(1\bar{1}0) = \begin{pmatrix} 0 & 1 & 0 \\ 1 & 0 & 0 \\ 0 & 0 & 1 \end{pmatrix} \quad . \qquad (1.49)$$

Therefore,

$$\varphi(000, \tfrac{1}{2}\tfrac{1}{2}0) = \begin{pmatrix} 0 & 1 & 0 \\ 1 & 0 & 0 \\ 0 & 0 & 1 \end{pmatrix} \begin{pmatrix} xx & xy & xz \\ xy & yy & yz \\ xz & yz & zz \end{pmatrix} \begin{pmatrix} 0 & 1 & 0 \\ 1 & 0 & 0 \\ 0 & 0 & 1 \end{pmatrix} \qquad (1.50)$$

$$= \begin{pmatrix} 0 & 1 & 0 \\ 1 & 0 & 0 \\ 0 & 0 & 1 \end{pmatrix} \begin{pmatrix} xy & xx & xz \\ yy & xy & yz \\ yz & xz & zz \end{pmatrix}$$

$$\varphi(000, \tfrac{1}{2}\tfrac{1}{2}0) = \begin{pmatrix} yy & xy & yz \\ xy & xx & xz \\ yz & xz & zz \end{pmatrix} \quad . \qquad (1.51)$$

Comparing Equations (1.48) and (1.51) we see that $xx = yy$; $xz = yz$. The force constant matrix now contains five independent force constants,

$$\varphi(000, \tfrac{1}{2}\tfrac{1}{2}0) = \begin{pmatrix} xx & xy & xz \\ xy & xx & xz \\ xz & xz & zz \end{pmatrix} \quad . \qquad (1.52)$$

Applying a reflection in the (001) plane,

$$\varphi(000, \tfrac{1}{2}\tfrac{1}{2}0) = \begin{pmatrix} 1 & 0 & 0 \\ 0 & 1 & 0 \\ 0 & 0 & -1 \end{pmatrix} \begin{pmatrix} xx & xy & xz \\ xy & xx & xz \\ xz & xz & zz \end{pmatrix} \begin{pmatrix} 1 & 0 & 0 \\ 0 & 1 & 0 \\ 0 & 0 & -1 \end{pmatrix} \tag{1.53}$$

$$\varphi(000, \tfrac{1}{2}\tfrac{1}{2}0) = \begin{pmatrix} xx & xy & -xz \\ xy & xx & -xz \\ -xz & -xz & zz \end{pmatrix} \quad . \tag{1.54}$$

Comparing Equations (1.52) and (1.54) gives the final constraint,

$$xz = -xz = 0 \quad .$$

Thus the force constant matrix reduces to the following simple form involving only three independent force constants.

$$\varphi(000, \tfrac{1}{2}\tfrac{1}{2}0) = \begin{pmatrix} xx & xy & 0 \\ xy & xx & 0 \\ 0 & 0 & zz \end{pmatrix} \tag{1.55}$$

One can calculate independent force constants for the n-th neighbor in the same way. The independent force constants of an fcc lattice out to eight neighbors are determined in Appendix A.

Additional constraints can be imposed on the force constants by invoking a specific type of interaction. Two types of central force models are described below.

Central Force Models

If the potential energy between a pair of atoms is a function only of their separation, R, the interatomic force between the pair is a central force. Two types of central force models are commonly used. In the axially symmetric model, the forces between each given atom pair are central, but not necessarily derived from the same potential. The

potential energy function between first neighbors need not be the same as the potential energy function between third neighbors, although both are functions of R. Therefore, the axially symmetric model imposes constraints on each set of n-th neighbor force constants. On the other hand, if the central potential is the same for every n-th neighbor pair, an additional constraint can be derived from the equilibrium condition which involves all the force constants. This second type of model is often called simply the "central force" model which can be somewhat confusing. In both the axially symmetric model and the "central force" model the potential energy is a function only of R. Both involve central forces and differ only in the details of the model as described above (31). The axially symmetric model will be discussed first.

$$\text{For } R = \left|\vec{R}(\ell, k) - \vec{R}(\ell', k')\right| \tag{1.56}$$

Equation (1.6) may be rewritten

$$\varphi_{\alpha\beta}(\ell k, \ell' k') = \left(\frac{\partial^2 \Phi(R)}{\partial U_\alpha(\ell, k)\, \partial U_\beta(\ell', k')} \right)\Bigg|_0 \tag{1.57}$$

$$= \left[\frac{\partial}{\partial U_\alpha(\ell, k)} \left(\frac{\partial \Phi(R)}{\partial R} \; \frac{\partial R}{\partial U_\beta(\ell', k')} \right) \right]_{R=R_0} .$$

Let

$$\varphi_{\alpha\beta}(\ell k, \ell' k') = \left[\frac{\partial}{\partial U_\alpha(\ell, k)} \left(\frac{\partial \Phi(R)}{\partial R} \; \frac{X_\beta}{R} \right) \right]_{R=R_0} , \tag{1.58}$$

where

$$X_\beta = R \, \frac{\partial R}{\partial U_\beta(\ell', k')} = \text{the } \beta \text{ component of } R.$$

Let $U_\alpha(\ell, k) \to U_\alpha$; then Equation (1.58) becomes

$$\varphi_{\alpha\beta}(\ell k, \ell' k') = \left[\frac{\partial^2 \Phi(R)}{\partial R^2} \frac{X_\beta}{R} \frac{\partial R}{\partial U_\alpha} + \frac{\partial \Phi(R)}{\partial R} X_\beta \frac{\partial}{\partial U_\alpha} \left(\frac{1}{R} \right) + \frac{\partial \Phi(R)}{\partial R} \frac{1}{R} \frac{\partial X_\beta}{\partial U_\alpha} \right]_{R=R_0} . \tag{1.59}$$

Carrying out the derivatives and evaluating at R_0, one obtains

$$\varphi_{\alpha\beta}(\ell k, \ell' k') = \left. \frac{\partial^2 \Phi(R)}{\partial R^2} \right|_{R=R_0} \frac{X_\beta X_\alpha}{(R_0)^2} + \left. \frac{\partial \Phi(R)}{\partial R} \right|_{R=R_0} X_\beta \left(\frac{-X_\alpha}{(R_0)^3} \right) + \left. \frac{\partial \Phi(R)}{\partial R} \right|_{R=R_0} \frac{1}{R} \delta_{\alpha\beta} . \tag{1.60}$$

This can be expressed as

$$\varphi_{\alpha\beta}(\ell k, \ell' k') = \varphi_t(\ell k, \ell' k') \left(\delta_{\alpha\beta} - \frac{X_\alpha X_\beta}{(R_0)^2} \right) + \varphi_r(\ell k, \ell' k') \frac{X_\alpha X_\beta}{(R_0)^2} \tag{1.61}$$

where φ_r, the radial force constant, is given by

$$\varphi_r(\ell k, \ell' k') = \left. \frac{\partial^2 \Phi(R)}{\partial R^2} \right|_{R=R_0} \tag{1.62}$$

and φ_t, the tangential force constant, is defined by

$$\varphi_t(\ell k, \ell' k') = \frac{1}{R_0} \left. \frac{\partial \Phi(R)}{\partial R} \right|_{R=R_0} . \tag{1.63}$$

Thus for axially symmetric forces only two independent force constants exist for each type of neighbor.

Consider the first neighbor force constants of an fcc crystal. Recall from Equation (1.55) there are only three independent force constants for first neighbors. These are designated as 1XX, 1XY and 1ZZ. The first neighbor is located at $R = \frac{a}{2}(1, 1, 0)$. Substituting into Equation (1.61) one obtains

$$1XX = \frac{1}{a\sqrt{2}} \left(\frac{\partial \Phi(R)}{\partial R} \right) \Bigg|_{R_0} + \frac{1}{2} \frac{\partial^2 \Phi(R)}{\partial R^2} \Bigg|_{R_0} \tag{1.64}$$

$$1XY = -\frac{1}{a\sqrt{2}} \left(\frac{\partial \Phi(R)}{\partial R} \right) \Bigg|_{R_0} + \frac{1}{2} \left(\frac{\partial^2 \Phi(R)}{\partial r^2} \right) \Bigg|_{R_0} \tag{1.65}$$

$$1ZZ = \frac{\sqrt{2}}{a} \left(\frac{\partial \Phi(R)}{\partial R} \right) \Bigg|_{R_0} . \tag{1.66}$$

Eliminating the derivatives among the equations yields the constraint imposed on first neighbors by an axially symmetric potential.

$$1XX - 1ZZ = 1XY \tag{1.67}$$

The axially symmetric constraints for an fcc crystal out to eighth neighbor interactions are listed in Table 1.2.

If the potential energy is constrained to be an identical function of R for all n-th neighbor pairs an additional constraint may be derived. This "central force" constraint arises from considerations of crystal equilibrium. For a monatomic cubic crystal in equilibrium the

Table 1.2. Axially symmetric constraints to eight neighbors for fcc crystals

Neighbor	Constraints
1	$(1XX) - (1ZZ) - (1XY) = 0$
2	none
3	$(3XX) - (3YY) - 3(3YZ) = 0$
	$2(3XX) - 2(3YY) - 3(3XZ) = 0$
4	$(4XX) - (4ZZ) - (4XY) = 0$
5	$3(5XX) - 3(5YY) - 8(5XY) = 0$
	$(5XX) - 9(5YY) + 8(5ZZ) = 0$
6	none
7	$3(7XX) - 3(7ZZ) - 4(7XY) = 0$
	$2(7YY) - 2(7ZZ) - (7XY) = 0$
	$3(7YZ) - (7XY) = 0$
	$2(7XZ) - (7XY) = 0$
8	none

value of the lattice constant must minimize the total potential energy. Therefore,

$$\left(\frac{d}{dp} \left[\sum_n Z_n \Phi(R_n) \right] \right) \Bigg|_{p=a} = 0 \quad , \tag{1.68}$$

where p is the general separation along a cube edge (non-equilibrium lattice constant), R_n is the non-equilibrium interatomic separation of a given set (n) of neighbors, and Z_n is the number of equivalent neighbors in the set.

For fcc crystals,

$$Z_1, Z_2, Z_3, \ldots = 12, 6, 24, \ldots \tag{1.69}$$

$$R_1, R_2, R_3, \ldots = P/\sqrt{2}, P, \sqrt{6}\, P/2, \ldots \tag{1.70}$$

$$(R_0)_1, (R_0)_2, (R_0)_3, \ldots = a/\sqrt{2}, a, \sqrt{6}\, a/2, \ldots \tag{1.71}$$

The equilibrium condition given by Equation (1.68) becomes

$$0 = 6\sqrt{2}\left(\frac{\partial \Phi(R)}{\partial R} \right) \Bigg|_{(R_0)_1} + 6\left(\frac{\partial \Phi(R)}{\partial R} \right) \Bigg|_{(R_0)_2} + 12\sqrt{6}\left(\frac{\partial \Phi(R)}{\partial R} \right) \Bigg|_{(R_0)_3} + \ldots \tag{1.72}$$

Recall from Equation (1.66) that

$$\left(\frac{\partial \Phi(R)}{\partial R} \right) \Bigg|_{(R_0)_1} = (1ZZ) \frac{a}{\sqrt{2}} \quad .$$

Similarly the derivatives in each term of Equation (1.72) can be evaluated by applying the axially symmetric condition [Equation (1.60)] to each set of neighbors. These values are tabulated in Table 1.3.

Table 1.3. Derivatives of $\Phi(R)$ in central force models evaluated for n-th neighbor atoms for fcc crystals

n	$(R_o)_n$	$\left(\frac{\partial\Phi(R)}{\partial r}\right)_{(R_o)_n}$	$\left(\frac{\partial^2\Phi(R)}{\partial r}\right)_{(R_o)_n}$
1	$a/\sqrt{2}$	$(1ZZ)a/\sqrt{2}$	$2(1XX) - (1ZZ)$
2	a	$(2YY)a$	$(2XX)$
3	$\sqrt{6}\,a/2$	$[4(3YY) - (3XX)]a/\sqrt{6}$	$[5(3XX) - 2(3YY)]/3$
4	$\sqrt{2}\,a$	$(4ZZ)\sqrt{2}\,a$	$2(4XX) - (4ZZ)$
5	$\sqrt{10}\,a/2$	$(5ZZ)\sqrt{10}\,a/2$	$[9(5XX) - (5YY)]/8$
6	$\sqrt{3}\,a$	$[(6XX) - (6YZ)]\sqrt{3}\,a$	$(6XX) + 2(6YZ)$
7	$\sqrt{14}\,a/2$	$[2(7ZZ) - (7YZ)]\sqrt{14}\,a/4$	$2(7XX) - (7YY)$
8	$2a$	$2(8YY)a$	$2(8XX)$

For an fcc crystal, taking interactions to eight neighbors, the "central force" constraint is given by

$$(1ZZ) + (2YY) - 2(3XX) + 8(3YY) + 4(4ZZ) + 10(5ZZ) + 4(6XX) - 4(6YZ) + 28(7ZZ) - 14(7YZ) + 4(8YY) = 0 \quad . \tag{1.73}$$

The axially symmetric model will be discussed further with respect to the present study in Chapter III. First, however, inelastic neutron scattering basics and experimental details are presented in Chapter II.

CHAPTER II. THE NEUTRON SCATTERING EXPERIMENT

Inelastic Nuclear Scattering

Before proceeding to the experimental methods and details of the present study, it is useful to examine the basic principles of inelastic nuclear neutron scattering. As mentioned in Chapter I, the nuclear scattering of thermal neutrons from a crystal may be elastic or inelastic depending on whether or not the neutron exchanges any energy with the lattice. Elastic scattering is used for structure analysis and crystal alignment. Inelastic scattering provides the phonon spectrum for lattice dynamical studies.

Each of these kinds of scattering contains coherent and incoherent contributions. Coherent scattering arises from identical scattering conditions (i.e., identical nuclei) occurring throughout the lattice. If more than one isotope is present in the sample an incoherent contribution to the total scattering will also be present due to the difference in scattering amplitudes of nuclei of different isotopes. Nuclei possessing non-zero spin give rise to another incoherent contribution due to the interaction of the spin of the neutron with the spin of the nucleus. All of the stable isotopes of cerium have a nuclear spin of zero; therefore, incoherence in cerium is due only to isotope content. The incoherent scattering cross section that arises from the isotope content of natural cerium is very small (see Table I.1).

For phonon measurement all scattering contributions except inelastic coherent scattering are considered as background. The background

also includes scattering due to multi-phonon processes. Therefore, only the one-phonon inelastic coherent neutron scattering cross section is described below. Since scattering theory is discussed thoroughly by numerous authors (32), only the results are presented here. The differential cross section is given by

$$\frac{d^2\sigma_{coh}}{d\Omega d\nu} = \frac{2\pi}{V} \sum_{\vec{q},j,\vec{\tau}} \frac{K'}{K_0} \frac{h^2(n + \frac{1}{2} \pm \frac{1}{2})}{2\nu} |F_j(\vec{Q})|^2$$

$$\times \delta[h\nu \mp h\nu_j(\vec{q})]\delta[\vec{Q} - (\vec{q} + \vec{\tau})] \quad . \qquad (2.1)$$

The terms of Equation (2.1) are defined below. Following these brief definitions the dependence of the cross section on several of the terms is discussed in more detail.

Ω = solid angle

V = primitive unit cell volume

$\vec{q}$ = phonon wave vector

j = identifier for mode of vibration

$\vec{\tau}$ = reciprocal lattice vector (this definition includes the factor of 2π)

$\vec{K}'$ = scattered neutron wave vector

$\vec{K}_0$ = incident neutron wave vector

$h\nu = \frac{\hbar^2(K'^2 - K_0^2)}{2m_n}$ = energy change of the neutron when scattered - m_n is the neutron mass

$h\nu_j(\vec{q})$ = energy of the created or annihilated phonon

$\vec{Q} = \vec{K}_0 - \vec{K}'$ = momentum transfer, i.e., scattering vector

$$n = \frac{1}{(e^{h\nu/kT} - 1)} = \text{average phonon occupation number}$$

$$F_j(Q) = \sum_k \frac{\bar{b}_k}{M_k^{\frac{1}{2}}} \vec{Q} \cdot \vec{U}(k, \vec{q}, j) e^{i\vec{\tau}\cdot\vec{R}(k)} e^{-W_k}$$

= inelastic coherent neutron structure factor

M_k = mass of atom k

$\bar{b}_k$ = coherent nuclear scattering amplitude for atom k

$\vec{R}(k)$ = position vector for atom k with respect to the primitive cell origin

$\vec{U}(k, \vec{q}, j)$ = displacement vector for atom k

$W_k = \frac{1}{2} \langle [\vec{Q} \cdot \vec{U}(k, \vec{q}, j)]^2 \rangle$ = the Debye-Waller factor

The upper and lower signs in Equation (2.1) correspond to phonon creation and annihilation respectively. The two delta functions impose two conditions necessary for a non-zero scattering cross section. The first delta function requires energy conservation.

$$h\nu = \frac{\hbar^2}{2m_n} (K'^2 - K_0^2) = \pm h\nu_j(\vec{q}) \tag{2.2}$$

The energy lost or gained by the neutron must correspond to the energy change of the lattice - the creation or annihilation of a phonon of the appropriate energy. The second delta function requires momentum conservation.

$$\vec{Q} = \vec{K}_0 - \vec{K}' = \vec{\tau} + \vec{q} \tag{2.3}$$

The momentum change of the neutron must correspond to the momentum change of the lattice.

According to the $\frac{K'}{K_0}$ factor in Equation (2.1) it would appear that a neutron energy gain process (phonon annihilation) would produce a larger scattering intensity than a neutron energy loss (phonon creation) process. However, the population factor, $(n + \frac{1}{2} \pm \frac{1}{2})$ must also be taken into account. At room temperature the population factor for an energy gain process is 5.5 for phonons having a frequency of 1.0 THz (1 THz = 10^{12} cps). However, this factor becomes less than 0.6 for phonons with frequencies above 6 THz. Furthermore, experimental resolution and methods of measurement affect the observed intensity. For example, resolution is higher for an energy loss process. Resolution effects and measurement methods are discussed more fully in a later section.

In addition to the frequency dependence which enters Equation (2.1) through the population factor the cross section is a function of the phonon frequency directly through the $1/\nu$ factor. Therefore, the intensity decreases as the phonon frequency increases.

The structure factor, $F_j(\vec{Q})$ contains several terms which produce important effects on the cross section. These terms exert a particularly strong influence since the cross section depends on $|F_j(\vec{Q})|^2$.

The coherent scattering length of the nuclei, $\bar{b}_k$, affects all phonon measurements independent of frequency or experimental parameters. The variation of $\bar{b}_k$ among most common isotopes is roughly an order of magnitude. The value for cerium (see Table 1.1) lies in the lower one-third of this range. The effect of cerium's low coherent scattering

length on the present experiment will be discussed in the section describing experimental details.

The form factor also contains the dot product, $\vec{Q} \cdot \vec{U}$, which requires the scattering intensity to go to zero for a mode with displacement $\vec{U}$ perpendicular to the scattering vector, $\vec{Q}$. According to Equation (1.20) this is equivalent to a mode with polarization vector, $\vec{e}(\vec{q})$, perpendicular to $\vec{Q}$. If an experiment is arranged so that $\vec{Q}$ always lies in a mirror plane of the crystal, no scattering will be observed for modes polarized perpendicular to that plane. The scattering will be strongest for those modes having $\vec{e}(\vec{q})$ nearly collinear with $\vec{Q}$. This feature of the form factor allows for the identification of observed modes.

According to the $\vec{Q} \cdot \vec{U}$ term, it appears that the largest scattering intensity will be obtained by using the largest possible $\vec{Q}$ values. However, the Debye-Waller factor, e^{-2W_k}, decreases the intensity for large $\vec{Q}$ due to the Q^2 factor appearing in the exponent. This effect is usually minor at room temperatures for experimental $\vec{Q}$ values commonly used. At very high temperatures, where $\langle \vec{U} \rangle$ becomes large, however, the Debye-Waller factor significantly reduces the intensity with increasing $\vec{Q}$.

Due to resolution effects, optimizing the cross section formula by judicious choices of K_0, K', and $\vec{Q}$ does not insure optimum experimental results. The description of the effect of resolution on the observed scattering is incorporated into the discussion of measurement techniques. First, however, basic principles of magnetic inelastic scattering are presented. A description of the triple axis instrument is

then given to facilitate understanding of the measurement techniques discussed thereafter.

Inelastic Magnetic Scattering

As mentioned in Chapter I, magnetic scattering of neutrons occurs because of the neutron's intrinsic magnetic moment. Only inelastic magnetic scattering is discussed here. The differential inelastic magnetic cross section is proportional to the quantities given in Equation (2.4) (33). Constant factors have been omitted for simplicity.

$$\frac{d^2\sigma}{d\Omega d\nu} \sim \frac{K'}{K_0} |f(\vec{Q})|^2 (n + 1) \mathrm{Im}[\chi(\vec{Q}, \nu)] e^{-2W} \qquad (2.4)$$

Here $f|\vec{Q}|$ is the magnetic form factor, n is the magnetic excitation occupation number, and $\chi(\vec{Q}, \nu)$ is the generalized susceptibility. The other symbols retain the definitions presented in connection with Equation (2.1).

The magnetic scattering intensity depends strongly on the magnetic form factor squared. $|f(\vec{Q})|^2$ drops off with increasing $\vec{Q}$ (see Figure 3.11), therefore, the inelastic magnetic scattering cross section also decreases with increasing $\vec{Q}$.

The Debye-Waller factor, K', K_0, and analogous population factors appear in both the magnetic and the phonon cross sections. The effect of these terms on the magnetic cross section follow the pattern previously discussed for phonon scattering.

The generalized susceptibility is a function of both $\vec{Q}$ and ν. For a given $\vec{Q}$ value, variation of the magnetic cross section is given by

$\frac{K'}{K_0}(n + 1)\chi(\vec{Q}, \nu)$. Since K', K_0, and ν are known experimental parameters, $\vec{\chi}(Q, \nu)$ can be extracted from the data.

The generalized susceptibility enters the cross section formula for magnetic scattering because of its intimate relation to the magnetic moment of the atoms in the crystal. (Recall $\chi(\vec{Q}, \nu)$ is a response function describing the response of a material to a magnetic field which varies both in space and time.) Since it is the interaction of the magnetic moment of the neutrons with the magnetic moment of the atoms which produces magnetic scattering, it is intuitively reasonable that $\chi(\vec{Q}, \nu)$ should appear in the cross section.

Magnetic inelastic scattering can produce well-defined, narrow peaks in the scattered neutron intensity or a single broad feature covering a wide energy range. To understand these two features of magnetic scattering consider the following example.

In the absence of magnetic and electric forces a rare-earth paramagnetic ion (well above the Curie temperature) has a ground state degeneracy of (2J + 1). Due to the presence of other ions in the crystal, however, the ion under consideration is subject to an electric field. This crystal field does not break down the L-S coupling of a rare-earth ion because the unfilled 4f shell is shielded by the 5d and 5p electrons. The crystal field produces sublevels in the J states, however, with an expected separation of 10^{-3} to 10^{-1} eV (34). Transitions between these states can be induced by an exchange of the appropriate amount of energy with a thermal neutron.

The two types of magnetic elastic scattering arise from the relative separation of these sublevels. If they are well-defined discrete states, the intensity of the scattered neutrons will contain narrow peaks corresponding to resonances in $\chi(\vec{Q}, \nu)$. On the other hand, if these levels are very closely spaced forming a quasi-continuum, $\chi(\vec{Q}, \nu)$ will exhibit only a single broad peak which can be extracted from the data. Detection of both kinds of magnetic inelastic scattering is discussed more fully in the section on measurement techniques.

First, however, the triple axis instrument which is used both in phonon and magnetic inelastic scattering is described.

The Triple Axis Spectrometer

A standard triple axis spectrometer is shown diagrammatically in Figure 2.1. An intense beam of neutrons from a nuclear reactor having a spectrum of thermal energies is incident on the monochromating crystal. They are Bragg diffracted at an energy E_0 which is dependent upon the angle $2\theta_m$. The monochromatic beam produced passes through a collimator made of parallel strips of cadmium. Since cadmium has a very high absorption cross section for neutrons, these Soller slits limit the horizontal divergence of the beam. The collimated beam strikes the sample set at angle ψ. Those neutrons scattered at angle Φ pass through another set of Soller slits to the analyzer. The analyzing crystal is set at an angle of $2\theta_A$ to Bragg diffract neutrons of a given final energy, E', into the detector.

The calculations of the angle variations, and the driving of motors to set those angles for a given scan are performed by an on-line

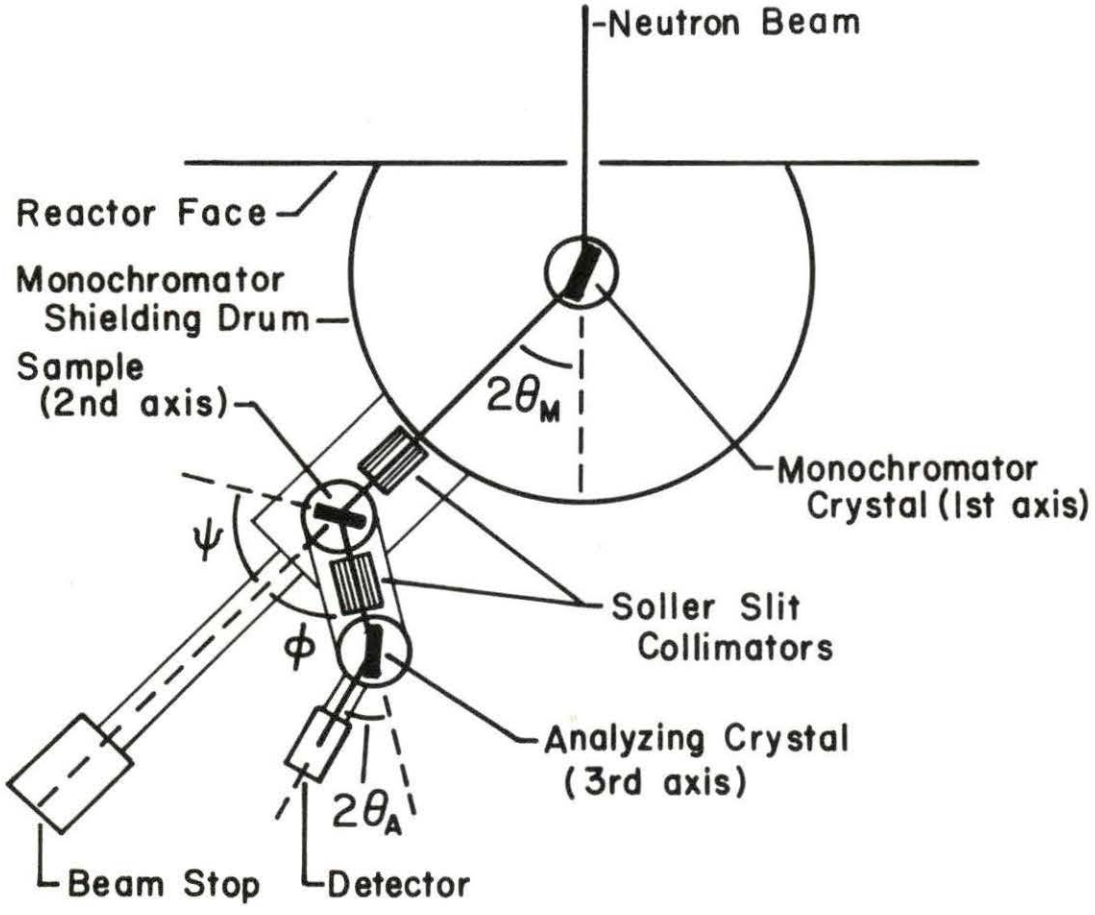

Figure 2.1. Schematic diagram of a typical triple axis spectrometer viewed from above

computer. Usually a monitor is located between the monochromator and the sample. The monitor is essentially a detector with a very low counting efficiency ($\sim$0.1%) so that it samples the beam without serious attenuation. Counting each point in a scan for a given monitor count instead of for a given time corrects for any variations in reactor power that occur during the measurements.

Specific features of the various triple axis instruments used for the present experiment are described in the section on experimental details. Basic techniques utilized in a standard inelastic neutron scattering experiment are discussed below.

Measurement Techniques

For most lattice dynamical studies, the triple axis instrument is used to measure phonons having $\vec{q}$ lying along directions of high symmetry. The first Brillioun zone of an fcc lattice is given in Figure 2.2. High symmetry lines and points are labeled with standard group theoretical notation. In most inelastic experiments performed on fcc crystals the phonons measured are those with wave vectors lying along the high symmetry directions shown: $\Delta[001]$, $\Sigma[110]$, and $\Lambda[111]$.

These directions are chosen because the phonons with $\vec{q}$ lying along these directions have polarizations which are purely longitudinal or transverse to the corresponding $\vec{q}$. For a monatomic lattice there will be one longitudinal mode and two transverse modes for each of the three directions.

For the designated high symmetry directions the dynamical matrix may be factored by a technique analogous to the symmetry reduction of

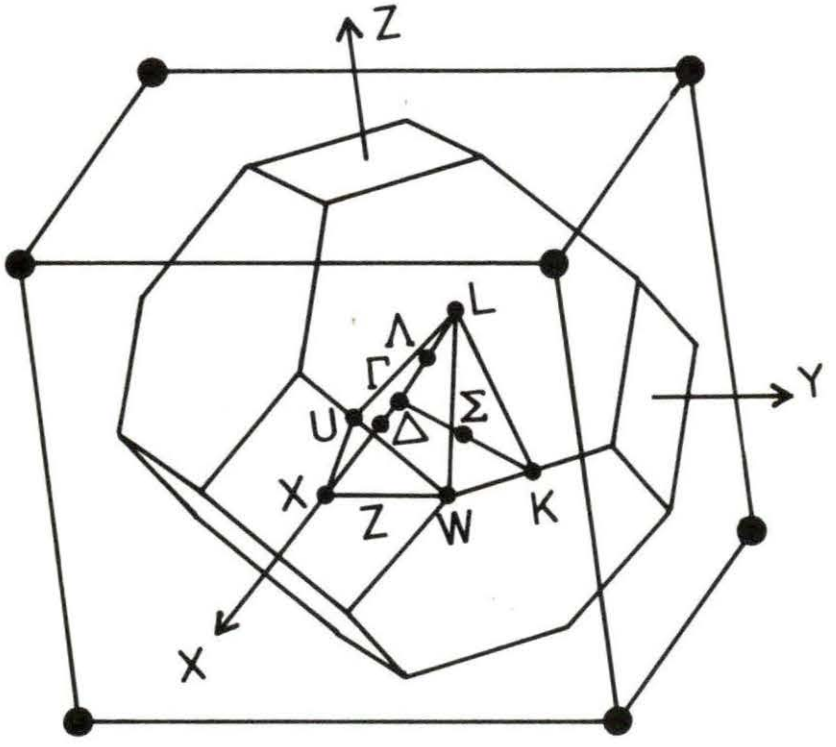

Figure 2.2. The first Brillioun zone of an fcc lattice. Symmetry lines and points are labeled with standard group theoretical notation

the force constant matrix. Solving Equation (1.24) using the factored dynamical matrix, one finds that the frequencies of the phonons in these directions are given by simple linear combinations of interatomic force constants. The resulting eigenvectors give the polarizations.

Due to the symmetry of an fcc crystal the frequencies of the two transverse modes in the [001] direction are the same. The [111] transverse modes are also degenerate. Therefore, only seven independent branches of the dispersion relation remain to be determined. These are L [001], T [001], L [110], T_1 [110], T_2 [110], L [111] and T [111]; where L denotes a longitudinal polarization, T_n a transverse polarization, and the phonon wave vector $\vec{q}$ lies along the designated direction. As mentioned in Chapter I, the phonon frequencies are periodic functions of $\vec{q}$. Therefore, only phonons with wave vectors lying within the first Brillioun zone need to be determined.

In an fcc crystal six of the seven phonon modes of interest lie in the $(1\bar{1}0)$ mirror plane. Only T_1 [110] is perpendicular to this plane. The T_1 [110] mode may be obtained from scattering in the (100) plane. Figure 2.3 represents the $(1\bar{1}0)$ plane of an fcc lattice in reciprocal space. The first Brillioun zone is outlined around each reciprocal lattice point. The $\vec{Q}$, $\vec{\tau}$, $\vec{q}$, and $\vec{e}$ vectors shown correspond to the scattering process used for the measurement of several different phonons. The polarization vector of a T_1 [110] phonon is perpendicular to this diagram. Figure 2.4 represents the (100) plane of an fcc crystal in reciprocal space. Vectors corresponding to scattering processes for some standard T_1 [110] measurements are included. Although they can be

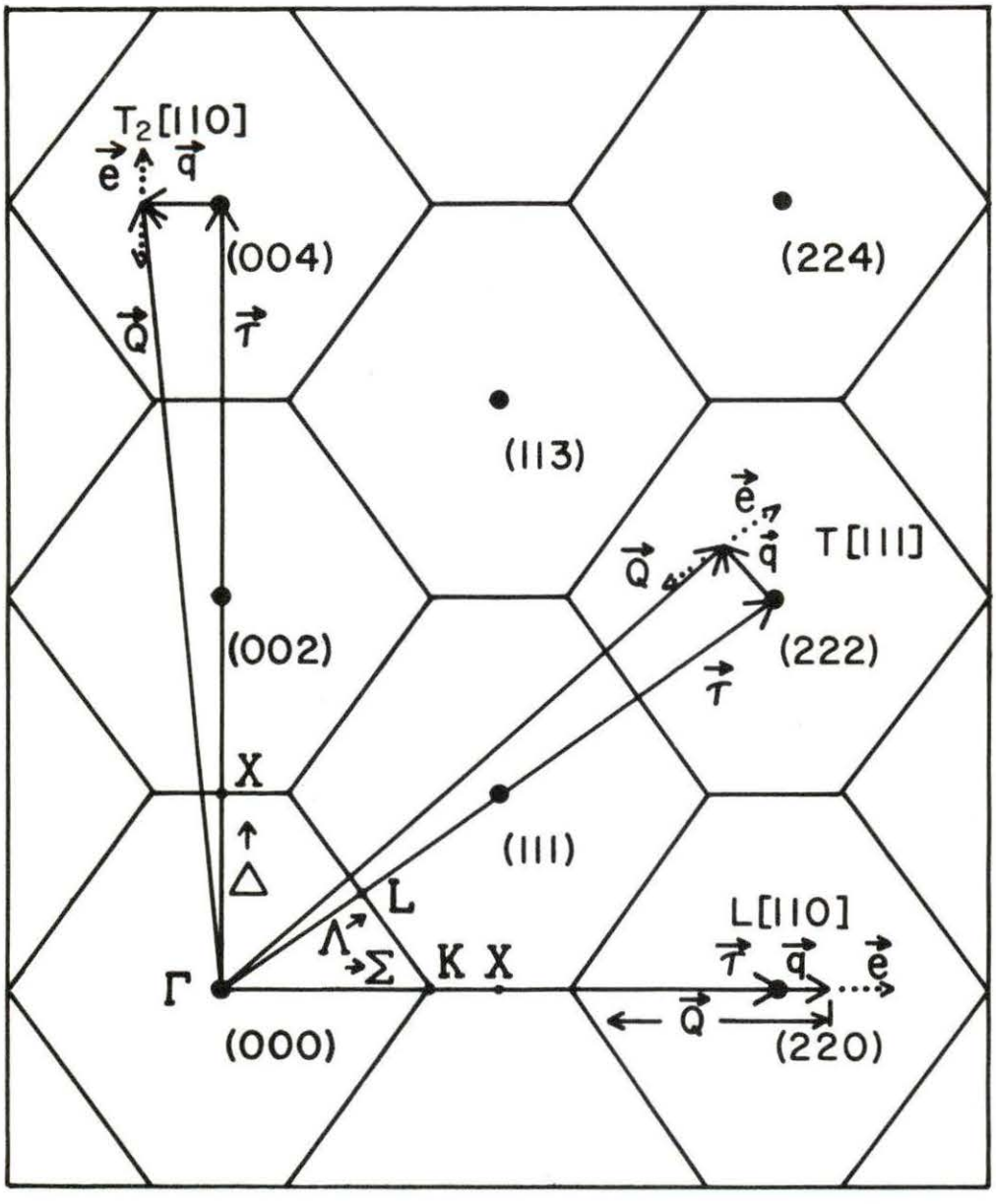

Figure 2.3. $(1\bar{1}0)$ plane of the reciprocal lattice of an fcc crystal. The momentum-space vectors associated with three phonons are also shown, with polarization vectors, $\vec{e}$, indicated by dotted lines, ←····→. The first Brillioun zone around the designated origin is labeled with standard group theoretical notation

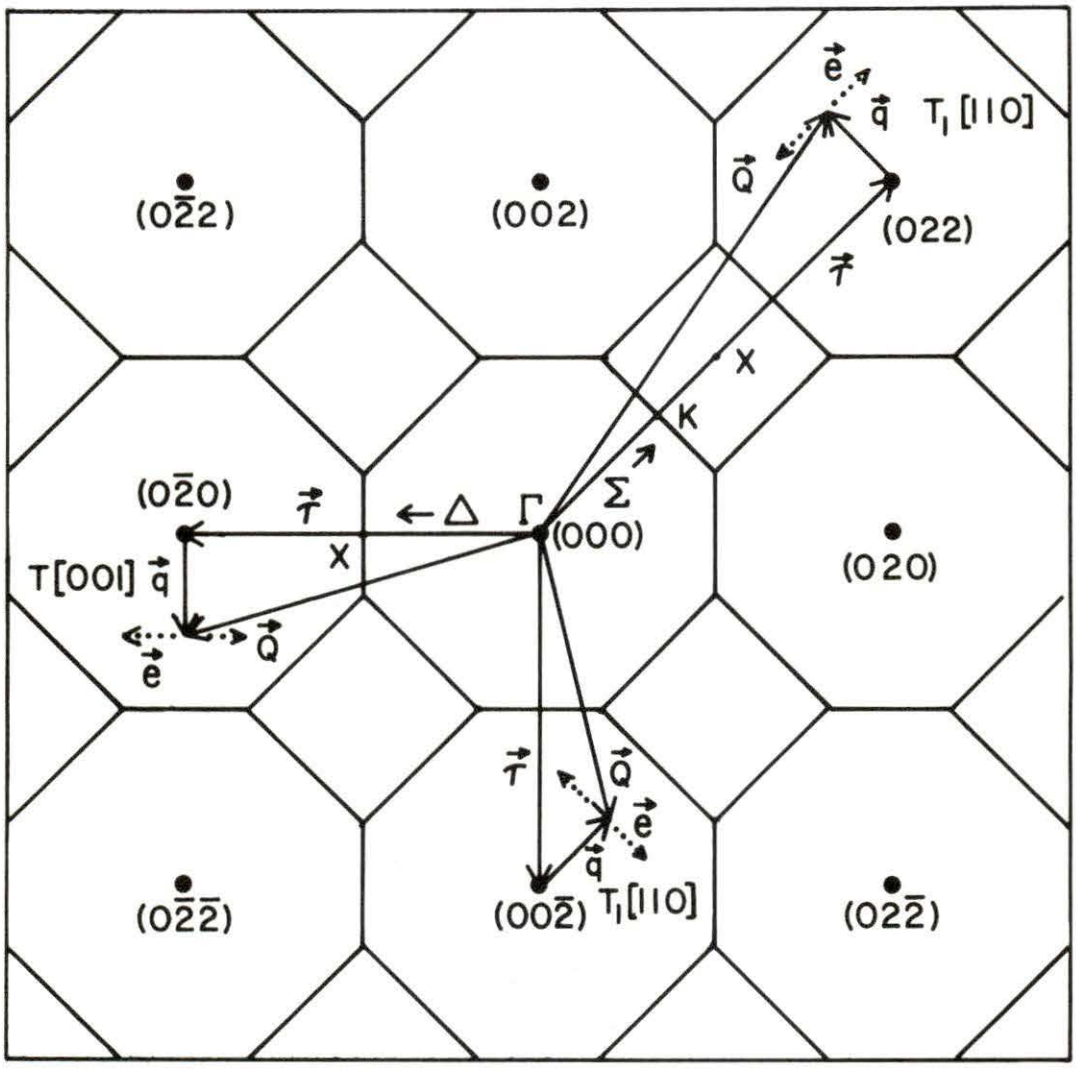

Figure 2.4. (100) plane of the reciprocal lattice for an fcc crystal with the momentum-space vectors of three phonons. Polarization vectors, $\vec{e}$, are shown with dotted lines, ←····→

measured in either plane, a T [001] phonon is included in Figure 2.4 since some of the T [001] data of the present work were measured in the (100) plane. (See Table 2.2).

A common experimental procedure used in obtaining the phonon branches is the "constant Q" method (25). This method was used in nearly all of the measurements of the present work and is the only method discussed.

In the "constant Q" method the scattering vector, $\vec{Q} = \vec{K}_0 - \vec{K}'$ is held constant while the energy transfer, $h\nu = \frac{\hbar^2}{2m_n}(K'^2 - K_0^2)$ is varied. The result is a vertical scan through the dispersion curve shown in Figure 2.5a. If the magnitude of $\vec{K}'$ is held fixed during a given scan, the vector $\vec{K}_0$ and the origin of $-\vec{K}'$ follow the dashed arc shown in Figure 2.5b. The majority of the measurements reported here were of this type.

The components of the $\vec{Q}$ vector are given by

$$Q_x = K_0 \cos\psi - K' \cos(\Phi + \psi) \tag{2.5}$$

$$Q_y = K_0 \sin\psi - K' \sin(\Phi + \psi) \quad . \tag{2.6}$$

For given values of Q_x, Q_y, and K', the variables K_0, Φ, and ψ can be calculated to perform the desired scan in energy.

For a constant Q scan with fixed final energy, the phonon cross section formula appears to be dependent on $\frac{1}{K_0}\frac{n}{\nu}$. However, the K_0 dependence can be removed if a uranium fission monitor is used in the experiment. The efficiency of such a monitor is proportional to 1/V, where V is the incident neutron velocity. Therefore, the K_0 dependence

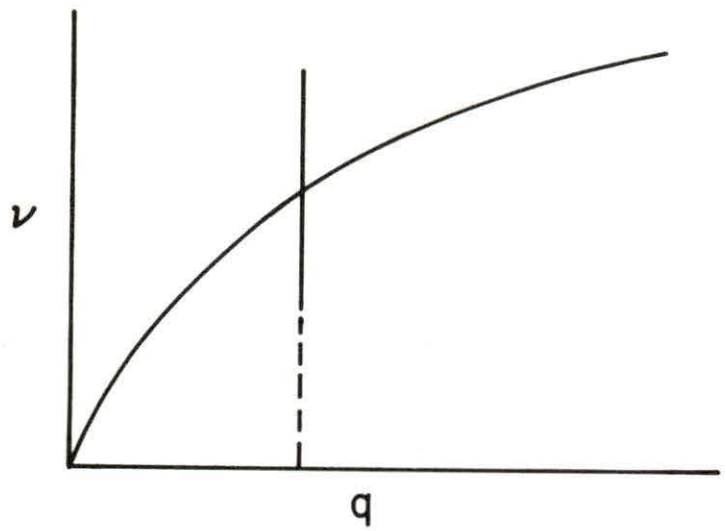

Figure 2.5a. A vertical scan through a dispersion curve as produced by the "constant-Q" method

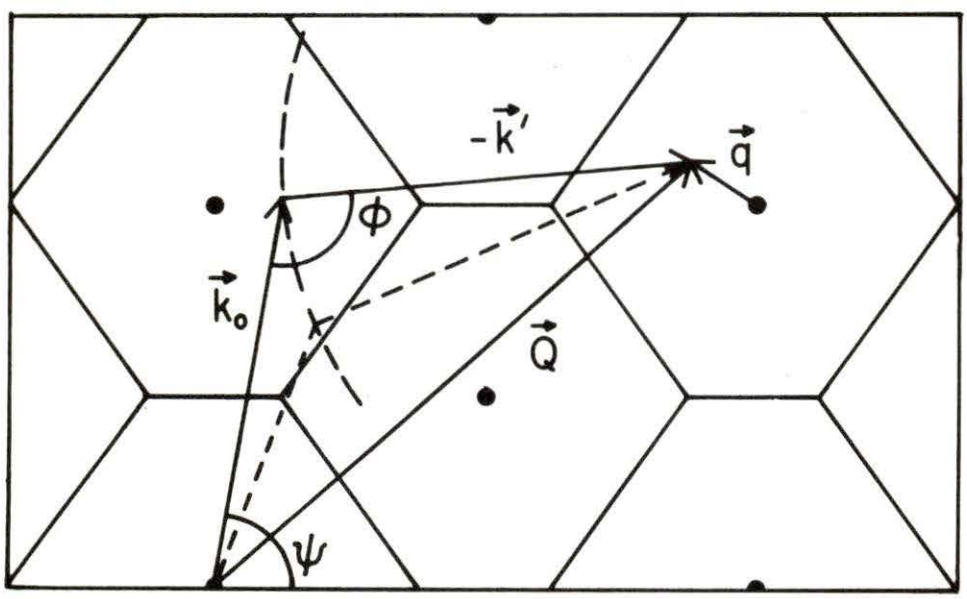

Figure 2.5b. The motion of momentum-space vectors in the reciprocal lattice for a constant Q scan using fixed final energy (i.e., fixed $|\vec{k}'|$)

in the cross section is effectively removed by the monitor. All of the present measurements were made using such a monitor.

The constant Q method may also be used to observe magnetic excitations. A constant Q scan avoids intensity variation due to the magnetic form factor in the cross section. It is important to avoid phonons when attempting to detect magnetic scattering. Due to the periodic nature of momentum space, every reciprocal lattice point is an equivalent Brillioun zone center (see Figure 2.3). For a monatomic lattice all the phonon branches go to zero at the Brillioun zone center. Therefore, by performing magnetic scattering measurements about reciprocal lattice points (i.e., with $\vec{Q} = \vec{\tau}$), one phonon scattering is avoided.

A magnetic excitation can be differentiated from a phonon peak by examination of the $\vec{Q}$ dependence of the scattered intensity. For an identical energy scan repeated at larger $\vec{Q}$, the intensity of a phonon peak will increase due to the $\vec{Q} \cdot \vec{U}$ term in the phonon cross section. On the other hand, the intensity of a magnetic excitation will decrease due to the magnetic form factor in the magnetic cross section.

If the magnetic scattering of the material does not exhibit well-defined excitations but follows a single broad structure in the generalized susceptibility, a constant Q scan over a very wide energy range is necessary to extract $\mathrm{Im}\,\chi(\vec{Q}, \nu)$. Performing a constant Q scan with fixed K' and using a monitor removes the K_0 factor from the magnetic cross section in the same way that K_0 is eliminated from the phonon cross section. Therefore, the observed scattering intensity depends only on $(n + 1)\,\mathrm{Im}\,\chi(\vec{Q}, \nu)$ for this type of measurement. The

generalized susceptibility can be determined by dividing out the frequency dependent population factor from the observed intensity at each point in the scan.

The magnetic form factor can also be examined using inelastic magnetic scattering. If a magnetic measurement is performed at constant energy transfer the scattered intensity will vary as a function of $|f(\vec{Q})|^2$. In this type of measurement one must be careful to avoid phonon energies in the range of $\vec{Q}$ that is scanned.

Both phonon and magnetic excitation measurements are subject to experimental resolution effects. The magnetic excitation linewidth is given by $\chi(\vec{Q},\nu)$ which is a characteristic of the material, hence it is different for each experiment. The theoretical linewidth of the phonons, however, (in the context of the harmonic approximation) is given explicitly in the cross section. Therefore, experimental resolution effects have been more thoroughly studied in connection with phonon measurements and are presented below in this context only.

The presence of the two delta functions in the phonon cross section formula implies infinitely sharp resolution in energy and momentum. However, finite experimental resolution allows the detection of neutrons corresponding to energies of $h(\nu + \Delta\nu)$ and momentum transfer, $(\vec{q} + \Delta q)$, when the instrument has been set to detect neutrons of energy $h\nu$ and momentum $\vec{q}$ only. Factors contributing to the broadening of the resolution are the horizontal divergence of the beam allowed in

each collimator, vertical divergence of the beam, and mosaic spread[1] in the monochromator, sample, and analyzer.

One resolution effect arises from the orientation of the instrument. To simplify the problem consider elastic scattering from two crystals only, the monochromator and sample in Figure 2.1. Notice that the sample is nearly parallel with the beam incident on the monochromator. If the sample was rotated by 90° it would still reflect the neutrons from the same set of crystal planes but the diffracted beam would be nearly antiparallel to the beam incident on the monochromator. A perfectly parallel arrangement produces neutron groups with widths governed by the mosaics of the sample and the monochromator. The "antiparallel" arrangement width is much greater, being roughly proportional to the sum of the mosaics and the angle of collimation (10). The observed resolution in inelastic scattering follows the same pattern. For best resolution the beam scattered from the sample should be roughly parallel to the beam incident on the monochromator, and the final scattered beam from the analyzer should be "parallel" to the beam incident on the sample. This results in the standard "W" configuration shown in Figure 2.1.

---

[1] Real crystals do not consist of a single perfect lattice, but are divided up by dislocations into small blocks. These separate blocks will display a spread of misorientations relative to one another known as mosaic spread. The crystal will then diffract neutrons of a given energy through a small range of angle settings instead of at just one precise angle.

For inelastic measurements the resolution may be improved over the above "instrument" resolution by the correct choice of the direction of $\vec{q}$. If one considers a group of neutrons with a small spread of $\vec{K}_0$ falling on the sample (instead of a single "ray") and traces the effect throughout the entire system the following results (35) are obtained: (1) For a "W" configuration the best resolution results when $\vec{q}$ is directed such that the resultant $\vec{Q}$ vector is counterclockwise from the reciprocal lattice vector, $\vec{\tau}$. (All $\vec{q}$ vectors in Figures 2.3 and 2.4 are of this type.) (2) The intensity and resolution of the scattered neutron group are dependent on the slope of the dispersion curve. Since the slope of a dispersion curve changes with $\vec{q}$, the resolution and intensity of the phonons are also $\vec{q}$ dependent. Most dispersion curves flatten out at large $\vec{q}$ values. This produces a broadening of the phonons as the zone boundary is approached.

Another experimentally observed "rule of thumb" for good resolution deals with matching the magnitudes of $\vec{K}_0$, $\vec{K}'$, and $\vec{q}$. If the magnitudes of these quantities are nearly the same, the resolution is usually better than if they differ by a significant amount. This point is explored further in the context of the present experiment in the discussion of experimental details.

Resolution effects arise from detection of neutrons with a small range of frequency and momentum instead of a single value. Another experimental problem is the accidental detection of neutrons scattered by other processes besides the phonon or magnetic scattering being studied. Such spurious processes can arise in one of several ways.

The most common problem is the unintentional detection of Bragg scattering in the sample. The settings of Φ and ψ for a given scan may accidentally coincide with angle settings appropriate for Bragg scattering in the sample. If the analyzer scattered only coherently the Bragg diffracted beam would not enter the detector. Due to elastic incoherent scattering in the analyzer, some of these neutrons do enter the detector. This may be designated as a B-B-Incoh process; a Bragg process in the monochromator and sample, and incoherent scattering in the analyzer. This process can be identified by placing a second monitor between the sample and the analyzer. The second monitor detects a strong peak due to the intense Bragg scattering in the sample. Measuring the phonon from a different lattice point, or changing $\vec{K}_0$ or $\vec{K}'$ will alleviate the problem.

Incoherent scattering in the sample and higher order Bragg diffraction in the analyzer may also give rise to spurious neutron groups. If the analyzer is set to diffract neutrons of final wavelength λ' (energy E'), higher order Bragg planes can scatter $\lambda'/2$ (4E'), $\lambda'/3$ (9E'), etc. into the detector. If neutrons incident on the sample have an energy $E_0 = 4E'$ and undergo elastic incoherent scattering a B-Incoh-B process can occur. This problem can be prevented by using an analyzer reflection with a zero structure factor for second order scattering. The final energy, E', can also be changed so that the new $E_0 = 4E'$ does not occur within the given scan range.

The third spurious process involves contamination in the beam incident on the sample. Incoherent and higher order scattering in the

monochromator may contribute undesired energies to the beam. Phonons from the monochromator may also scatter into the incident beam. If the sample is coincidentally set properly, it may scatter these "contaminating" neutrons in such a way that their final energy is E' and they are passed by the analyzer. Repeating the measurements under different conditions will remedy the situation.

Given the previous brief review of the relevant scattering cross sections and the experimental instrumentation and methods, the details of the γ-Ce experiment itself are presented below. Following a discussion of the measurements the data used for the analysis are tabulated. The analysis of the phonon and magnetic excitation data is presented in Chapter III.

Experimental Details and Results

The measurements reported in the present work were performed on a γ-Ce sample obtained from O. D. McMasters and K. A. Gschneidner, Jr. of Ames Laboratory. (Initially, a few measurements were begun on a small sample of γ-Ce, but when a larger crystal became available it was immediately put into use. Data from the first sample are included in Appendix B.) The second, larger crystal was an allotropically pure, cigar-shaped boule. The purity analysis of the cerium stock from which the boule was made is given in Table 2.1. No purity analysis of the sample itself was made.

Examination with a double axis diffractometer identified a polycrystalline section on one end of the sample, numerous small crystallites,

Table 2.1. Purity analysis of cerium stock #Ce-52374$

Spark Source Spectrometric Analysis (Atomic ppm)

LI	<.000	BE	<.003	B	<.01	NA	.04	MG	<.01	AL	.02	SI	.079	P	.02
S	<1	CL	.7	K	.03	CA	.2	TI	.21	V	.014	CR	3.4	MN	.75
FE	13	CO	.04	NI	3	CU	2	ZN	.08	GA	<.02	GE	<.1	AS	.02
SE	<.1	KR	<.5	RB	<.8	SR	<.4	ZR	<.2	NB	<20	MO	<.2	RU	<.09
RH	<.02	PD	<.05	AG	<.009	CD	<.02	IN	<.009	SN	<.03	SB	<.01	TE	<.02
I	<.01	CS	<.001	BA	<.3	HF	<.3	TA	6.0	W	<.4	RE	<.1	OS	<.2
IR	<.08	PT	4.0	AU	<.02	HG	<.02	TL	<.02	PB	<.05	BI	<.01	TH	<.2
														U	.30

Rare Earth Impurities

SC	.3	Y	10	LA	9	CE		PR	<1	ND	4	SM	<.4	EU	<.05
GD	6	TB	<1	DY	1	HO	<1	ER	5	TM	<.06	YB	<.3	LU	.90

Vacuum Fusion Results (Wt ppm)

O	44	N	10	H	2	C	4	F	26	FE	2.5

and two fairly large crystals in the specimen. After some initial confusion, these two large crystals were easily identifiable from the distinctive difference in their shapes revealed by Polaroid photographs of their (111) and (002) reflections. The difference in count rate between the two crystals on these reflections was roughly a factor of two. For obvious reasons the larger crystal of the two was used for the measurements. From the Polaroid photographs this crystal was estimated to have a volume of approximately 3 cm^3. No measurements of mosaic width were made for this crystal, however, the mosaic width was estimated to be in the range from 15-20 minutes of arc. During the orientation procedure an oxide film developed on the sample due to cerium's rapid oxidation rate. After the polycrystalline section of the sample was removed with a spark cutter, the oxide film was cleaned off using a 50% solution of HNO_3. The sample was then sealed in a thin walled aluminum container and kept under high vacuum or in a helium atmosphere throughout the experiment.

The phonon and magnetic excitation data were collected at two different installations, Ames Laboratory, Ames, Iowa and Oak Ridge National Laboratory, Oak Ridge, Tennessee. Measurements were begun using the Ames Laboratory Research Reactor, ALRR, which is a CP-5 type reactor operated at 5 Megawatts. Cerium's low coherent scattering cross section coupled with the intensity loss due to resolution effects as the zone boundary is approached prohibited completion of the experiment at Ames Laboratory. The measurements were finished using the High Flux Isotope Reactor, HFIR, at Oak Ridge National Laboratory. This reactor operates at 100 Megawatts.

All of the measurements reported here were taken at room temperature and nearly all the scans used a neutron energy loss (phonon creation) process. (See data tabulations in Table 2.2 and Appendix B.) Virtually all of the Ames Laboratory data were found to agree within error with those taken at Oak Ridge. Therefore, most of the data used for the analysis (Table 2.2) were ORNL data because they represent the largest collection of data obtained under consistent experimental conditions. Data obtained at Ames Laboratory are tabulated in Appendix B for comparison. The experimental conditions under which the Ames Laboratory data were taken are therefore described only briefly below. The experimental conditions under which the HFIR data were obtained are then presented in somewhat more detail.

Measurements at Ames Laboratory were begun on a triple axis spectrometer which was built by Mitsubishi Electric Company and modified by Ames Laboratory. Pyrolytic graphite was used for both the monochromator and analyzer. The instrument was operated in a fixed E_0, variable E' mode. The incident neutron wavelength was $\lambda_0 = 2.455$ Å, corresponding to an incident frequency $\nu_0 = 8.4$ THz. Since most of the cerium phonons have frequencies below 3 THz, the match between $|\vec{K}_0|$, $|\vec{K}'|$, and $|\vec{q}|$ was not very good, producing poor resolution. No filters were used with the Mitsubishi spectrometer and higher order contaminations in the beam coupled with the above resolution effect produced ambiguities in much of the data obtained with this instrument. The experiment was moved to a second spectrometer, the Triax, when it became available.

The Triax, which was built by Ames Laboratory, was operated in the fixed E', variable E_0 mode. This allowed much more flexibility to match

$|\vec{K}|$ and $|\vec{K}_0|$ with $|\vec{q}|$, and to choose λ_0 corresponding more closely to the 1 Å peak in the Maxwellian neutron energy spectrum produced by the reactor. A pyrolytic graphite monochromator and analyzer were used, and a pyrolytic graphite filter was also used thereby reducing higher order contaminations in the beam. Therefore, a significant improvement in the intensity, resolution, and general quality of the data was obtained. However, the inherent intensity problems due to cerium's low coherent scattering cross section and the poor resolution at large $\vec{q}$ values prohibited completion of the measurements at Ames. Therefore, the experiment was moved to the High Flux Isotope Reactor.

At Oak Ridge National Laboratory the HB-3 triple axis spectrometer was used. Due to the extremely high flux of the reactor, care must be taken in correctly identifying the observed scattering. Therefore, the HB-3 incorporates a second monitor placed between the sample and the analyzer to detect spurious processes. (See the discussion of spurious processes in the section on measurement techniques.) The HFIR measurements were conducted using a beryllium monochromator (101) reflection and a pyrolytic graphite analyzer (002) reflection.

The HB-3 instrument was operated in a fixed E' mode at all times. A value of $\nu' = 6$ THz was used for large $\vec{q}$ phonons, and a value of $\nu' = 3.3$ THz was used to improve the resolution for the narrower low frequency, low $\vec{q}$ phonons. A pyrolytic graphite filter was inserted between the sample and analyzer for the 3.3 THz measurements due to the increased probability of detection of contaminations at this frequency. (Recall that a second order process in the monochromator will scatter

neutrons at an energy of $4E_0$. To measure a phonon with a frequency of 2 THz with a neutron energy loss process E_0, must be 5.3 THz if E' is 3.3 THz. Therefore, E_0 is low enough that a significant flux of neutrons with an energy of $4E_0$ is present in the reactor spectrum. Thus, measurements conducted with E' = 3.3 THz are much more susceptible to contamination problems than measurements performed with E' = 6 THz.)

As previously mentioned, nearly all the Triax phonons were remeasured with the HB-3. All reliable Triax measurements agree within error with HFIR measurements except for several L [001] phonons. Here the HB-3 data are systematically lower by approximately 5% through the middle one-third of the zone. The L [001] phonons from the HB-3 data were incorporated in the analysis as they were self-consistent and HB-3 data in general were in excellent agreement with the Triax data on all other branches. (It should be noted that the area of discrepancy contained only two phonons from the Triax data which were considered to be reliable.)

The data used for the lattice dynamical analysis are presented in Table 2.2. All phonons listed there are HB-3 data except those designated as Triax data. The wave vector for each phonon is given in terms of the reduced wave vector unit ξ defined by $\vec{q} = \frac{2\pi}{a}\xi$. $\vec{\tau}$ is the reciprocal lattice point about which the given phonon was measured.

Approximately 35% of the HB-3 phonon centers were determined with a peak fitting program. Several phonons near the zone boundary were broad and centers were too ill-defined to be determined accurately by eye. The fitting program was originally used for these phonons. The

Table 2.2. Phonon frequencies used in lattice dynamical analysis

Branch	$\vec{q}$ (ξ units)	ν (THz)[a]	$\pm\Delta\nu$ (THz)	$\vec{\tau}$ (2 π/a)
L [001]	.1	.345	.02	002
	.15	.52	.02	002
	.2	.76[b]	.03	002
	.3	1.04	.06	004
	.4	1.35	.06	004
	.5	1.70	.07	004
	.6	2.04	.07	004
	.7	2.45[b]	.05	002
	.8	2.72	.08	004
	.9	2.94	.08	004
	1.0	3.04	.07	004
T [001]	.1	.29	.01	$\bar{2}02$
	.2	.60	.015	$\bar{2}02$
	.3	.97	.025	220
	.4	1.27	.02	220
	.5	1.50[b]	.04	220
	.6	1.735[b]	.04	220
	.7	1.99	.05	220
	.8	2.04	.06	220
	.9	2.10	.09	220
L [110]	.1	.58	.02	220
	.2	1.28[b]	.03	220
	.3	1.735[b]	.025	220
	.4	2.09[b]	.03	220
	.5	2.20[b]	.05	220
	.6	2.20[b]	.04	220
	.7	2.19	.06	220
	.8	2.15	.05	220
	.9	2.04	.06	220
	1.0	2.05	.06	220

[a]All phonons listed in this table were obtained with neutron energy loss, fixed E'.

[b]From Triax measurements - all other phonon frequencies listed are from HB-3 measurements.

Table 2.2. Continued

Branch	$\vec{q}$ (ξ units)	ν (THz)[a]	±Δν (THz)	$\vec{\tau}$ (2 π/a)
T_2 110	.1	.47	.01	002
	.15	.70	.01	002
	.2	.95[b]	.01	002
	.3	1.41	.02	004
	.4	1.79	.02	004
	.5	2.13	.04	004
	.6	2.30	.06	004
	.7	2.59	.07	004
	.8	2.82	.07	004
	.9	2.90	.07	004
T_1 [110]	.1	.27	.01	$\bar{2}02$
	.15	.40	.01	$\bar{2}02$
	.2	.54	.01	$\bar{2}02$
	.3	.825	.02	$\bar{2}02$
	.4	1.09	.03	$\bar{2}02$
	.5	1.30	.03	$\bar{2}02$
	.6	1.43	.05	$\bar{2}02$
	.7	1.62	.07	$\bar{2}02$
	.8	1.79	.05	$\bar{2}02$
	.9	1.85	.06	$\bar{2}02$
L [111]	.1	.84	.04	222
	.15	1.20	.05	222
	.2	1.55	.06	222
	.3	2.27	.08	222
	.4	2.66	.08	222
	.5	2.75	.07	222
T [111]	.1	.425	.01	222
	.15	.60	.01	222
	.2	.755	.015	222
	.3	.99	.03	222
	.4	.825	.025	222
	.5	.75	.03	222

other phonons fit with the program served as a check on the visual center determinations. The center values given by the program for these "double checked" phonons agreed well within error with the centers determined visually. The errors listed in Table 2.2 were also obtained visually. Several typical phonons are shown in Figure 2.6.

The dispersion curves constructed from the measured phonons are given in Figure 2.7. The line through the points is a hand drawn smoothed curve and does not represent any fitting procedure. Fitting of the dispersion curves to various models is discussed in Chapter III. First, however, a brief summary of the magnetic inelastic measurements is given below.

Spurious structure observed during phonon measurements conducted with the Mitsubishi prompted investigation of magnetic excitations in γ-Ce. Considerable disagreement over the nature of magnetic scattering in γ-Ce exists in the literature (36-38) and values listed for possible discrete magnetic excitations ranged from 1.4-2.56 THz. Several preliminary scans through the appropriate energy range were performed at Ames with inconclusive results.

A series of constant-Q measurements at "zone center equivalent" lattice points was performed at ORNL. Comparison of a set of scans with $Q = (1,1,1)$, $Q = (2,2,2)$, and $Q = (3,3,3)$, for example, allows for identification of any peaks exhibiting a Q dependence in their intensity given by $|f(\vec{Q})|^2$. This particular scan series is shown in Figure 2.8. Although some structure in the background was observed in several of the "magnetic" scans, the data did not consistently indicate a scattering

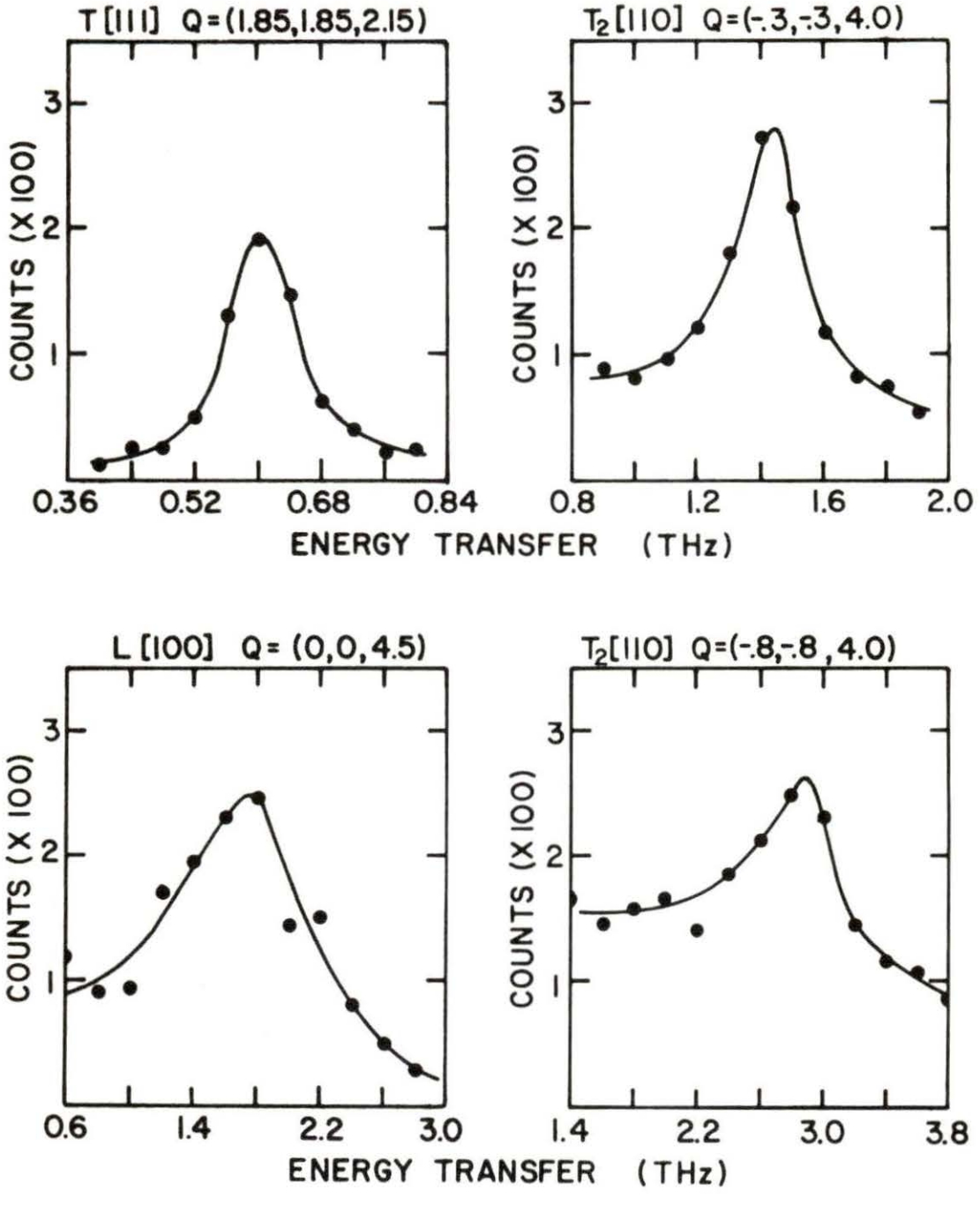

Figure 2.6. Representative γ-Ce phonons from various branches. Notice the broadening of the transverse modes for large Q values

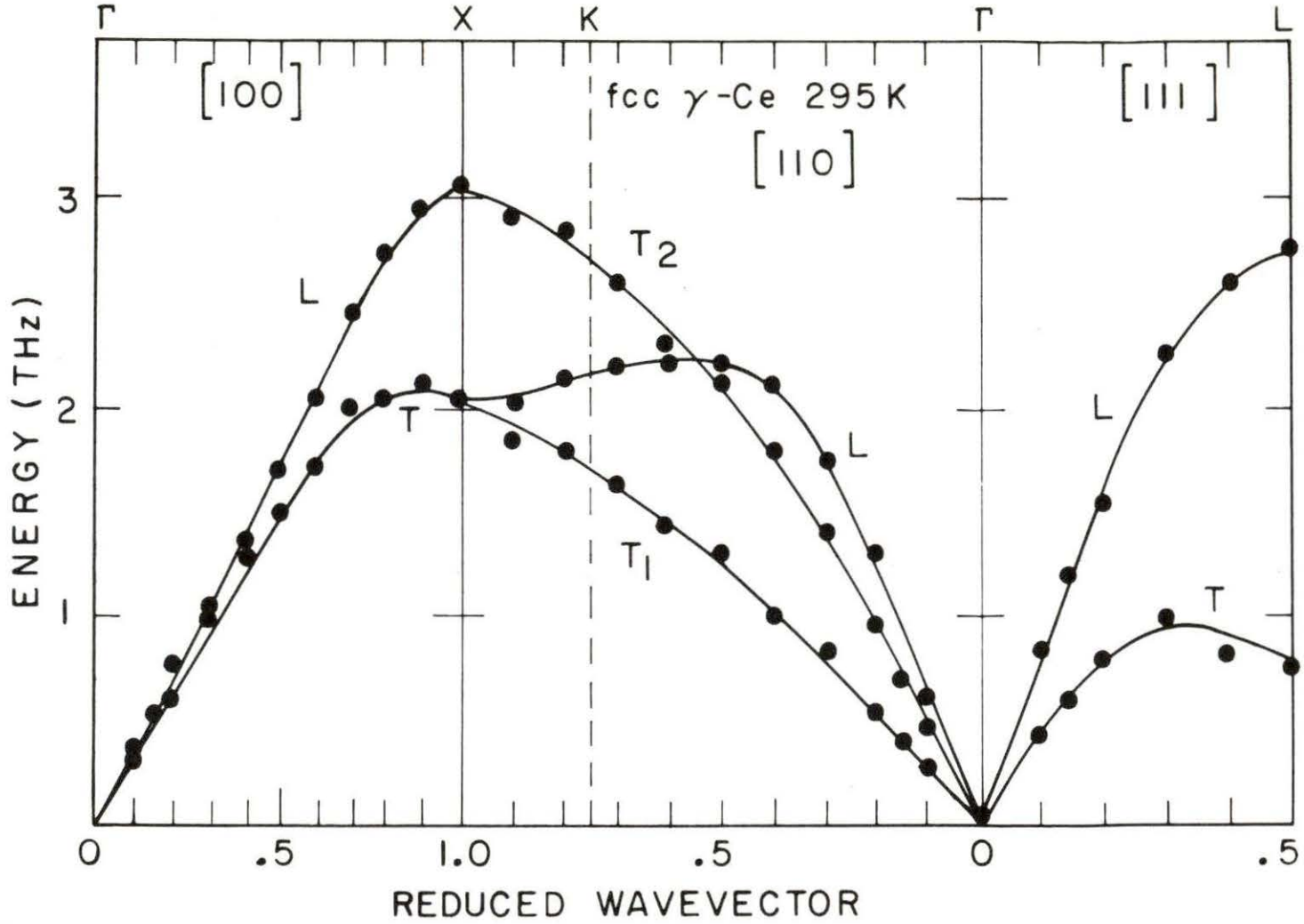

Figure 2.7. Experimentally determined dispersion curves of γ-Ce for the three symmetry directions. The lines are hand-drawn and do not represent a fitting procedure

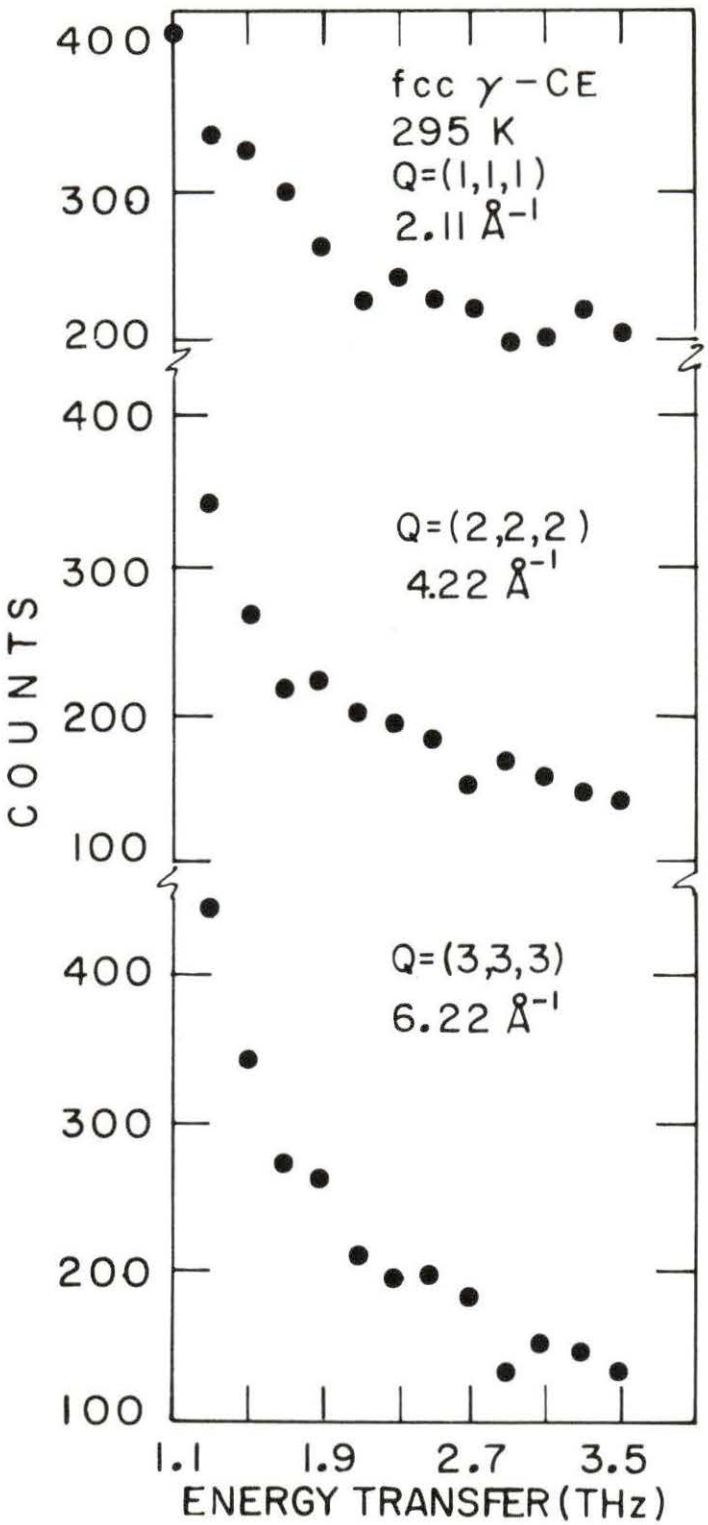

Figure 2.8. Inelastic magnetic scattering from γ-Ce. No discrete peaks exhibiting an intensity variation given by $|f(\vec{Q})|^2$ are observed

which could be construed to arise from a discrete magnetic excitation in cerium. However, useful information was extracted from the observed magnetic scattering. Analysis of the magnetic scattering is included in Chapter III following the discussion of the lattice dynamical analysis.

CHAPTER III. ANALYSIS

Dispersion Curve Fitting

In order to extract elastic and thermodynamic properties from the experimentally determined dispersion curves, the phonon data must be fit with a suitable force model. This procedure yields the elastic constants (if they are not already known) and the interatomic force constants. The interatomic force constants can in turn be used together with the relevant dispersion relations to generate the phonon density of states. From the density of states the temperature variation of the lattice specific heat and of the Debye temperature can be calculated. Therefore, the fitting procedure is described first in this section. Then the density of states and calculated thermodynamic properties are discussed and the results are compared with previous experimental results obtained from measurements on polycrystalline samples. Chapter III concludes with the analysis of the magnetic scattering data.

In the present work the experimental dispersion curves (Figure 2.7) were fit with the Born-von Kármán force model discussed in Chapter I. The complicated interactions of the localized electrons, conduction electrons, and ion cores, which produce the interatomic forces in a metal, are unknown and are phenomenologically represented by the interatomic force constants. Therefore, the interatomic force constants obtained by fitting the dispersion curves of a metal have little physical significance and should be regarded as fitting parameters. Their usefulness

lies in that they can be used with the phenomenological dispersion relation [Equation (1.24)] to calculate a phonon density of states which is consistent with the measured dispersion curves. In order to obtain the best fit possible with the computer program which was available, interatomic force constants out to eight nearest neighbors were included in the fitting procedure for γ-Ce.

Before discussing the fitting procedure itself, it is useful to examine the simplified form in which the dynamical matrix and equation of motion can be written for the three symmetry directions of an fcc lattice. The relationships between basic parameters involved in the fitting procedure are then discussed in order to clarify the description of the fitting procedure presented thereafter. Following the discussion of these topics, the results for the Born-von Kármán fitting of γ-Ce are presented.

The expression for the dynamical matrix can be simplified by translational invariance and inversion symmetry. Writing Equation (1.30) with the "self force constant", $\varphi_{\alpha\beta}(\ell\ell)$, written separately from the rest of the sum, one obtains

$$D_{\alpha\beta}(\vec{q}) = \varphi_{\alpha\beta}(\ell\ell) + \sum_{\ell'\neq\ell} \varphi_{\alpha\beta}(\ell, \ell')e^{-iq\cdot[\vec{R}(\ell)-\vec{R}(\ell')]} \quad . \qquad (3.1)$$

From translational invariance the "self term" is given by Equation (1.13).

$$\varphi_{\alpha\beta}(\ell\ell) = - \sum_{\ell'\neq\ell} \varphi_{\alpha\beta}(\ell\ell')$$

Therefore, the dynamical matrix may be written as

$$D_{\alpha\beta}(\vec{q}) = - \sum_{\ell' \neq \ell} \varphi_{\alpha\beta}(\ell\ell') + \sum_{\ell' \neq \ell} \varphi_{\alpha\beta}(\ell\ell') e^{-i\vec{q}\cdot[\vec{R}(\ell)-\vec{R}(\ell')]} \quad . \tag{3.2}$$

Each point in an fcc lattice is a point of inversion symmetry. Therefore,

$$\varphi_{\alpha\beta}(\ell\ell') = \varphi_{\alpha\beta}(\ell - \ell') \quad . \tag{3.3}$$

Equation (3.2) becomes,

$$\begin{aligned} D_{\alpha\beta}(\vec{q}) &= - \sum_{\ell' \neq \ell} \varphi_{\alpha\beta}(\ell\ell') + \tfrac{1}{2} \sum_{\ell' \neq \ell} \varphi_{\alpha\beta}(\ell\ell')(e^{-iq\cdot[R(\ell)-R(\ell')]} \\ &\quad + e^{i\vec{q}\cdot[\vec{R}(\ell)-\vec{R}(\ell')]}) \\ &= - \sum_{\ell' \neq \ell} \varphi_{\alpha\beta}(\ell\ell') + \tfrac{1}{2} \sum_{\ell' \neq \ell} \varphi_{\alpha\beta}(\ell\ell') 2 \cos(\vec{q}\cdot[\vec{R}(\ell) - \vec{R}(\ell')]) \\ &= - \sum_{\ell' \neq \ell} \varphi_{\alpha\beta}(\ell\ell')\{1 - \cos(\vec{q}\cdot[\vec{R}(\ell) - \vec{R}(\ell')])\} \quad . \end{aligned} \tag{3.4}$$

Recall from Chapter II that the dynamical matrix factors for lattice vibrations propagating in the three symmetry directions of an fcc lattice. The physical interpretation of the factorization of the dynamical matrix is that phonons propagating in the symmetry directions correspond to entire planes of atoms vibrating in phase. For example, an [001] phonon corresponds to a lattice motion in which every atom in a given (001) plane vibrates in phase with every other atom of the designated (001) plane. The mathematics of the problem therefore reduces to a one-dimensional analog with each particle in a linear chain representing a whole plane of atoms. The force constants between successive "particles" in the one-dimensional analog correspond to the force constants

between successive planes of atoms in the real crystal. These interplanar force constants are linear combinations of the interatomic force constants (hereafter denoted as AFC's).

The expression for the dynamical matrix for modes in the three symmetry directions may be simplified in the following manner. Consider a series of {001} planes and a reference atom at $R(\ell) = 0$. Every atom in the two (001) planes adjacent to the plane containing the origin will have the same $\vec{q} \cdot \vec{R}(\ell')$ value given by

$$\vec{q} \cdot \vec{R}(\ell') = |\vec{q}|d \quad . \tag{3.5}$$

Here d is the perpendicular distance from the original plane to the first plane on either side.

In terms of the reciprocal lattice, d may be written as

$$d = 2\pi/\tau_{\vec{q}} \quad , \tag{3.6}$$

where $\tau_{\vec{q}}$ is the reciprocal lattice vector connecting the designated origin and the nearest reciprocal lattice point in the direction of $\vec{q}$. Recall that $\vec{q}$ may always be written in terms of the reduced wave vector coordinate, $\vec{\xi}$, as defined in Chapter II. Thus Equation (3.5) becomes

$$|\vec{q}|d = \frac{2\pi}{a} |\vec{\xi}| \frac{2\pi}{\tau_{\vec{q}}} \quad . \tag{3.7}$$

The boundary of the first Brillioun zone lies halfway between the origin and the nearest lattice point in the direction of $\tau_{\vec{q}}$ (see Figures 2.3 and 2.4). Therefore,

$$\vec{\tau}_{\vec{q}}/2 = \vec{q}_{max} = \frac{2\pi}{a}\vec{\xi}_{max} \quad , \tag{3.8}$$

where $\vec{q}_{max}$ is the wave vector of a zone boundary phonon. Equation (3.7) may be written as

$$|\vec{q}|d = \frac{\pi|\vec{\xi}|}{|\vec{\xi}_{max}|} = \frac{\pi\xi}{\xi_m} \quad . \tag{3.9}$$

If planes of atoms successively further away from the original plane are designated by integers p, p+1, p+2, ..., etc., Equation (3.9) is readily generalized to

$$|\vec{q}|d_p = \frac{p\pi\xi}{\xi_m} \quad . \tag{3.10}$$

The dynamical matrix can therefore be rewritten in terms of the interplanar force constants and ξ yielding

$$D_j(\xi) = -\sum_p \Phi'_p(j)\left[1 - \cos\left(\frac{p\pi\xi}{\xi_m}\right)\right] \quad .[1] \tag{3.11}$$

Here $\Phi'_p(j)$ is the sum of all the AFC's, $\varphi_{\alpha\beta}$, between the reference atom at the origin and the atoms in the p-th plane on either side of it. The summation extends over pairs of planes which are successively further away from the original plane on opposite sides of it.

The equation of motion [Equation (1.29)] for a given mode, j, becomes

---

[1] Representing the interplanar force constants with a capital phi (Φ) is fairly standard notation and has therefore been adopted in the present work. These Φ's are not to be confused with the potential energy function denoted by Φ in Chapter I.

$$M_k \omega_j^2(\xi) = \sum_p \Phi_p(j) \left[1 - \cos\left(\frac{p\pi\xi}{\xi_m} \right) \right] \quad . \tag{3.12}$$

The $\Phi_p(j)$ are the interplanar force constants and are equal to the negative of the $\Phi'_p(j)$'s of Equation (3.11). In practical fitting procedures the number of AFC's included in the summation which yields $\Phi_p(j)$ depends on the number of nearest neighbors to be included in the fit.

A rigorous derivation of the AFC composition of the $\Phi_p(j)$'s for each symmetry mode of an fcc lattice (39) will not be repeated here. The results to eight nearest neighbors (8NN) are given in Table 3.1 (31). Each row gives the coefficients of the designated AFC's in the summation that yields the corresponding $\Phi_p(j)$. For example, the interplanar force constant between a reference {001} plane and the first two planes on either side for a L [001] mode is given by

$$\Phi_1(L\ [001]) = 8(1XX) + 16(3YY) + 8(5YY) + 16(7ZZ) \quad . \tag{3.13}$$

In order to illustrate the origin of the coefficients listed in Table 3.1, consider the following simple example. For the unit cell shown in Figure 3.1, the first {010}-type plane adjacent to the reference plane contains two first nearest neighbors to the atom at the origin. These two first nearest neighbors are labeled 1 and 2. Adding the other unit cells that surround the origin, one obtains a total of 8 first nearest neighbors in the closest {010}-type planes on either side of the reference plane. All of the first nearest neighbor positions in these planes can be generated by performing appropriate

Table 3.1. 8NN AFC composition of the interplanar force constants, $\Phi_p(j)$, and of the elastic constants, c_{ij}, of an fcc crystal

j	$\Phi_p(j)$	AFC's											
		1XX	1ZZ	1XY	2XX	2YY	3XX	3YY	3YZ	3XZ	4XX	4ZZ	4XY
T [001]	Φ_1	4	4	0	0	0	8	8	0	0	0	0	0
	Φ_2	0	0	0	0	2	0	8	0	0	4	4	0
	Φ_3	0	0	0	0	0	0	0	0	0	0	0	0
	Φ_4	0	0	0	0	0	0	0	0	0	0	0	0
L [001]	Φ_1	8	0	0	0	0	0	16	0	0	0	0	0
	Φ_2	0	0	0	2	0	8	0	0	0	8	0	0
	Φ_3	0	0	0	0	0	0	0	0	0	0	0	0
	Φ_4	0	0	0	0	0	0	0	0	0	0	0	0
T [111]	Φ_1	4	2	-2	2	4	4	8	4	0	0	0	0
	Φ_2	0	0	0	0	0	2	4	-2	-4	4	2	-2
	Φ_3	0	0	0	0	0	0	0	0	0	0	0	0
L [111]	Φ_1	4	2	4	2	4	4	8	-8	0	0	0	0
	Φ_2	0	0	0	0	0	2	4	4	8	4	2	4
	Φ_3	0	0	0	0	0	0	0	0	0	0	0	0
T_2 [110]	Φ_1	8	0	0	0	0	0	8	0	0	0	0	0
	Φ_2	0	2	0	0	4	4	0	0	0	8	0	0
	Φ_3	0	0	0	0	0	0	8	0	0	0	0	0
	Φ_4	0	0	0	0	0	0	0	0	0	0	2	0
	Φ_5	0	0	0	0	0	0	0	0	0	0	0	0
T_1 [110]	Φ_1	4	4	0	0	0	4	4	0	8	0	0	0
	Φ_2	2	0	-2	2	2	0	4	-4	0	4	4	0
	Φ_3	0	0	0	0	0	4	4	0	-8	0	0	0
	Φ_4	0	0	0	0	0	0	0	0	0	2	0	-2
	Φ_5	0	0	0	0	0	0	0	0	0	0	0	0
L [110]	Φ_1	4	4	0	0	0	4	4	0	-8	0	0	0
	Φ_2	2	0	2	2	2	0	4	4	0	4	4	0
	Φ_3	0	0	0	0	0	4	4	0	8	0	0	0
	Φ_4	0	0	0	0	0	0	0	0	0	2	0	2
	Φ_5	0	0	0	0	0	0	0	0	0	0	0	0
Λ [0ξ1]	Φ_0	8	8	0	0	0	16	16	0	0	0	0	0
	Φ_1	0	0	0	0	0	0	0	0	0	0	0	0
	Φ_2	0	0	0	2	0	-8	0	0	0	8	0	0
	Φ_3	0	0	0	0	0	0	0	0	0	0	0	0
	Φ_4	0	0	0	0	0	0	0	0	0	0	0	0
π [0ξ1]	Φ_0	16	0	0	0	0	0	32	0	0	0	0	0
	Φ_1	-4	4	0	0	0	8	-8	0	0	0	0	0
	Φ_2	0	0	0	0	2	0	-8	0	0	4	4	0
	Φ_3	0	0	0	0	0	0	0	0	0	0	0	0
	Φ_4	0	0	0	0	0	0	0	0	0	0	0	0
c_{ij}	c_{11}	4	0	0	4	0	16	8	0	0	16	0	0
	c_{44}	2	2	0	0	4	4	20	0	0	8	8	0
	c_{12}	-2	-2	4	0	-4	-4	-20	8	32	-8	-8	16

AFC's													
5XX	5YY	5ZZ	5XY	6XX	6YZ	7XX	7YY	7ZZ	7YZ	7XZ	7XY	8XX	8YY
4	0	4	0	0	0	8	8	0	0	0	0	0	0
0	0	0	0	8	0	8	0	8	0	0	0	0	0
0	4	4	0	0	0	0	8	8	0	0	0	0	0
0	0	0	0	0	0	0	0	0	0	0	0	0	2
0	8	0	0	0	0	0	0	16	0	0	0	0	0
0	0	0	0	8	0	0	16	0	0	0	0	0	0
8	0	0	0	0	0	16	0	0	0	0	0	0	0
0	0	0	0	0	0	0	0	0	0	0	0	2	0
4	4	4	4	6	2	4	4	4	4	-4	4	0	0
4	4	4	-4	0	0	4	4	4	4	4	-4	2	4
0	0	0	0	2	-2	4	4	4	-4	-4	-4	0	0
4	4	4	-8	6	-4	4	4	4	-8	8	-8	0	0
4	4	4	8	0	0	4	4	4	-8	-8	8	2	4
0	0	0	0	2	4	4	4	4	8	8	8	0	0
8	0	0	0	0	0	8	0	8	0	0	0	0	0
0	0	4	0	0	0	0	8	0	0	0	0	0	0
0	8	0	0	0	0	8	0	0	0	0	0	0	0
0	0	4	0	4	0	0	8	0	0	0	0	2	4
0	0	0	0	0	0	0	0	8	0	0	0	0	0
0	4	4	0	0	0	4	8	4	8	0	8	0	0
2	2	0	4	0	0	4	0	4	0	8	0	0	0
4	0	4	0	0	0	0	4	4	-8	0	0	0	0
2	2	0	-4	4	-4	4	0	4	0	-8	0	2	2
0	0	0	0	0	0	4	4	0	0	0	-8	0	0
0	4	4	0	0	0	4	8	4	-8	0	-8	0	0
2	2	0	-4	0	0	4	0	4	0	-8	0	0	0
4	0	4	0	0	0	0	4	4	8	0	0	0	0
2	2	0	4	4	4	4	0	4	0	8	0	2	2
0	0	0	0	0	0	4	4	0	0	0	8	0	0
8	8	16	0	0	0	16	32	16	0	0	0	0	0
0	0	0	0	0	0	0	0	0	0	0	0	0	0
0	0	0	0	8	0	0	-16	0	0	0	0	0	0
0	0	0	0	0	0	0	0	0	0	0	0	0	0
0	0	0	0	0	0	0	0	0	0	0	0	2	0
16	16	0	0	0	0	32	0	32	0	0	0	0	0
-4	0	4	0	0	0	-8	8	0	0	0	0	0	0
0	0	0	0	8	0	-8	0	-8	0	0	0	0	0
0	-4	4	0	0	0	0	8	-8	0	0	0	0	0
0	0	0	0	0	0	0	0	0	0	0	0	0	2
36	4	0	0	16	0	72	32	8	0	0	0	16	0
2	18	20	0	16	0	20	40	52	0	0	0	0	16
-2	-18	-20	24	-16	32	-20	-40	-52	32	48	96	0	-16

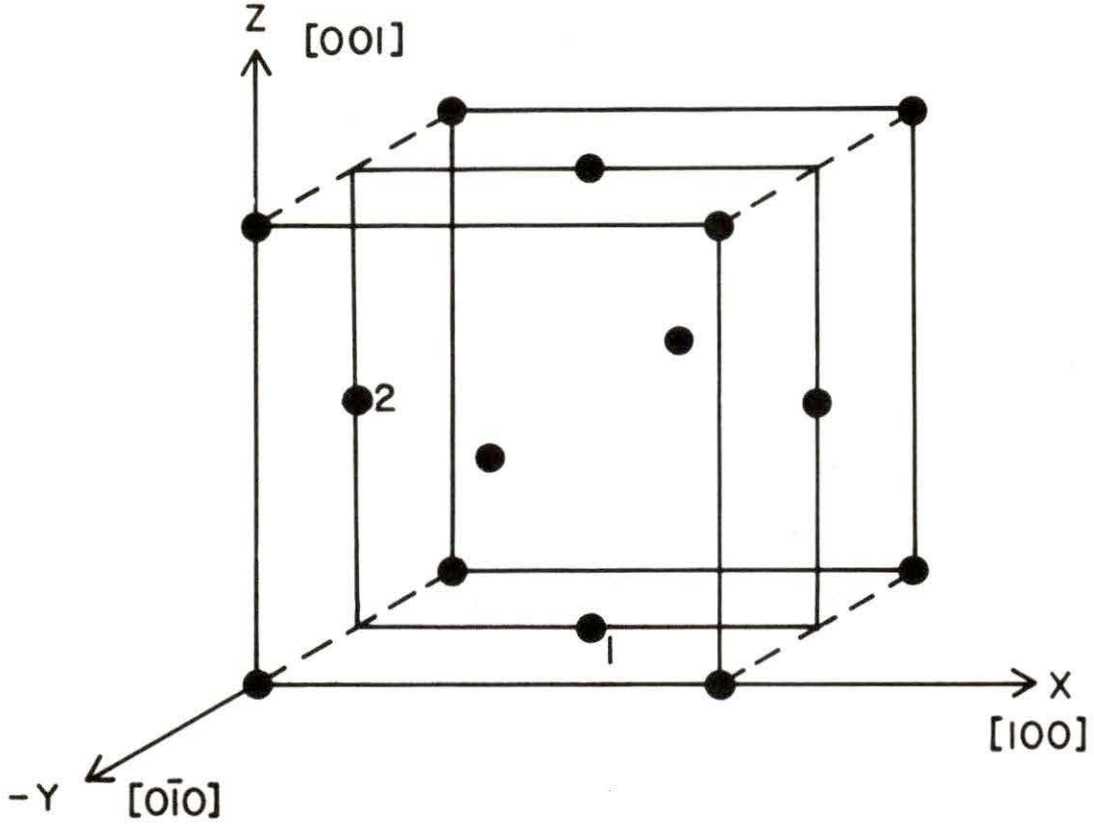

Figure 3.1. {010}-type planes of an fcc monatomic lattice shown with respect to the cubic unit cell. The first plane from the origin contains two first nearest neighbors to the atom at the origin numbered 1 and 2

symmetry operations on the position of atom 1. Therefore, the matrix $\varphi^n_{\alpha\beta}$ which gives the AFC's between the atom at the origin and the n-th first neighbor can be generated by applying appropriate symmetry operations to $\varphi^1_{\alpha\beta}$. Recall from Chapter 1, [Equation (1.55)]

$$\varphi^1_{\alpha\beta} = \begin{pmatrix} xx & xy & 0 \\ xy & xx & 0 \\ 0 & 0 & zz \end{pmatrix} \quad .$$

$\varphi^2_{\alpha\beta}$ can be generated by applying a rotation of $\pi/2$ about the y axis.

$$\varphi^2_{\alpha\beta} = \begin{pmatrix} 0 & 0 & 1 \\ 0 & 1 & 0 \\ -1 & 0 & 0 \end{pmatrix} \begin{pmatrix} xx & xy & 0 \\ xy & xx & 0 \\ 0 & 0 & zz \end{pmatrix} \begin{pmatrix} 0 & 0 & -1 \\ 0 & 1 & 0 \\ 1 & 0 & 0 \end{pmatrix} \quad . \tag{3.14}$$

Therefore,

$$\varphi^2_{\alpha\beta} = \begin{pmatrix} zz & 0 & 0 \\ 0 & xx & -xy \\ 0 & -xy & xx \end{pmatrix} \quad . \tag{3.15}$$

Performing the symmetry operations that generate the six other first neighbor positions, one obtains

$$\varphi^3_{\alpha\beta} = \begin{pmatrix} xx & -xy & 0 \\ -xy & xx & 0 \\ 0 & 0 & zz \end{pmatrix} \tag{3.16}$$

$$\varphi^4_{\alpha\beta} = \begin{pmatrix} zz & 0 & 0 \\ 0 & xx & xy \\ 0 & xy & xx \end{pmatrix} \tag{3.17}$$

$$\varphi^5_{\alpha\beta} = \begin{pmatrix} xx & xy & 0 \\ xx & xy & 0 \\ 0 & 0 & zz \end{pmatrix} \tag{3.18}$$

$$\varphi^6_{\alpha\beta} = \begin{pmatrix} xx & -xy & 0 \\ -xy & xx & 0 \\ 0 & 0 & zz \end{pmatrix} \tag{3.19}$$

$$\varphi^{7}_{\alpha\beta} = \begin{pmatrix} zz & 0 & 0 \\ 0 & xx & xy \\ 0 & xy & xx \end{pmatrix} \tag{3.20}$$

$$\varphi^{8}_{\alpha\beta} = \begin{pmatrix} zz & 0 & 0 \\ 0 & xx & -xy \\ 0 & -xy & xx \end{pmatrix} \tag{3.21}$$

The summation of these $\varphi^{n}_{\alpha\beta}$'s gives the first neighbor AFC composition of the interplanar force constants between the designated planes for [010] modes. The resultant matrix is given below.

$$\begin{pmatrix} (4xx + 4zz) & 0 & 0 \\ 0 & 8xx & 0 \\ 0 & 0 & (4xx + 4zz) \end{pmatrix}$$

An examination of the displacements associated with a transverse [010] mode reveals that only φ_{xx} and φ_{zz} will be involved. A longitudinal [010] vibration involves φ_{yy} which is equal to φ_{xx} for the first nearest neighbor. (See Chapter I, Symmetry Considerations.) Therefore, the elements (4xx + 4zz) of the above matrix are associated with $\Phi_1(T\ [010]) = \Phi_1(T\ [001])$, for the two transverse modes. The 8xx term is associated with $\Phi_1(L\ [010]) = \Phi_1(L\ [001])$ as given in Table 3.1.

In order to include the desired number of neighbors in a practical fitting procedure, a sufficient number of interplanar force constants must be included in the summation over planes in Equation (3.12). For example, the eighth nearest neighbor of the atom at the origin in Figure 3.1 is at a distance of 2a along the cube edge. (See Figure A.1.) Therefore, there is no eighth neighbor in the first, second, or third successive planes from the reference plane. Thus, Φ_4 must be included

for transverse and longitudinal [001] modes in order to incorporate 8NN AFC's into the analysis.

Table 3.1 also contains the AFC composition for two modes in the [0ξ1] direction. In an fcc crystal this direction lies along the X-W line on the surface of the first Brillioun zone (see Figure 2.2). Lattice vibrational modes propagating in the [0ξ1] direction are not purely longitudinal or transverse. However, their polarizations are governed entirely by symmetry (40), therefore, the dynamical matrix factors for these modes in a manner analogous to the factorization obtained for the [001], [110], and [111] directions. Hence, [0ξ1] interplanar force constants may be obtained from the linear combinations of AFC's given in Table 3.1. Working through the mathematics one obtains "self-terms" for these modes which are called zero plane force constants, Φ_0. The equation of motion for [0ξ1] modes therefore becomes

$$M_k \omega_j^2(\xi) = \Phi_0 + \sum_p \Phi_p(j) \left[1 - \cos\left(\frac{p\pi\xi}{\xi_m} \right) \right] \quad . \tag{3.22}$$

The [0ξ1] modes of γ-Ce have not yet been measured, however, they are discussed further in connection with the density of states which was obtained for γ-Ce.

The AFC composition of the elastic constants given in Table 3.1 are obtained by considering the long wavelength limit of lattice vibrations. If the wavelength of a lattice wave propagating in a given symmetry direction is very long compared to the interatomic spacing, the problem becomes one of non-dispersive wave propagation in an elastic medium (41).

Therefore, as $\xi \to 0$, Equation (3.12) must become the equation of motion for the corresponding acoustic vibration.

The velocity of an acoustic vibration is given by

$$V_j^2 = \frac{C_j}{\rho} = \frac{\omega^2}{q^2} \quad , \tag{3.23}$$

where ρ is the density of the crystal and C_j is the elastic constant (or linear combination of elastic constants) associated with the mode j. For cubic crystals there are three independent elastic constants, c_{11}, c_{44}, c_{12}, which are associated with the various phonon branches as indicated in Table 3.2.

Table 3.2. Elastic constants associated with each symmetry direction of a cubic crystal

Branch	$\rho V_j^2 = C_j (\xi \to 0)$
T [001]	c_{44}
L [001]	c_{11}
T [111]	$\frac{1}{3}(c_{11} - c_{12} + c_{44})$
L [111]	$\frac{1}{3}(c_{11} + 2c_{12} + 4c_{44})$
T_2 [110]	c_{44}
T_1 [110]	$\frac{1}{2}(c_{11} - c_{12})$
L [110]	$\frac{1}{2}(c_{11} + c_{12} + 2c_{44})$

Equation (3.23) may be solved for ω^2 in terms of C_j, and ξ.

$$\omega^2 = \frac{C_j q^2}{\rho} = \left(\frac{C_j}{\rho} \frac{4\pi^2 \xi^2}{a^2} \right) \tag{3.24}$$

A monatomic fcc crystal contains four atoms per primitive cubic cell. Therefore, the density is given by

$$\rho = \frac{4M_k}{a^3} \quad . \tag{3.25}$$

Substituting these values into Equation (3.12) and expanding the cosine term in the small ξ limit, one obtains

$$\frac{a^3}{4} \rho \left(\frac{C_j}{\rho} \frac{4\pi^2 \xi^2}{a^2} \right) = \sum_p \Phi_p(j) \left[1 - \left(1 - \frac{p^2 \pi^2 \xi^2}{2\xi_m^2} + \ldots \right) \right]$$

$$(aC_j)(\xi_m^2) = \sum_p \Phi_p(j) \frac{p^2}{2} \quad . \tag{3.26}$$

Therefore, the elastic constants can be obtained from the interplanar force constants which in turn will give the AFC composition of each elastic constant. (If C_j represents a combination of elastic constants, a set of n equations corresponding to Equation (3.26), written for n different modes, must be solved simultaneously to yield the individual elastic constants.)

As an example, consider the AFC composition of the c_{44} elastic constant. The velocity of the T [001] mode as $\xi \to 0$ is equal to $\sqrt{\frac{c_{44}}{\rho}}$ (see Table 3.2). Therefore, c_{44} is given by a summation of T [001]

interplanar force constants. From Equation (3.26) we have

$$ac_{44}(\xi_{T\ [001]m})^2 = \tfrac{1}{2}\,\Phi_1(T\ [001]) + 2\,\Phi_2(T\ [001]) + \ldots \quad . \tag{3.27}$$

For the [001] direction $\xi_m^2 = 1$ (see Figure 2.3). Therefore, substituting the AFC composition of Φ_1 and Φ_2 into Equation (3.27), one obtains

$$ac_{44} = \tfrac{1}{2}(4(1XX) + 4(1ZZ) + 8(3XX) + 8(3YY) + \ldots)$$
$$+ 2(2(2YY) + 8(3YY) + 4(4XX) + 4(4ZZ) + \ldots)$$

$$ac_{44} = 2(1XX) + 2(1ZZ) + 4(2YY) + 4(3XX) + 20(3YY) + 8(4XX) + 8(4ZZ) + \ldots, \tag{3.28}$$

as given in Table 3.1.

If the elastic constants have been measured they provide additional parameters which can be added to the fitting procedures. If they are not known the fitting procedure may be used to calculate elastic constant values which are consistent with the fit made to the dispersion curves.

The fitting program used in the present analysis was a linear least squares fitting program obtained from McMasters University, Ontario, Canada. In principle Equation (3.12) is satisfied for every measured frequency, ω_i. In order to obtain a least squares fit to the data, the program minimizes the expression

$$\sigma^2 = \sum_i W(i)(M_k\omega(i)^2 - \sum_n \varphi_n(i) f_n(i))^2 \quad . \tag{3.29}$$

Here W(i) is the standard least squares weight given by

$$W(i) = \left(\frac{1}{\nu_i (\Delta\nu_i)} \right)^2 \tag{3.30}$$

where ν_i if the frequency of the i-th phonon and $\Delta\nu_i$ is the error assigned to frequency ν_i. The $\varphi_n(i)$ are the AFC's and $f_n(i)$ is the fitting function.

The fitting function is obtained from the AFC composition of the interplanar force constants. The summation in the equation of motion [Equation (3.12)] may be rewritten in terms of AFC's such that

$$\sum_p \Phi_p \left(1 - \cos \frac{p\pi\xi}{\xi_m} \right) = \sum_p \left[\sum_n \alpha_{np} \varphi_n \left(1 - \cos \frac{p\pi\xi}{\xi_m} \right) \right] , \tag{3.31}$$

where the α_{np}'s are the coefficients given by each row of Table 3.1. Interchanging the summations yields

$$\sum_n \varphi_n \left[\sum_p \alpha_{np} \left(1 - \cos \frac{p\pi\xi}{\xi_m} \right) \right] . \tag{3.32}$$

Therefore, the fitting function is defined by

$$f_n(i) = \sum_p \alpha_{np} \left(1 - \cos \frac{p\pi\xi}{\xi_m} \right) . \tag{3.33}$$

Minimizing σ^2 in Equation (3.29) with respect to φ_k yields

$$\frac{\partial\sigma^2}{\partial\varphi_k} = 0 = \sum_i W(i) 2 (M_k \omega(i)^2 - \sum_n \varphi_n f_n(i)) ((-1) f_k(i))$$

$$= \sum_i W(i) M_k \omega(i)^2 f_k(i) - \sum_i W(i) \left(\sum_n \varphi_n f_n(i) f_k(k) \right) . \tag{3.34}$$

Defining the following quantities,

$$B_k = \sum_i W(i) M_k \omega(i)^2 f_k(i) \tag{3.35}$$

$$M_{n,k} = \sum_i W(i) f_n(i) f_k(i) \quad , \tag{3.36}$$

one obtains

$$0 = B_k - \sum_n M_{n,k} \varphi_n \quad . \tag{3.37}$$

All of the quantities in the summations giving B_k and $M_{n,k}$ are known. Therefore, by minimization with respect to each φ_k, B_k and $M_{n,k}$ are evaluated for each φ_k and stored as elements of a linear array and a square array respectively.

This procedure yields

$$\vec{B} = \underline{\underline{M}}\vec{\varphi} \quad , \tag{3.38}$$

and the φ's may be obtained by a standard matrix inversion

$$\underline{\underline{M}}^{-1}\vec{B} = \vec{\varphi} \quad . \tag{3.39}$$

If the AFC's are to be fit to elastic constant data as well as phonon data, the quantity to be minimized, σ'^2, is given by

$$\sigma'^2 = \sigma^2 + \sum_j W^c(j) [a C_j \xi_m^2 - \sum_n \varphi_n f_n^c(j)]^2 \quad , \tag{3.40}$$

where σ^2 is given by Equation 3.29, $W^c(j)$ is an appropriate weight, and $f_n^c(j)$ is the fitting function for the elastic constants. The elastic constant fitting function can be obtained from Equation (3.26).

$$0 = aC_j\xi_m^2 - \sum_p \Phi_p(j)\ p^2/2 \tag{3.41}$$

Writing the AFC composition of the interplanar force constants explicitly, one obtains

$$0 = aC_j\xi_m^2 - \sum_p (\sum_n \alpha_{np}\varphi_n)p^2/2$$

$$0 = aC_j\xi_m^2 - \sum_n \varphi_n \sum_p \alpha_{np}\ p^2/2$$

$$0 = aC_j\xi_m^2 - \sum_n \varphi_n f_n^c(j) \quad . \tag{3.42}$$

Minimization of Equation (3.40) with respect to φ_k yields

$$0 = -\frac{\partial\sigma^2}{\partial\varphi_k} + \sum_j W(j)aC_j\xi_m^2 f_k^c(j) - \sum_j W(j)\ [\sum_n \varphi_n f_n^c(j)f_k^c(j)\ ] \quad . \tag{3.43}$$

Defining B_k^c and M_{nk}^c by

$$B_k^c = \sum_j W(j)aC_j\xi_m^2 f_k^c(j) \tag{3.44}$$

$$M_{nk}^c = \sum_j W(j)f_n^c(j)f_k^c(j) \quad , \tag{3.45}$$

and using the results of Equation (3.34-3.37), one obtains

$$0 = B_k - \sum_n M_{nk}\varphi_n + B_k^c - \sum_n M_{nk}^c\varphi_n \quad . \tag{3.46}$$

Combining terms yields

$$0 = B_k' - \sum_n M_{nk}'\varphi_n \quad , \tag{3.47}$$

and the solution is obtained in the manner outlined in Equations (3.38-3.39).

Additional constraints may be added to the fit by procedures similar to the addition of elastic constants. Extra constraints may be included in order to produce a fit consistent with the axially symmetric conditions listed in Table 1.2. Also, additional constraints are necessary for fitting beyond 4NN in order to remove linear dependencies in the equations so that one may solve for the AFC's. In order to obtain solutions for the AFC's there must be as many independent interplanar force constants as independent AFC's for a given n-th neighbor fit. The method of determining the number of independent interplanar force constants is described below.

In Chapter I we found that not all the AFC's were independent but were reduced by symmetry. Similarly, the number of independent interplanar force constants can be determined by examining the degeneracies in the dispersion curves which arise from crystal symmetry.

From Figure 2.7 one finds that there are seven degenerate branches at $\Gamma(000)$, involving seven different sets of interplanar force constants $\Phi(j)$. However, there are only three independent elastic constants which characterize these seven different modes as $\xi \to 0$. Therefore, there must be four conditions relating the interplanar force constants. At X(001) there are five branches and only two different frequencies. Therefore, there must be three more constraints relating the interplanar

force constants due to these degeneracies. Finally, one additional condition is imposed by setting all of the $\Phi_p(j)$ equal to zero for planes beyond those which are required to include the designated number of neighbors. Therefore, there are eight constraints in all which relate the interplanar force constants.

Examination of Table 3.1 reveals that there are fewer independent interplanar force constants than AFC's for fitting beyond four nearest neighbors. Appropriate additional constraints on the AFC's must then be included in the fit in order to remove linear dependencies which remain in the equations. The manner in which additional constraints are added into the fitting program used in the present analysis is discussed below. First, however, the use of Table 3.1 in determining the number of extra constraints necessary for a given n-th neighbor fit is illustrated.

For a 6NN fit there are 18 independent AFC's as listed in Table 3.1. Only those $\Phi_p(j)$'s involving 1NN-6NN AFC's are included in a 6NN fitting procedure. Therefore, there are 24 relevant interplanar force constants in the three symmetry directions which were measured for γ-Ce. However, there are 8 conditions relating the $\Phi_p(j)$'s as discussed above. Thus, there are only 16 independent interplanar force constants, and two additional constraints must be imposed on the AFC's in order to obtain solutions from a 6NN fit.

For an 8NN fit there are 26 independent AFC's. There are 29 interplanar force constants in the three symmetry directions, 21 of which

are independent. Therefore, five additional constraints on the AFC's are required for fitting to 8NN.

If the [0ξ1] branches were included in an 8NN fit, eight more interplanar force constants would be added to the fit. (Note in Table 3.1, Φ_1 (Λ [0ξ1]) and Φ_3(Λ [0ξ1]) are zero out to eight neighbors.) However, the degeneracies associated with the [0ξ1] frequencies require fifteen conditions on the total set of 37 interplanar force constants. (See examples of fcc dispersion curves with [0ξ1] branches included in Reference 35.) Therefore, there are 22 independent interplanar force constants for an 8NN fit in which [0ξ1] data are included. To solve for the 26 independent AFC's, four extra conditions must be added to the fit.

The program used in the present analysis provided for the addition of two different types of extra constraints in the fitting procedure. Designated AFC's may be set equal to appropriate constant values, or axially symmetric constraints involving the relevant AFC's may be imposed. In each case the constraints must involve the appropriate AFC's in order to remove the linear dependencies remaining in the equations. (For the present analysis appropriate constraint combinations were determined by experimenting with the computer program rather than attempting to analyze a set of 26 equations.)

Both of the above types of constraints are added to the fitting procedure in a manner analogous to the addition of elastic constants. Equating a given AFC to a designated value, h, may be expressed by

$$0 = h - \sum_n \delta_n \varphi_n \quad , \tag{3.48}$$

where

$\delta_n = 1$ for the φ_n whose value is h;

$\delta_n = 0$ for all other φ_n.

Including a set of designated AFC's fixed at given values in Equation (3.29) requires an extra term given by

$$\sum_m W'_m (h_m - \sum_n \delta_n \varphi_n)^2 \quad . \tag{3.49}$$

Here W'_m is the weight with which each particular fixed value is added to the fit. The minimization procedure designated by Equation (3.34) now includes the extra terms given below,

$$\sum_m W'_m h_m \delta_k - \sum_m W'_m \sum_n \delta_n \varphi_n \delta_k \quad . \tag{3.50}$$

This expression can be simplified by defining

$$B'_k = \sum_m W'_m h_m \delta_k \tag{3.51}$$

$$M'_{nk} = \sum_m W'_m \delta_n \delta_k \quad . \tag{3.52}$$

Therefore, the extra constraint terms can be expressed by

$$B'_k - \sum_n M'_{nk} \varphi_n \quad . \tag{3.53}$$

These terms become elements of the appropriate arrays given below when minimization is carried out with respect to each φ_k.

$$\vec{B}' - \underline{\underline{M'_{nk}}} \vec{\varphi} \tag{3.54}$$

The above arrays may be combined with $\vec{B}$ and $\underline{\underline{M}}$, as given in Equation (3.38), and the solution obtained by matrix inversion.

Axially symmetric constraints may be included in a similar manner. Each axially symmetric condition (Table 1.2) may be written as

$$\sum_n \delta_{nm}\varphi_n = 0 \quad , \tag{3.55}$$

where δ_{nm} is the appropriate coefficient for each φ_n of a given equation, m. For example, to express the constraint on the first nearest neighbors;

$$\begin{aligned} &\delta_{(1XX),1} = 1 \quad ; \\ &\delta_{(1ZZ),1} = \delta_{(1YY),1} = -1 \quad ; \\ &\delta_{n,1} = 0 \quad \text{for all other } \varphi_n \quad . \end{aligned} \tag{3.56}$$

A set of axially symmetric constraint equations may be added to the fit by including the following term in Equation (3.29),

$$\sum_m W''_m \left(\sum_n \delta_{nm}\varphi_n\right)^2 \quad , \tag{3.57}$$

where W''_m is the weight with which the constraint equation, m, is added to the fit. Proceeding with the minimization yields

$$-\sum_m W''_m \sum_n \delta_{nm}\varphi_n\delta_{km} \quad . \tag{3.58}$$

(The minus sign arises from the change in sign invoked in Equation (3.34).) Using our standard type of definition,

$$M''_{nk} = \sum_m W''_m\delta_{nm}\delta_{km} \quad , \tag{3.59}$$

the additional constraint term becomes,

$$- \sum_n M''_{nk} \varphi_n \quad . \tag{3.60}$$

Upon minimization with respect to each φ_n a two-dimensional array $\underline{\underline{M}}''_{nk}$ results and may be added to $\underline{\underline{M}}_{nk}$ of Equation (3.38) in order to obtain solutions.

The weights with which the extra constraints (and elastic constants) are added to the fit are arbitrary. The degree to which a given constraint is obeyed is determined by the relative importance of the "constraint term" and the "phonon data term" in σ'^2. The magnitude of these terms is governed by the number of data points, the number of constraints, and the weights associated with each term.

Another option available in the program is fitting with an axially symmetric model. If all of the axially symmetric constraints on 1 to n neighbors are imposed for an n-th neighbor fit, the AFC's are constrained to obey the axially symmetric model. This procedure is not to be confused with the addition of several axially symmetric constraints merely as additional conditions which are necessary to remove linear dependencies and thereby obtain solutions. The terminology used to denote these various fitting procedures in the context of the present work is defined below.

An n-th neighbor fitting for $n \leq 4$ requires no additional constraints and is hereafter designated as a general tensor fit. For $n > 4$ additional constraints are necessary and these fitting procedures are called modified tensor fits. If any n-th neighbor fit is constrained

to obey all of the axially symmetric conditions on 1 to n neighbors it is called an axially symmetric fit.

The AFC's generated by the fitting procedure are used to evaluate the dynamical matrix for the measured ξ values of each mode (see Equation (3.11)). The program then calculates a frequency for each of the measured phonons in accordance with the phenomenological dynamical matrix that has been produced. The deviation of the calculated values from the measured values is given by the parameter, χ^2, defined as

$$\chi^2 = \frac{1}{N} \sum_{i=1}^{n} \left(\frac{\nu(i)_{calc} - \nu(i)_{exp}}{\Delta\nu(i)_{exp}} \right)^2 \tag{3.61}$$

The sum is over all data points, and N is given by

$$N = n - m \tag{3.62}$$

where n is the total number of data points and m is the number of fitting parameters.

Various fitting schemes which were utilized in the present analysis are listed below.

1) 4NN; general tensor.
2) 4NN; axially symmetric.
3) 6NN; modified tensor fit - two axially symmetric constraints on the fifth neighbors.
4) 6NN; modified tensor fit - two AFC's fixed at values given by the 4NN general tensor fit.
5) 6NN; axially symmetric.

6) 8NN; modified tensor fit - two axially symmetric conditions on the fifth neighbors, three axially symmetric conditions on the seventh neighbors.

7) 8NN; modified tensor fit - five AFC's fixed at values given by a 6NN fit.

8) 8NN; axially symmetric.

The variation of χ^2 for these fitting procedures is shown graphically in Figure 3.2. (The axially symmetric fits were run twice, first with weights of 100, then with weights of 1000 on all the axially symmetric constraints. Therefore, χ^2 is presented for both of these differently weighted procedures.) The axially symmetric fits usually have a slightly higher value of χ^2 for a given n-th neighbor fit, however, the differences in χ^2 between the axially symmetric fits and general or modified tensor fits is quite small. The most striking feature of Figure 3.2 is the large improvement in fit up to three nearest neighbors followed by a much more gradual reduction in χ^2 with the inclusion of more neighbors. This indicates that the most important interatomic forces in γ-Ce are fairly short range. However, residual long range interactions are also present which depend on the detailed electronic response to the nuclear motions. Therefore, the fit continues to improve out to eight neighbors.

The 8NN modified tensor fit, which was the best fit obtained, is shown in Figure 3.3. This fit was produced by all 8NN modified tensor fitting procedures, independent of the specific extra

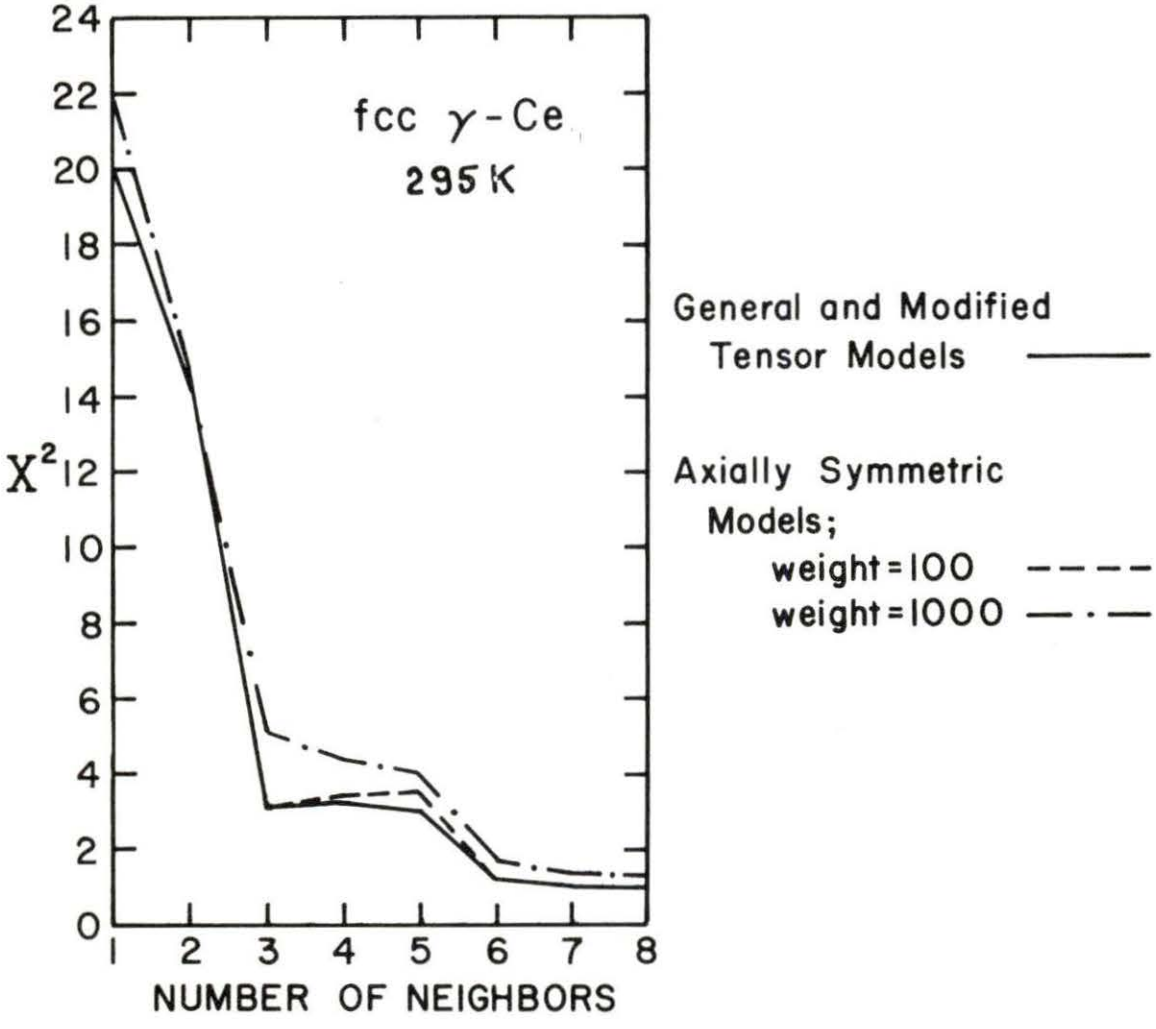

Figure 3.2. Variation of χ^2 with the number of neighbors included in the fit for axially symmetric, general tensor, and modified tensor fitting procedures

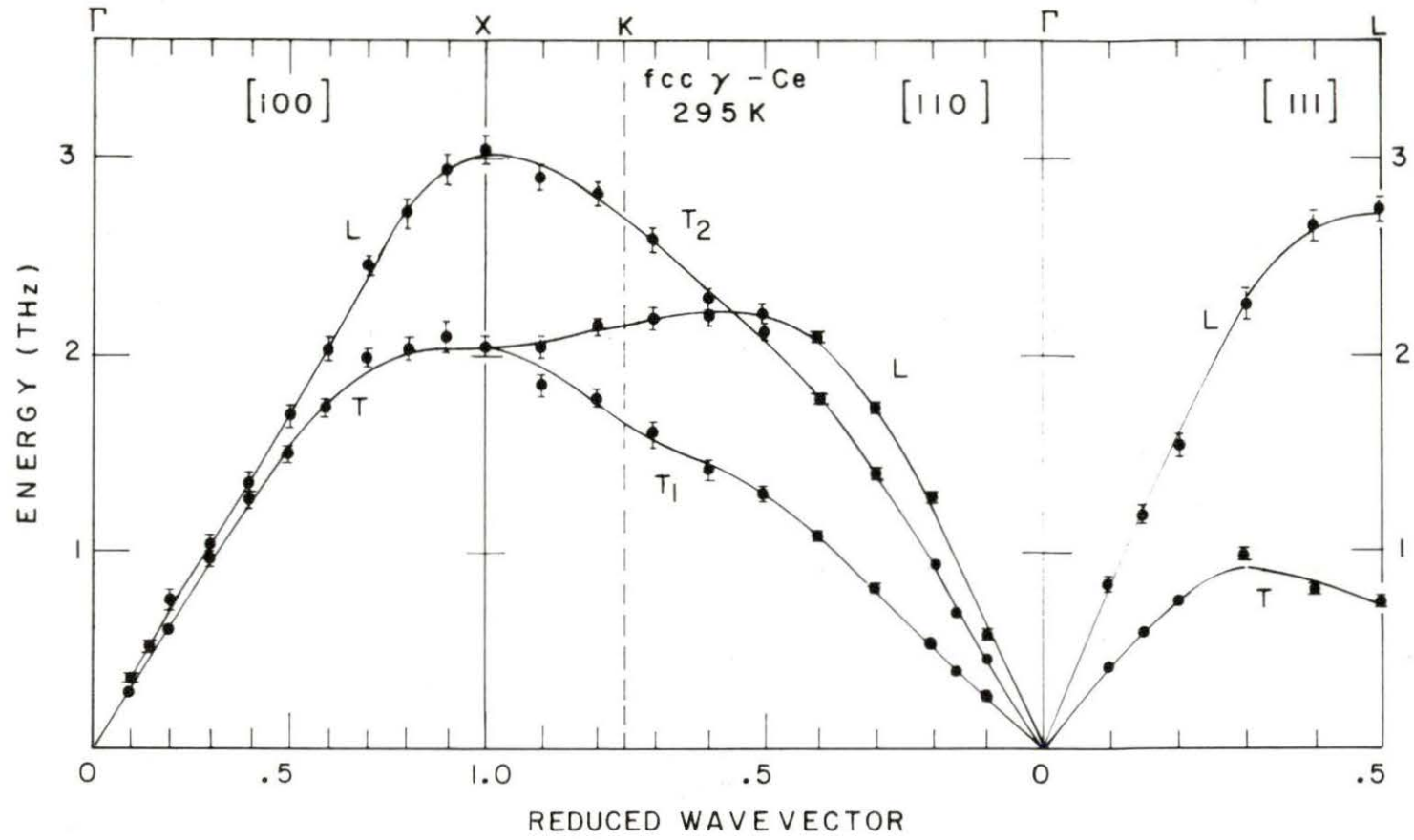

Figure 3.3. Dispersion curves for γ-Ce calculated from the 8NN modified tensor fitting procedures. The experimental data points and error bars are also given for comparison

constraints that were introduced. Table 3.3 lists four different combinations of constraints which were imposed in order to produce 8NN fits. Although all of these fitting procedures produced identical fits, and generated the same elastic constant values, the AFC's which were generated were slightly different.

The AFC's and elastic constants produced by the 8NN fit #1 (as designated in Table 3.3) are presented in Table 3.4. Throughout the remainder of the analysis, the results which are discussed in detail are those obtained from the AFC's listed in Table 3.4. The AFC's and elastic constants obtained from other fitting schemes are tabulated in Appendix C.

Since the AFC's are used in the calculation of the density of states, the above variation in their values among the 8NN fitting procedures produces some changes in the density of states. The variation in the density of states, however, has no noticeable effect on the thermodynamic properties which are calculated from it. There is also evidence that the density of states would be more uniquely defined if data from the [0ξ1] directions were included in the fit. This point will be examined further in the discussion of the density of states which follows.

Density of States

The method of calculating the density of states from the AFC's is described in detail elsewhere (42) and will be reviewed only briefly below. The AFC's generated by the fitting program give the value of

Table 3.3. Constraint combinations used for 8NN fitting procedures

Fitting Procedure	Constraints
	Axially Symmetric
8NN Fit #1	3(5XX) - 3(5YY) - 8(5XY) = 0
	(5XX) - 9(5YY) + 8(5ZZ) = 0
	2(7YY) - 2(7ZZ) - (7XY) = 0
	3(7YZ) - (7XY) = 0
	2(7XZ) - (7XY) = 0
8NN Fit #2	3(5XX) - 3(5YY) - 8(5XY) = 0
	(5XX) - 9(5YY) + 8(5ZZ) = 0
	3(7XX) - 3(7ZZ) - 4(7XY) = 0
	3(7YZ) - (7XY) = 0
	2(7XZ) - (7XY) = 0
	AFC Values Fixed
8NN Fit #3	1XX, 1XY, 2YY, 3YZ, 3XZ
8NN Fit #4	1XY, 2YY, 3XX, 3YZ, 3XZ

Table 3.4. AFC's and elastic constants obtained from 8NN fit #1

AFC	Value	(Error)	10^4 dynes/cm
1XX	0.47237	(0.04239)	
1ZZ	-0.08721	(0.07570)	
1XY	0.44955	(0.02800)	
2XX	-0.31061	(0.05936)	
2YY	0.02849	(0.02731)	
3XX	0.04096	(0.04448)	
3YY	0.02046	(0.02509)	
3YZ	-0.04848	(0.02004)	
3XZ	0.00663	(0.00728)	
4XX	-0.01327	(0.01451)	
4ZZ	0.03369	(0.03180)	
4XY	0.02206	(0.03668)	
5XX	0.00434	(0.02172)	
5YY	0.00002	(0.01191)	
5ZZ	-0.00052	(0.01556)	
5XY	0.00162	(0.01213)	
6XX	-0.02288	(0.00801)	
6YZ	0.00989	(0.02331)	
7XX	0.00695	(0.01070)	
7YY	-0.00866	(0.01011)	
7ZZ	-0.00517	(0.00405)	
7YZ	-0.00233	(0.00617)	
7XZ	-0.00349	(0.00925)	
7XY	-0.00698	(0.00225)	
8XX	0.00045	(0.00022)	
8YY	0.01145	(0.00933)	

Elastic Constants	Value 10^{12} dynes/cm^2
c_{11}	0.23888
c_{44}	0.18605
c_{12}	0.08890
$(c_{11} - c_{12} + c_{44})/3$	0.11201
$(c_{11} + 2c_{12} + 4c_{44})/3$	0.38695
$(c_{11} - c_{12})/2$	0.07499
$(c_{11} + c_{12} + c_{44})/2$	0.34993

the dynamical matrix at any point $\vec{q}$ in the first Brillioun zone. The density of states program uses the dynamical matrix to solve for eigenfrequencies corresponding to $\vec{q}$ values that form a cubic mesh in momentum space. Consider an eigenfrequency, $\nu_0(\vec{q})$, and a slightly different frequency, $\nu_0(\vec{q}) + \Delta\nu$, both of which lie on constant frequency surfaces. The number of frequencies between $\nu_0(\vec{q})$ and $\nu_0(\vec{q}) + \Delta\nu$ is proportional to the volume confined between the two constant frequency surfaces. By calculating the appropriate volumes, the density of states is obtained.

By examining the general mathematical form for the density of states, one obtains insight into the relationship between features of the density of states and features of the dispersion curves. The density of states may be written as (43),

$$g(\omega)d\omega = \left(\frac{L}{2\pi}\right)^3 \int \frac{dS_\omega}{v_g} d\omega \quad . \tag{3.63}$$

Here $\left(\frac{L}{2\pi}\right)^3$ is the volume of the sample, dS_ω is an area element in momentum space, and v_g is the group velocity of the lattice vibrations. Since v_g represents the slope of the dispersion curves, one expects a very large density of states where $v_g \to 0$. In comparing dispersion curves and density of state curves one must bear in mind that the dispersion curves represent phonons in only a few symmetry directions while the structure of the density of states is governed by off-symmetry modes as well. However, in general the flat areas of the dispersion curves can be related to structures in the density of states.

The density of states for γ-Ce corresponding to the AFC's from the 8NN fit #1 is shown in Figure 3.4. Comparison to the dispersion curves (Figure 3.3) identifies the peak at 2.2 THz with the flattened portions of the L [110], T [001] and T_1 [110] branches near the zone boundary. The peak at 2.6 THz corresponds to the flattening of the L [111] branch near the zone boundary. There is no feature in the dispersion curves, however, which corresponds to the large peak at 1.43 THz in the density of states.

If AFC's from other 8NN fits are used in the density of states program, the position of the unidentified peak changes dramatically. The other peaks change somewhat in structure and position for different AFC's, however, these variations are minor. On the other hand, the center of the unidentified peak varies over a range of 1.38-1.74 THz for different sets of AFC's produced by various 8NN modified tensor fitting schemes. (The various density of states are presented in Appendix C.)

In consulting the density of states and dispersion curves for other fcc metals, it was discovered that the Λ [0ξ1] branch is usually very flat (35,44). Therefore, the AFC's from a 6NN fit were used to calculate frequencies for the [0ξ1] branches which were consistent with the fit obtained to the measured data. The calculated [0ξ1] branches are shown in Figure 3.5. For the Λ branch the slope goes to zero at a frequency of 1.65 THz. The corresponding 6NN density of states given for comparison in Figure 3.6 locates the unidentified peak at 1.65 THz.

According to the above analysis, the "mobile" peak in the density of states apparently arises primarily from [0ξ1] phonons. The variation of AFC's with imposed fitting constraints and the subsequent variation

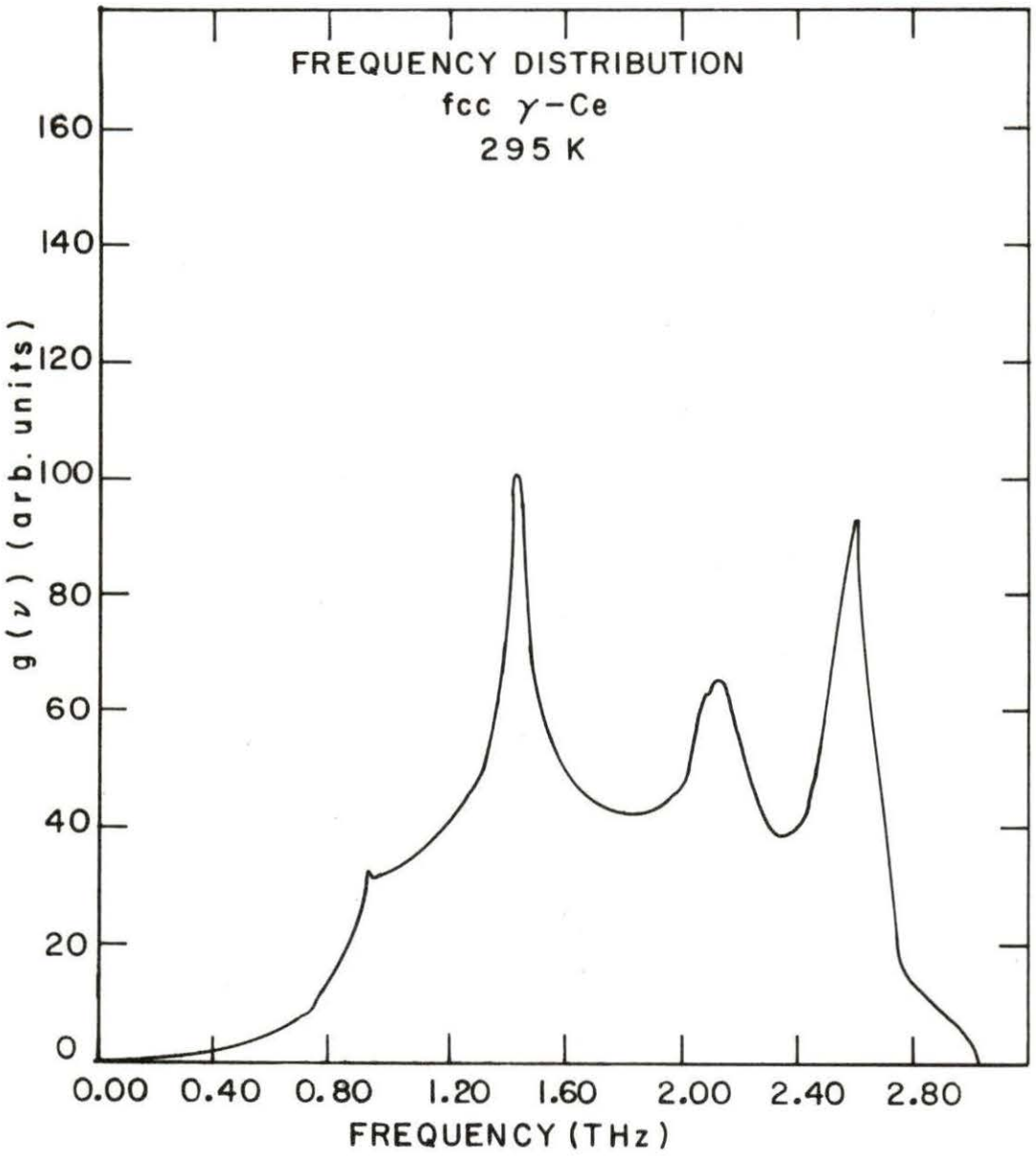

Figure 3.4. Density of states for γ-Ce calculated from the AFC's generated by 8NN Fit #1

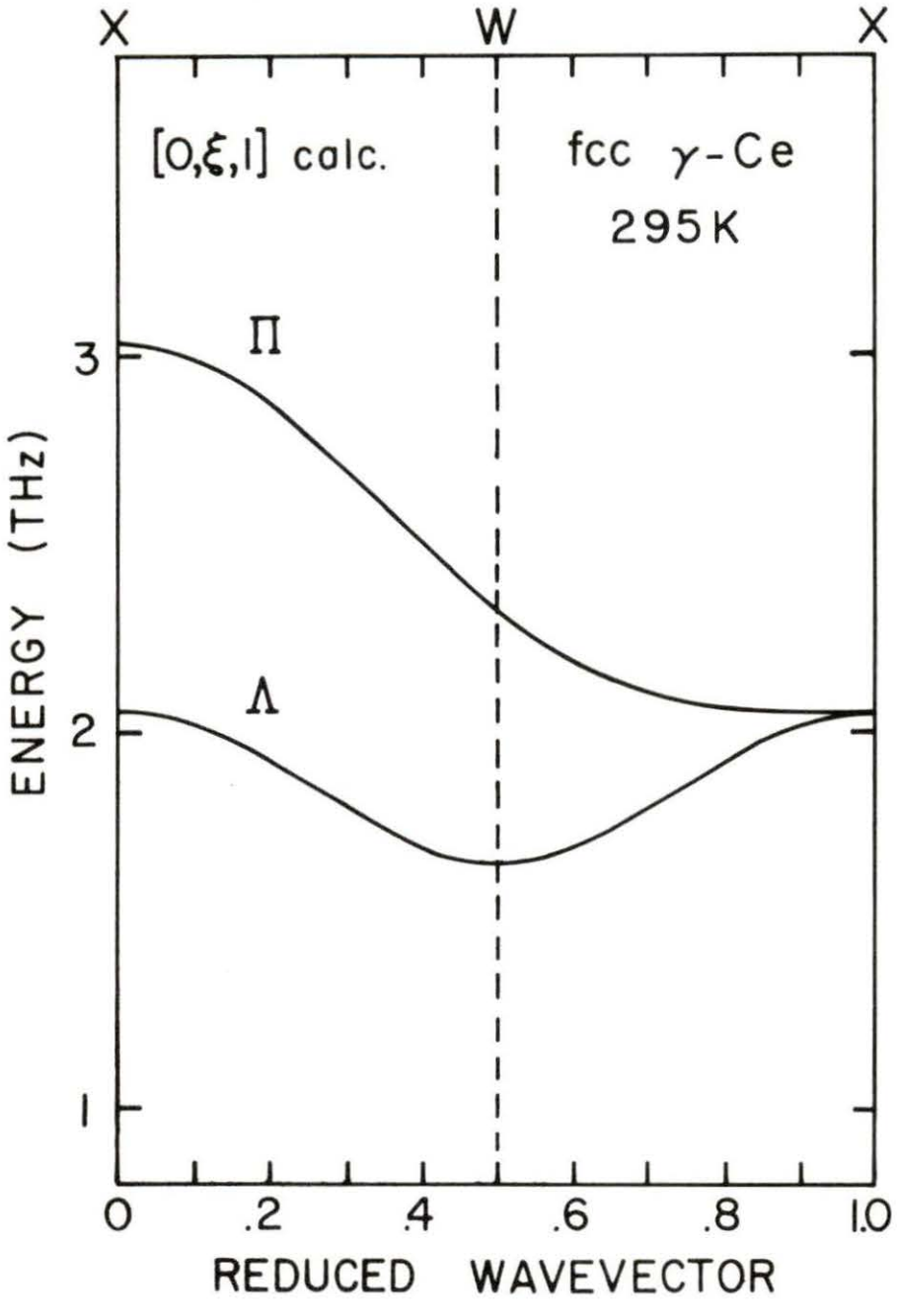

Figure 3.5. γ-Ce [0ξ1] branches calculated from the AFC's produced by 6NN Fit #1 (see Appendix C for the constraints on this fitting procedure)

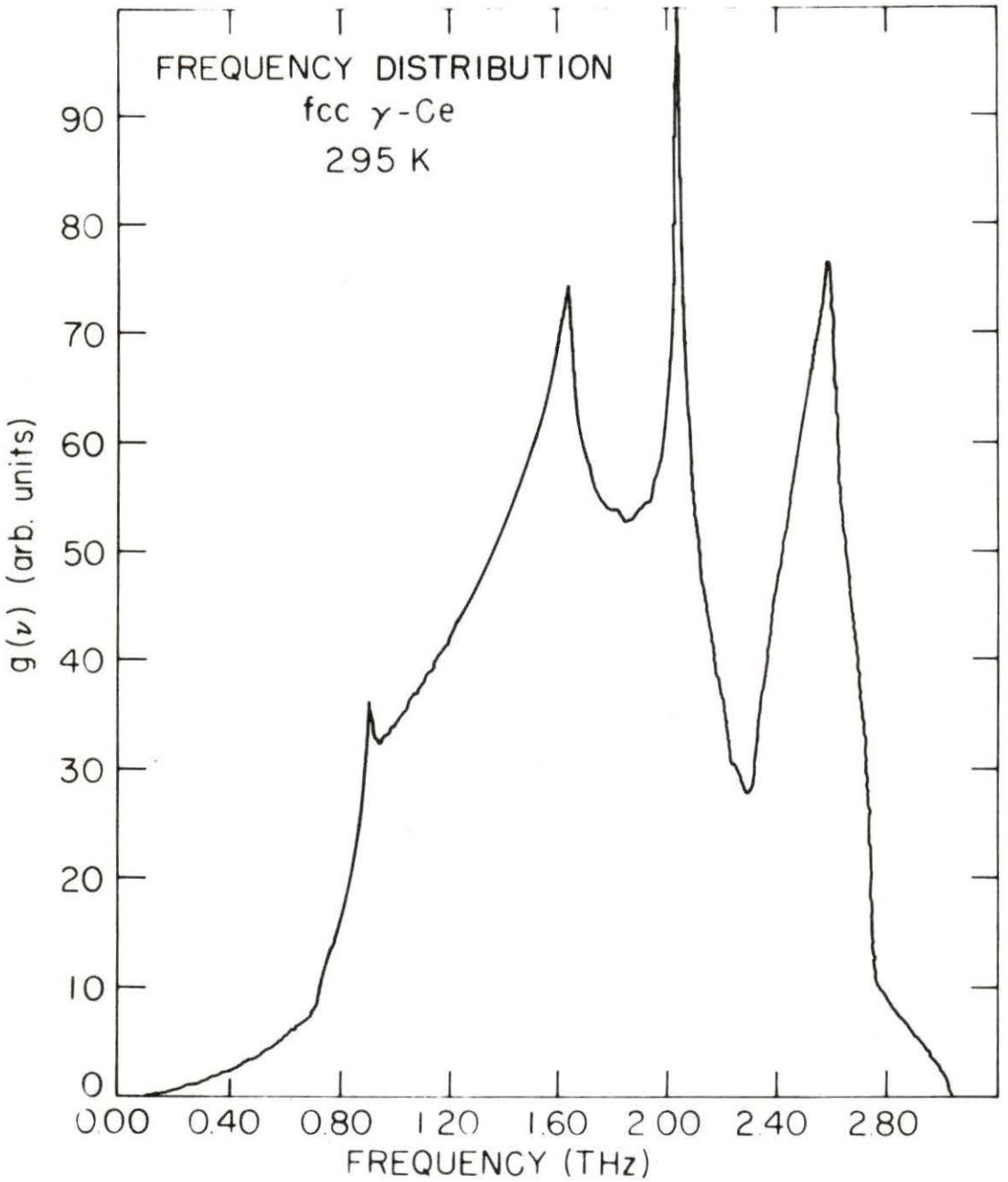

Figure 3.6. Density of states calculated from the AFC's generated by 6NN Fit #1. Note the correspondence between the peak at 1.65 THz and the Λ [0ξ1] branch shown in Figure 3.5

in the density of states would probably be appreciably diminished by including real [0ξ1] data in the fitting procedure. Plans are now underway for the measurements of the [0ξ1] branches of γ-Ce in collaboration with Dr. R. M. Nicklow of Oak Ridge National Laboratory.

The variation in the position of the [0ξ1] peak induced by various fitting procedures has no noticeable effect on the lattice specific heat or Debye temperature which are calculated from the density of states. The results of the present analysis of the thermodynamic properties of γ-Ce are presented below and the comparison of these results to former thermodynamic measurements on γ-Ce is presented in a later section.

Thermodynamic Properties

Before presenting the specific thermodynamic results obtained for γ-Ce it is useful to examine the method by which these properties are calculated. The internal energy function for lattice vibrations is given by (43)

$$U = \int_0^\infty d\omega g(\omega) n(\omega) \hbar\omega \tag{3.64}$$

where $n(\omega)$ is the phonon occupation number as defined in Chapter I, $g(\omega)$ is the phonon density of states, and the integration is performed over all frequencies, ω. The lattice specific heat at constant volume is given by the derivative of the above expression.

$$C_V^{\ell} = \left(\frac{\partial U}{\partial T} \right)_V = \frac{\hbar^2}{kT^2} \int_0^\infty \frac{d\omega g(\omega) \omega^2 e^{\hbar\omega/kT}}{(e^{\hbar\omega/kT} - 1)^2} \tag{3.65}$$

Equation (3.65) can be integrated numerically for any temperature, $T > 0$, given the phonon density of states $g(\omega)$. Therefore, using the output from the density of states program, $C_V^{\ell}(T)$ for γ-Ce was generated. Figure 3.7 gives the lattice specific heat curve generated from the "8NN fit #1" density of states. No appreciable change was induced by using any of the slightly different 8NN densities of states.

At room temperatures the value of C_V^{ℓ} approaches the classical Dulong-Petit value of 3R where R is the universal gas constant. For very low temperatures, the lattice specific heat varies as T^3 over a small region as predicted by the Debye model (43).

It is customary to express lattice specific heat information in terms of the temperature variation of the Debye temperature, θ_D. The method by which $\theta_D(T)$ is obtained is given below.

In the context of the Debye model, the phonon density of states is given by $A\omega^2$, where A is a constant. Since the Debye model is a continuum approximation which treats a solid as a non-dispersive medium, one would expect $g(\omega) \approx A\omega^2$ only for very low frequencies (long wavelengths). At $T \gtrsim 0$ the population factor in Equation (3.65) may be assumed to be essentially equal to one for a few low frequencies, and equal to zero for all other frequencies. Therefore, at $T \gtrsim 0$ the expressions for the Debye specific heat and the real specific heat may be equated.

$$\int_{\omega_1}^{\omega_2} A\omega^4 d\omega = \int_{\omega_1}^{\omega_2} g(\omega)\omega^2 d\omega \qquad (3.66)$$

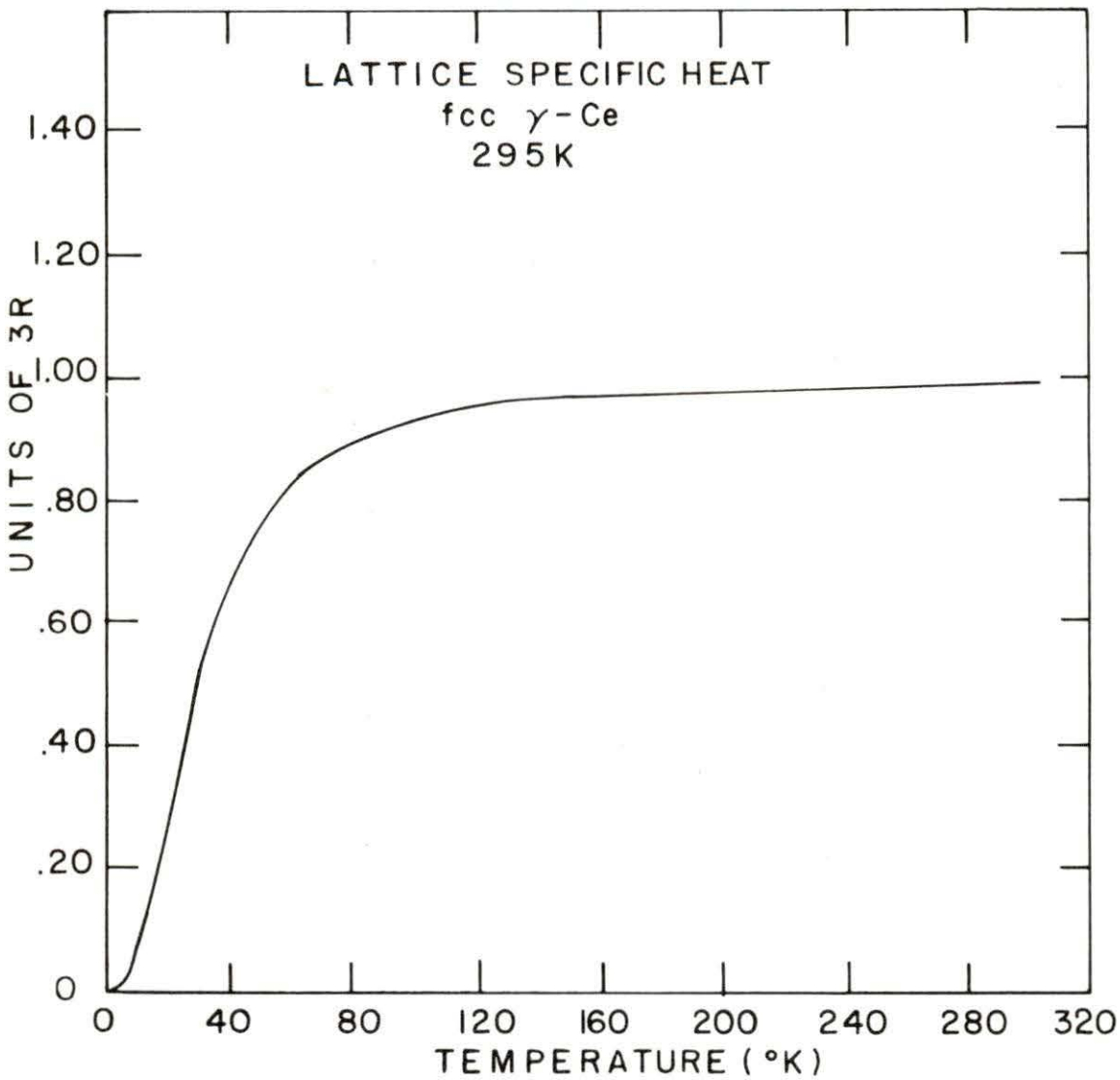

Figure 3.7. Temperature dependence of the lattice specific heat of γ-Ce. The specific heat curve was generated from the density of states shown in Figure 3.4

Thus the constant, A, may also be calculated from the density of states by numerical integration.

$$A = \frac{\int_{\omega_1}^{\omega_2} g(\omega)\omega^2 d\omega}{\int_{\omega_1}^{\omega_2} \omega^4 d\omega} \tag{3.67}$$

Obtaining a value for A allows one to calculate the Debye temperature, θ_D. If $g(\omega)$ is normalized such that

$$\int_0^{\infty} g(\omega)d\omega = 1 \quad , \tag{3.68}$$

then

$$\int_0^{\omega_D} A\omega^2 d\omega = 1 \tag{3.69}$$

since the total number of states in the Debye model must equal the real number of phonon states. (Notice that the upper limit of the integral over the Debye density of states must be a finite value, ω_D, in order to obtain a finite number of states.) The Debye temperature is defined by

$$\frac{\hbar\omega_D}{kT} = \frac{\theta_D^0}{T} \tag{3.70}$$

Therefore, one obtains from Equations (3.69) and (3.70),

$$1 = \frac{A\omega_D^3}{3} = \frac{A\theta_D^3}{3}\left(\frac{k}{\hbar}\right)^3$$

$$\theta_D^0 = \left(\frac{\hbar}{k}\right)[3/A]^{1/3} \quad . \tag{3.71}$$

The value of A calculated from Equation (3.67) is obtained in the approximation that $T \approx 0$. Therefore, incorporating this value of A into Equation (3.71) yields the Debye temperature at zero degrees, θ_D^0.

If the Debye approximation was valid at all temperatures, the Debye temperature would be a constant equal to θ_D^0. However, the Debye specific heat varies significantly from the real lattice specific heat as the temperaure is increased and higher frequency modes are thermally excited. The Debye model can be "forced" to yield the correct specified heat value at any given temperature, however, by allowing the value of θ_D to vary. The value of θ_D is adjusted by successive iterations until the specific heat given by the Debye model is equal to the specific heat generated by the real density of states for a given temperature, T. This procedure yields the temperature variation of the Debye temperature, $\theta_D(T)$ which gives a measure of the deviation of the real lattice specific heat from the Debye model.

The Debye temperature for γ-Ce is given in Figure 3.8. Near room temperature θ_D becomes temperature independent as the specific heat becomes model independent and approaches the classical value of 3R.

Specific heat and Debye temperature values for γ-Ce obtained from former experiments are compared with the above results in the following section. Features of the dispersion curves and calculated elastic properties are also discussed.

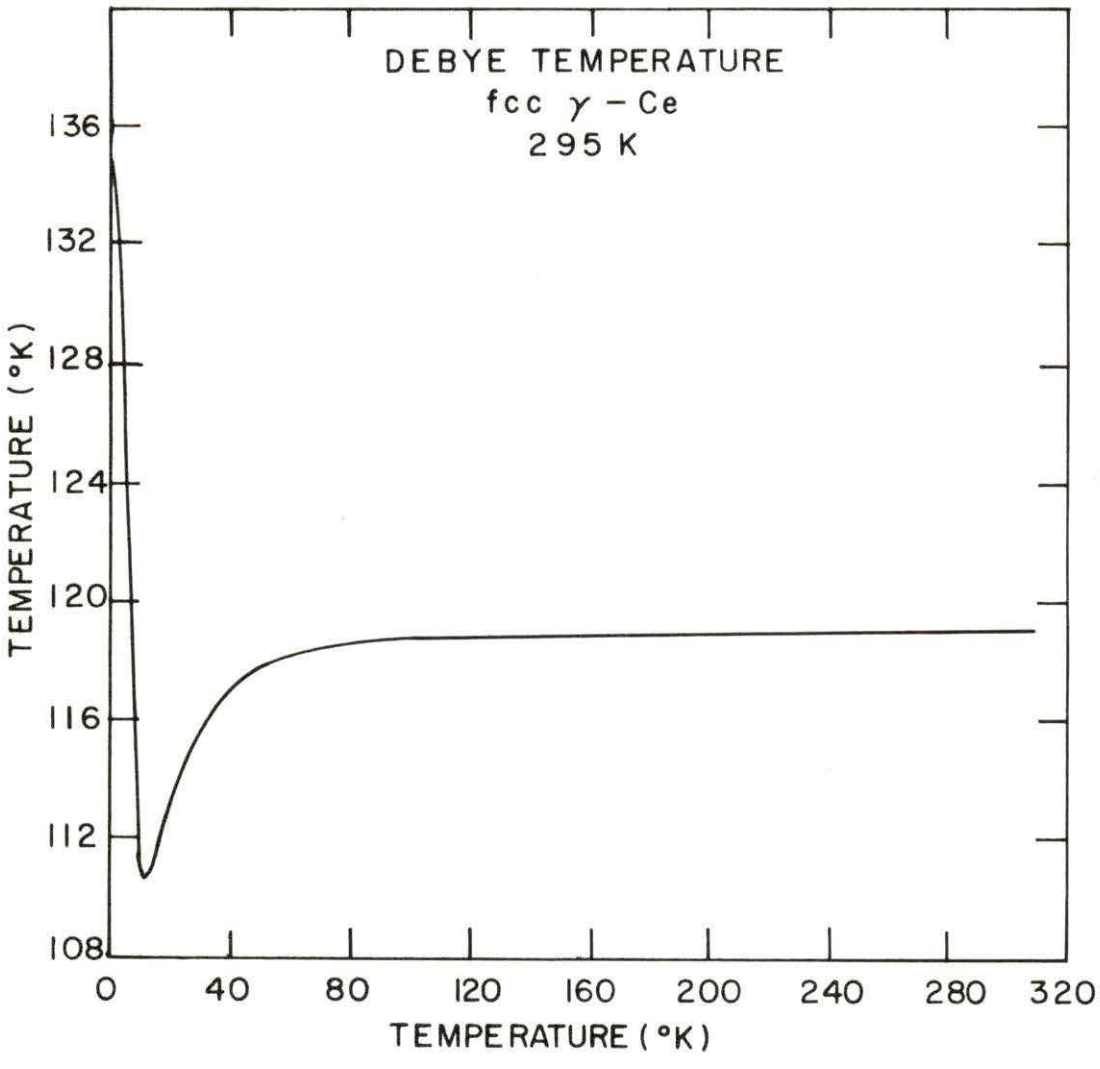

Figure 3.8. Temperature dependence of the Debye temperature for γ-Ce calculated from the density of states given in Figure 3.4

Lattice Dynamical Results - Comparisons

The present experiment was performed on one of the first single crystals of γ-Ce successfully produced by Ames Laboratory. Therefore, the current results represent the first single crystal lattice dynamical measurements to be performed on γ-Ce.[1] Unfortunately, no data on single crystals are available for comparison of the calculated elastic and thermodynamic properties. The various calculated values must therefore be compared with the results of former measurements which were performed on polycrystalline samples. Before, the comparison of these properties is discussed, however, the dispersion curves of γ-Ce are compared with the dispersion curves of other fcc metals.

One of the primary motivations for measuring the dispersion curves of γ-Ce was to obtain insight into the α-γ transition and the possible mixed valence nature of γ-Ce. However, there exists no well-developed theoretical description of these phenomena. Therefore, the unique features of the γ-Ce dispersion curves are discussed only qualitatively below. The relationship of these features to the other intriguing properties of γ-Ce is yet to be determined.

The lattice vibrational spectrum of a crystalline element is generally expected to be similar to that of other elements having the same

---

[1] The measurement of the magnetic form factor of γ-Ce by polarized neutron scattering discussed in Chapter I (20) was also performed on a single crystal of γ-Ce produced by Ames Laboratory. The comparison of these results to the magnetic scattering observed in the present experiment is presented in the section on Magnetic Scattering Analysis which follows the current discussion.

crystal structure which lie in the same column of the periodic table. These elements have analogous electronic structures, which suggests that the interatomic forces may be similar. If the atoms in a crystal behave like a system of classical "balls and springs", one can obtain a rough idea of the relationship between the phonon frequencies of two such elements by considering the expression for the frequency of a classical harmonic oscillator.

$$\omega = \sqrt{\frac{k}{m}} \tag{3.72}$$

Here m is the mass and k is the spring constant. The difference in the atomic masses of the two elements will obviously affect the frequencies. The effective "spring constant" of a crystalline element is unknown, however, it must be related to the interatomic spacing over which the interatomic forces act. Therefore, the homology rule for phonon frequencies of similar crystalline elements is given by

$$\frac{\langle \nu_1 \rangle}{\langle \nu_2 \rangle} = \left(\frac{M_2}{M_1} \frac{a_2^2}{a_1^2} \right)^{\frac{1}{2}} . \tag{3.73}$$

Here ν is the frequency, M is the mass, and a is the lattice parameter.

Another estimate of the ratio of frequencies to be expected for two similar crystalline elements is obtained from the Lindemann rule (44). This empirical equation relates the Debye temperature of an element to its melting temperature.

$$\theta_D = C \sqrt{\frac{T_M}{MV^{2/3}}} \tag{3.74}$$

Here T_M is the melting temperature, M is the mass, V is the volume, and C is a constant. This equation can be modified using the relationship between Debye temperature and frequency [Equation (3.70)] to yield another estimate of the frequency ratio for two similar crystalline elements.

$$\frac{\langle \nu_1 \rangle}{\langle \nu_2 \rangle} = \left(\frac{M_2 \, T_{M1} \, a_2^2}{M_1 \, T_{M2} \, a_1^2} \right)^{\frac{1}{2}} \tag{3.75}$$

The electronic structure of cerium is more similar to that of thorium than any other element in the periodic table. Thorium is also an fcc metal and the dispersion curves have been measured (45). Therefore, a frequency comparison can be made.

Using the appropriate masses, and lattice parameters, the homology rule predicts

$$\langle \nu_{Ce} \rangle = 1.3 \langle \nu_{Th} \rangle \quad . \tag{3.76}$$

However, if the melting temperatures are included in the context of the Lindemann rule one obtains

$$\langle \nu_{Ce} \rangle = .95 \langle \nu_{Th} \rangle \quad . \tag{3.77}$$

Apparently the γ-Ce frequencies are governed by more complex interactions than the homology rule takes into account. These interactions are

reflected in the melting temperature, therefore, there is a large discrepancy between Equations (3.76) and (3.77).

A comparison of the measured frequencies of γ-Ce and thorium yields another interesting result. (The dispersion curves of thorium are given in Figure 3.9 for reference.) Comparing the zone boundary frequencies of γ-Ce (Figure 3.3) and of thorium, one finds that the γ-Ce frequencies are indeed lower as the Lindemann rule suggests. However, the actual numerical values are even lower than those predicted by the Lindemann equation. The γ-Ce frequencies lie 4-11% below the predicted Lindemann results for three of the four non-degenerate zone boundary frequencies. The T [111] zone boundary frequency is 43% lower than predicted.

A similar lowering of the phonon frequencies has also been observed for $CeSn_3$ which is currently being studied at Ames Laboratory. The correspondence between the behavior of the phonons in γ-Ce and $CeSn_3$ is of particular interest since $CeSn_3$ is a mixed valence compound.

A systematic lowering of phonon frequencies reflects interatomic "spring constants" that are weaker than expected, i.e., the lattice is "softer" than expected. Lattice "softening" in γ-Ce has also been observed in room temperature bulk elastic measurements performed as a function of pressure on a polycrystalline sample (46). As the pressure was increased toward the γ-α transition pressure, the compressibility steadily increased. At the transition itself the compressibility decreased dramatically. Similar behavior was observed in the measurement of elastic moduli as a function of temperature (47), however, here the results were complicated by the formation of the intermediate β-phase.

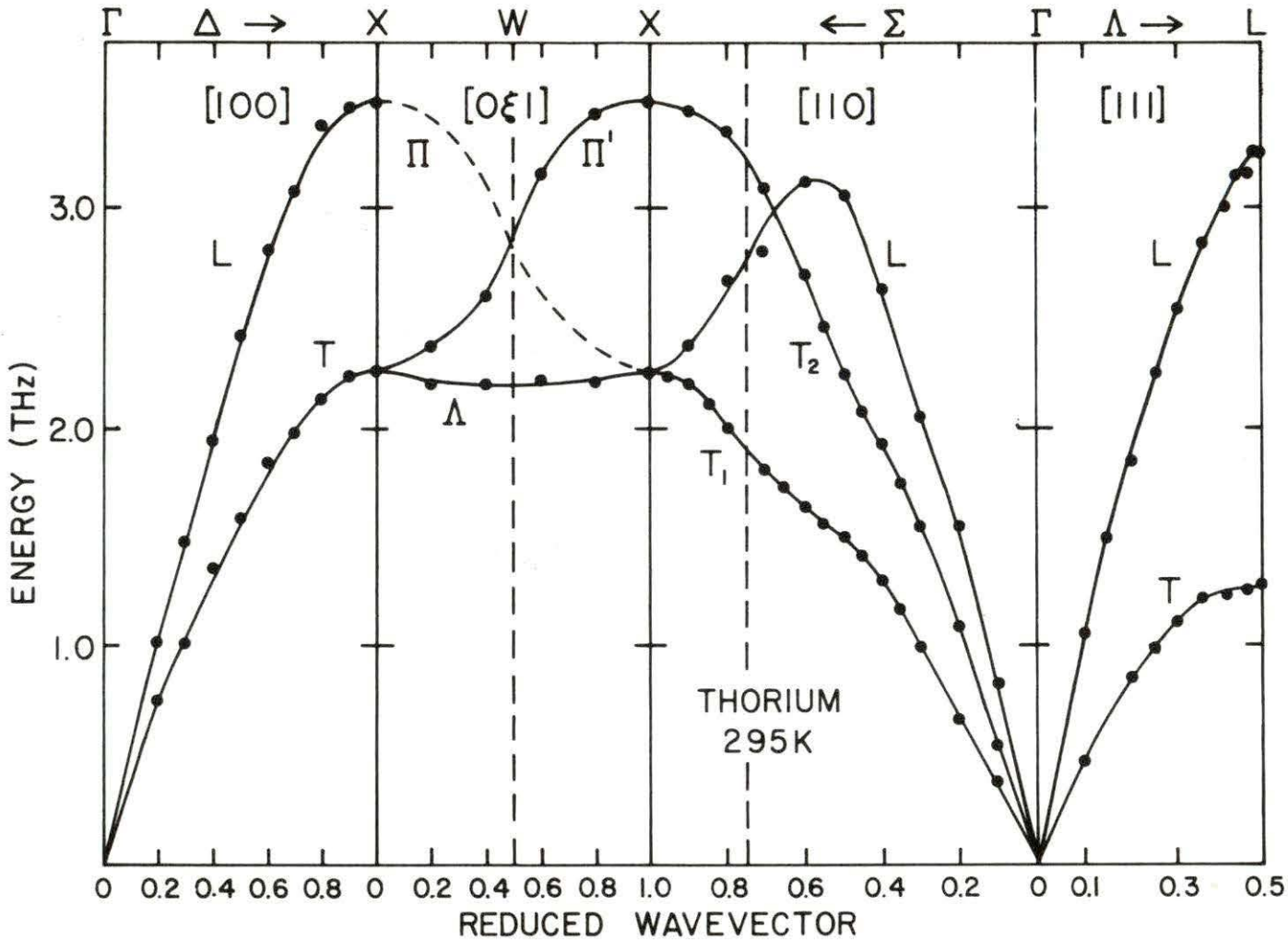

Figure 3.9. Phonon dispersion curves for thorium along the principle symmetry directions (45). The line is a hand-drawn smoothed curve

At this point it is tempting to correlate the α-γ transformation with the general softening of the phonons and elastic properties of γ-Ce, and with the striking frequency decrease of the T [111] zone boundary phonon. Any relationship among these phenomena is presently unknown, however, a temperature-dependent study of the T [111] zone boundary phonon may yield significant results with respect to these questions. An experiment of this type is now being planned in collaboration with Dr. R. M. Nicklow of Oak Ridge National Laboratory.

Another interesting feature of the γ-Ce dispersion curves is the flatness of the L [110] branch. The corresponding branch in the thorium curves exhibits a very sharp curvature. Most fcc metals have a larger curvature in the L [110] branch than γ-Ce, although many do not exhibit as sharp a curvature as does thorium (35,43,48). The implications of the peculiar flatness of the L [110] branch is γ-Ce are unknown, however, this behavior is consistent with an overall softening of the phonons.

In addition, it is interesting to notice that the L [001] and T [001] branches of γ-Ce lie very close together throughout a considerable portion of the first Brillioun zone. Therefore, the c_{11} and c_{44} elastic constants associated with these modes are very close in value (see Tables 3.2 and 3.4).

No single crystal elastic constant measurements have been performed on γ-Ce. Therefore, no data exist for a direct comparison with the elastic constant values generated by the fitting procedures of the present analysis. However, polycrystalline bulk elastic moduli for γ-Ce have been determined by several authors (46,47,49,50) Unfortunately, polycrystalline

elastic moduli cannot be accurately calculated from single crystal elastic constants via simple averaging techniques unless the crystal is nearly isotropic (51). However, a calculation of this type was utilized in the present analysis in order to determine whether the single crystal measurements were consistent with the results from former experiments on polycrystalline samples.

The averaging technique first proposed by Voigt (52) assumes the existence of uniform local stress throughout the polycrystalline sample. The relationships expressing the stress of a single crystal in terms of a given strain are averaged over all possible lattice orientations. On the other hand, the Reuss average (53) is performed assuming uniform local strain. Therefore, in the Reuss procedure the relationships expressing the strain in terms of a given stress are averaged over all possible lattice orientations. Both of these models are physically unrealistic. In the context of the Voigt average the forces between the individual grains cannot be in equilibrium, and according to the Reuss method the distorted grains cannot fit together. In order to approach the problem rigorously, one would need to solve the equations of equilibrium for every crystallite, taking into account the appropriate boundary conditions at their surfaces of separation (51). Therefore, the averaging techniques are approximations which yield fairly accurate results only for nearly isotropic crystals.

The Voigt and Reuss expressions for the bulk modulus ($B = 1/K_T$, where K_T is the isothermal compressibility) and shear modulus (μ) of a cubic crystal are given in Table 3.5a. In these equations the c_{ij} are

Table 3.5a. Voigt and Reuss expressions for the bulk modulus, B, and shear modulus, μ, of cubic crystals

Voigt Equations	Reuss Equations
$B = 1/3(c_{11} + 2c_{12})$	$B^{-1} = 3(s_{11} + 2s_{12})$
$\mu = 1/5(c_{11} - c_{12} + 3c_{44})$	$\mu^{-1} = 1/5(4s_{11} - 4s_{12} + 3s_{44})$

elastic constants and the s_{ij} are compliance moduli. The relationships between the elastic constants and compliance moduli for a cubic crystal are given in Table 3.5b. Since there are only two independent elastic

Table 3.5b. Relationship of compliance moduli and elastic constants for cubic crystals

$$s_{44} = \frac{1}{c_{44}}$$

$$s_{11} - s_{12} = \frac{1}{c_{11} - c_{12}}$$

$$s_{11} + 2s_{12} = \frac{1}{c_{11} + 2c_{12}}$$

moduli for polycrystalline materials (as discussed below) all of the elastic moduli of interest can be calculated from B and μ. Before the comparison of the calculated Voigt and Reuss values and the former results is presented, a brief description of the measurement of bulk elastic moduli is given below.

An ideal polycrystalline material is treated as an isotropic continuous medium. Therefore, polycrystalline materials are characterized by only two independent wave velocities, i.e., longitudinal and transverse with respect to the directon of propagation. Standard elastic moduli may be calculated from experimentally measured longitudinal and transverse wave velocities (v_ℓ, and v_t respectively) according to the expressions given below.

$$\text{Adiabatic compressibility:} \quad K_s = [\rho(v_\ell^2 - 4/3\ v_t^2]^{-1} \tag{3.78}$$

$$\text{Young's modulus:} \quad Y = \rho\ v_t^2\left[\frac{4 - 3(v_\ell/v_t)^2}{1 - (v_\ell/v_t)^2}\right] \tag{3.79}$$

$$\text{Shear modulus:} \quad \mu = \rho\ v_t^3 \tag{3.80}$$

$$\text{Poisson's ratio:} \quad \sigma = \frac{2 - (v_\ell/v_t)^2}{2[1 - (v_\ell/v_t)^2]} \tag{3.81}$$

In these equations the ρ denotes the density of the material.

Experimental values for these bulk elastic moduli of γ-Ce obtained from wave velocity measurements are given in Table 3.6. The values obtained from References 46 and 50 are probably the most reliable as the other experiments involved thermal cycling and undetermined amounts of β-Ce may have formed in the sample and influenced the results.

The calculated Reuss and Voigt values for polycrystalline elastic moduli given in Table 3.6 were obtained using the elastic constant values

Table 3.6. Comparison of measured and calculated elastic moduli values

	Adiabatic Compressibility 10^{-12} dynes/cm^2	Young's Modulus 10^{12} dynes/cm^2	Shear Modulus 10^{12} dynes/cm^2	Poisson's Ratio	Reference
	4.64	.337	.136	.240	49
Polycrystalline	4.64	.336	.135	.237	47
Measurements	5.05	.300	.120	.248	50
	5.05	.299	.120	.248	46
Present Work	7.18	.317	.142	.119	Voigt Average
	7.18	.274	.117	.172	Reuss Average

given by the 8NN fit #1. In order to calculate the adiabatic compressibility, the Reuss and Voigt values of the bulk modulus obtained according to the relationships given in Table 3.5a were inverted to yield the isothermal compressibility, K_T. The adiabatic compressibility was then calculated from the relation

$$K_s = K_T - \frac{TV9\alpha^2}{C_p} \quad . \tag{3.82}$$

Here T is the absolute temperature, V is the atomic volume (9), α is the linear coefficient of thermal expansion (54), and C_p is the specific heat at constant pressure (55). The values of these properties for γ-Ce used in the calculation of K_s were obtained from the indicated references. Young's modulus and Poisson's ratio were then obtained from the following relationships.

$$Y = 2\ (1 + \sigma) \tag{3.83}$$

$$K_s = 3(1 - 2\sigma)/Y \tag{3.84}$$

The agreement between the calculated and measured values listed in Table 3.6 is particularly good for Young's modulus and the shear modulus. The values for Poisson's ratio and the compressibility agree less well. However, within the context of the approximations employed in obtaining the averaged values, the calculated moduli are indeed consistent with the values obtained from polycrystalline experiments.

Polycrystalline wave velocity measurements can also be used to calculate θ_D. From Debye theory one obtains (56)

$$\nu_D = \left(\frac{3N_a \rho}{4\pi(MW)} \right)^{1/3} \bar{v} \quad , \tag{3.85}$$

where ν_D is the Debye cut-off frequency, N_a is Avogadro's number, ρ is the density, (MW) is the molecular weight, and $\bar{v}$ is the average sound velocity. For a polycrystalline sample which is assumed to be elastically isotropic (small grain size with respect to acoustic wavelength) the average sound velocity is given by

$$\bar{v} = [1/3(2/v_t^3 + 1/v_\ell^3)]^{-1/3} \quad . \tag{3.86}$$

Therefore, incorporating the definition of the Debye temperature [Equation (3.70)] into Equation (3.86) yields

$$\theta_D = \frac{h}{k}\left(\frac{3N_a \rho}{4\pi(MW)} \right)^{1/3} \left[\frac{1}{3}\left(\frac{2}{v_t^3} + \frac{1}{v_\ell^3} \right) \right]^{-1/3} \quad . \tag{3.87}$$

There is no explicit temperature dependence given in the above expression for θ_D, however, v_t and v_ℓ are functions of temperature. Thus, for wave velocity measurements performed at a given temperature, T_1, the Debye temperature given by Equation (3.87) is equal to $\theta_D(T)$ evaluated at T_1.

The above temperature dependent θ_D value, however, is not derived under precisely the same assumptions as $\theta_D(T)$ generated by a lattice dynamical analysis. In a lattice dynamical analysis the Debye parameter at a given temperature, T_1, is adjusted until the specific heat calculated from the Debye model density of states becomes equal to the

specific heat calculated from the experimental phonon density of states. The Debye temperature obtained from wave velocity measurements, however, is calculated from a Debye model expression [Equation (3.87)] at all temperatures, without the benefit of adjustment to yield "correct" results. Thus the value of the Debye temperature (for a given temperature, T_1) calculated from the present lattice dynamical analysis cannot be expected to agree precisely with the corresponding Debye temperature calculated from wave velocity measurements.

A comparison of room temperature θ_D values is given in Table 3.7. The values listed for the present analysis were calculated from the density of states produced by 8NN fit #1. Again, the polycrystalline values given by References 46 and 50 are probably the most reliable, as those given by References 47 and 49 may have been influenced by undetermined amounts of β-Ce in the sample due to thermal cycling.

The agreement between the wave velocity and lattice dynamical θ_D values for γ-Ce is very reasonable considering the differing methods by which they were calculated. The results of the present experiment are again consistent with the results of polycrystalline measurements.

The lattice specific heat calculated in the present analysis is more amenable to comparison with former experiments than is the Debye temperature. Thermodynamic measurements yield the specific heat at constant pressure, C_p. However, this C_p value is easily related to the specific heat at constant volume according to

$$C_p = C_V + C_d \quad , \tag{3.88}$$

where C_d is the dilatation term given by

$$C_d = \frac{TV9\alpha^2}{K_T} \quad . \tag{3.89}$$

Here T is the absolute temperature, V is the atomic volume, α is the linear thermal expansion coefficient, and K_T is the isothermal compressibility. The total specific heat at constant volume for a metal is normally given by

$$C_V = C_V^{\ell} + C_V^{e} \quad , \tag{3.90}$$

where C_V^{ℓ} is the lattice specific heat and C_V^{e} is the contribution to the specific heat arising from the conduction electrons. However, an extra term, C_V^{f}, must be included in the expression for C_V for γ-Ce due to the contribution of the thermal excitation of 4f electrons from the ground state to the next higher level(s) of the 4f multiplet. This term can be calculated according to

$$C_V^{f} = N_a \frac{d}{dt} \left[\frac{\sum_J (2J+1) E_J e^{-E_J/kT}}{\sum_J (2J+1) e^{-E_J/kT}} \right] \tag{3.91}$$

where N_a is Avogadro's number, J is the total angular momentum quantum number, and the E_J values are the energy levels of the multiplet. For most rare earth metals this term essentially goes to zero and can be ignored, however, for γ-Ce it is large enough to be included. Therefore,

Equation (3.88) applied to γ-Ce becomes

$$C_p = C_V^{\ell} + C_V^{e} + C_V^{f} + C_d \quad . \tag{3.92}$$

The only recent experimental determination of C_p for γ-Ce is based on an enthalpy measurement performed in 1960 (55). The sample used for the enthalpy measurements was less pure (with respect to other elements) than the γ-Ce used in the present experiment. Also the allotropic content of the sample used for the enthalpy measurements is unknown since the measurements were performed between 0°C and 1100°C and β-Ce can begin to form at temperatures as high as 5°C. However, the value obtained for C_p at room temperature from the enthalpy measurements agrees very well with the room temperature C_p value which was calculated according to Equation (3.92) using the lattice specific heat value obtained from the present analysis. This comparison is given in Table 3.7.

The value of C_p at 300° which was calculated from the present analysis was determined in the following manner. The value for C_p^f was determined according to Equation (3.91), and a value for C_V^e was estimated from values given by former analyses of the C_p data given by Reference 55 into component terms (57,58). The dilatation term [Equation (3.89)] was recalculated due to the availability of more recent values for V (9), α (54), and K_T, which are more accurate than the values used in the analysis given by References 57 and 58. (K_T was calculated according to Equation (3.82) from the K_S value given by References 46 and 50 in Table 3.6.)

Table 3.7. Specific heat and Debye temperature of γ-Ce at room temperature

Property	Value	Reference
C_p (cal/°K)	6.45	55
	6.46	Present work
θ_D (°K)	144	49
	139	47
	135[a]	50
	135	46
	119	Present work

[a] A value for θ_D was not quoted in Reference 50. The Debye temperature listed was calculated from the wave velocity values given by Reference 50.

The measured C_p value and the C_p value obtained from the present analysis agree very well at room temperature. This is to be expected, however, since C_V^{ℓ}, which is the largest contribution to C_p, is approaching a constant value of 3R at this temperature. A comparison of the present specific heat results and other experimental values for the temperature range between the Debye and the Dulong-Petit regions would be more meaningful. However, no low temperature specific heat data for γ-Ce are available due to the formation of the β and α phases upon cooling.

The temperature dependent transformation properties of γ-Ce and the lack of single crystal data for γ-Ce preclude a rigorous comparison of the lattice dynamical results of the present analysis with former experimental results. However, according to the analysis presented in this section, the elastic and thermodynamic results of the present work are consistent with the results of former measurements on polycrystalline samples. The experimental results for magnetic scattering by γ-Ce will be discussed in the following section.

Magnetic Scattering Analysis

The present experiment has produced several significant results concerning the magnetic scattering of γ-Ce. These single crystal measurements have firmly established the 'quasi-continuum' nature of the magnetic level structure of γ-Ce. Former inelastic magnetic scattering measurements on γ-Ce were performed on polycrystalline samples. Due to the difficulty in identification of various contributions to the scattering from polycrystalline samples, peaks observed in the

frequency range of 1.4-2.3 THz were variously ascribed to one-pnonon or magnetic scattering by various authors (36,37).

The inelastic magnetic scattering from a single crystal, however, can be isolated from the one-phonon scattering by performing the measurements at "equivalent zone center" Q values where the phonon frequencies go to zero. (See Chapter II, Measurement Techniques.) This procedure was utilized in the present experiment and the observed scattering gave no indication of a discrete magnetic excitation lying anywhere in the frequency region .8-3.8 THz. Therefore, the peaks observed in former polycrystalline measurement can be unambiguously ascribed to phonon scattering.

In the context of the present experiment the magnetic scattering was observed using constant Q scans. The variation of the scattering intensity with Q value, for a given energy transfer, can also be obtained from the data by analyzing several scans which were performed over the same energy range with different Q values. For example, the data obtained from the three constant Q scans given in Figure 2.8 have been plotted as a function of Q for energy transfers of 2.9, 3.1, and 3.5 THz in Figure 3.10. This type of analysis, for the same three constant Q scans, was performed for four different energy transfer values in all. The results are summarized in Figure 3.11. The magnetic form factor obtained from Reference 20 is included in Figure 3.11 for comparison.

The magnetic inelastic scattering data given in Figure 3.11 exhibit the expected decrease in intensity with increasing Q, however, they begin to differ significantly from the measured form factor at large Q

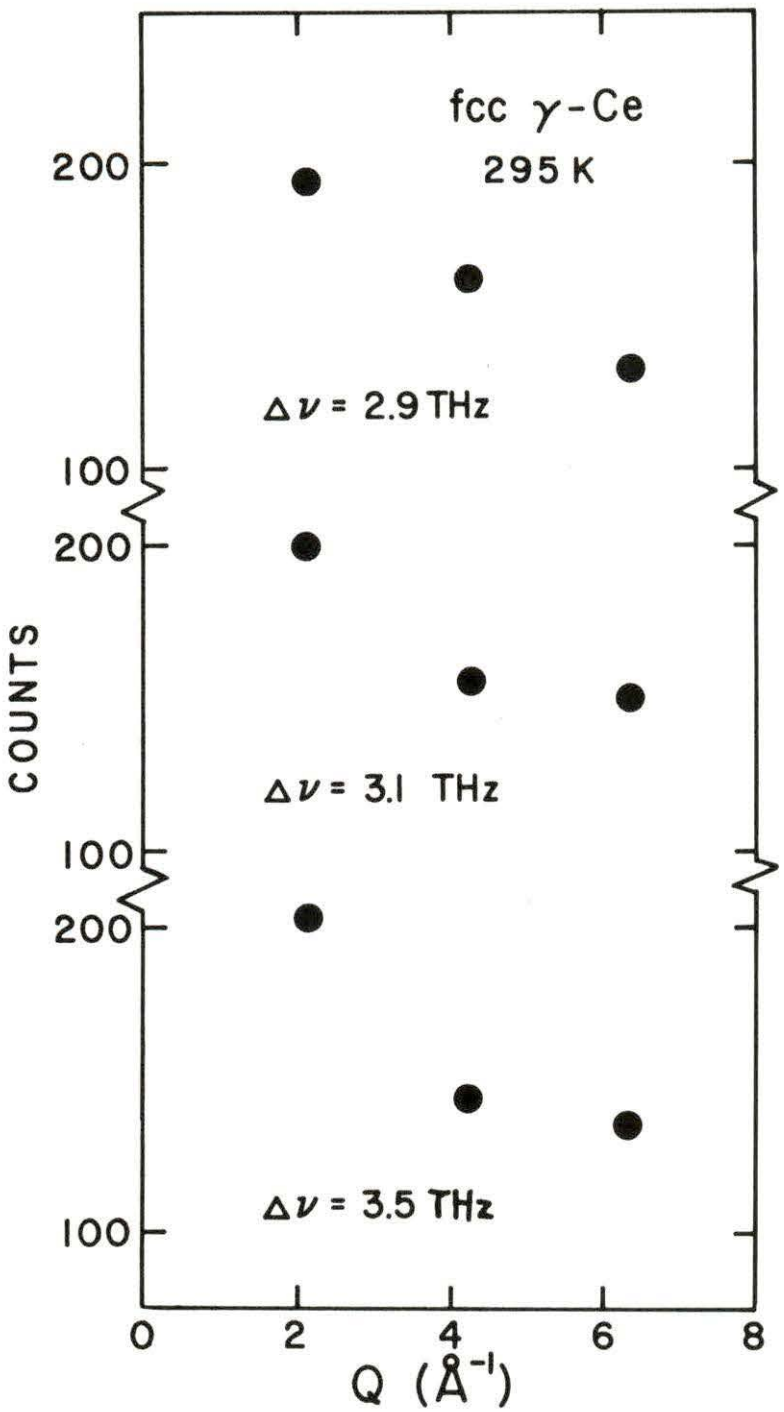

Figure 3.10. Q dependence of the magnetic scattering of γ-Ce for several energy transfer (Δν) values. These graphs were constructed from data given in Figure 2.8

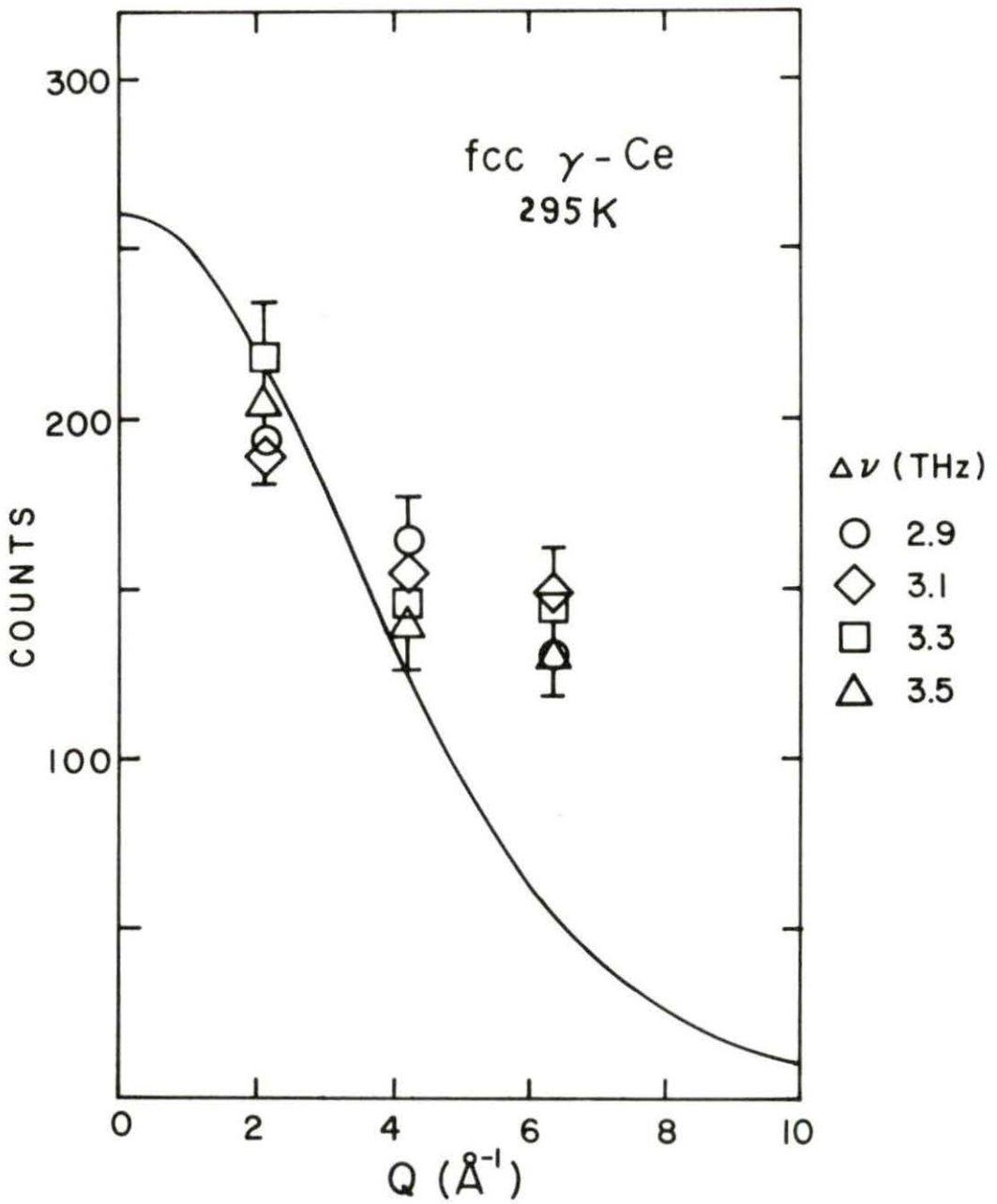

Figure 3.11. Q dependence of the observed magnetic scattering of γ-Ce compared with the form factor given by Reference 20

values. This deviation would undoubtedly be removed by correcting the observed scattering intensities for the contributions due to background scattering. This background arises from multiphonon processes (as described in Appendix D) and from experimental factors such as scattering off the sample container, electronic noise in the counting circuits, etc.

The general features of the magnetic inelastic scattering results of the present analysis correspond to the results of similar measurements performed on a polycrystalline sample of fcc $Ce_{0.74}Th_{0.26}$ (38). The phonon contribution to the observed scattering of $Ce_{0.74}Th_{0.26}$ was estimated by making identical measurements on a sample of $La_{0.73}Th_{0.27}$ which was the same size as the $Ce_{0.74}Th_{0.26}$ sample. Since La is non-magnetic, the observed scattering from $La_{0.73}Th_{0.27}$ must all be nuclear in origin, i.e., phonon scattering. Therefore, the inelastic magnetic scattering contribution is extracted from the observed scattering intensity of $Ce_{0.74}Th_{0.26}$ by performing a point-by-point subtraction of the intensity observed for $La_{0.73}Th_{0.27}$. (The $La_{0.73}Th_{0.27}$ scattering intensity was suitably weighted before subtraction to account for the different scattering amplitudes of Ce and La.)

An estimate for the background in these measurements was obtained from the scattering intensity observed for the $La_{0.73}Th_{0.27}$ sample at energy transfers above 30 meV (7.25 Thz). This energy transfer value is well above phonon energies, and since La exhibits no magnetic scattering, all scattering observed above 30 meV is assumed to be due to coherent multiphonon scattering, incoherent processes, and experimental

factors. This background is assumed to be constant at all energy transfer values and is also assumed to be a valid background level for the $Ce_{0.74}Th_{0.26}$ scattering intensity.

The polycrystalline $Ce_{0.74}Th_{0.26}$ data which have been corrected for one-phonon and background scattering are qualitatively similar to the results of the present experiment. No detailed comparison of the $Ce_{0.74}Th_{0.26}$ data and the uncorrected γ-Ce data can be made. However, the preliminary examination of these data presented below reveals an interesting result.

According to Figure 3.11 the energy scans made at Q values of 2.1 $\AA^{-1}$ and 4.2 $\AA^{-1}$ correspond to the magnetic form factor fairly well. Therefore, there is little background correction necessary for the energy scans performed at these Q values. A qualitative comparison of these two energy scans with the $Ce_{0.74}Th_{0.26}$ energy scans reveals that the γ-Ce intensity drops much faster than the $Ce_{0.74}Th_{0.26}$ intensity. Now, the broad single feature in the scattering produced by a quasi-continuum of magnetic energy levels is characterized by a half width, Γ. Therefore, the faster intensity drop in γ-Ce corresponds to half width, Γ_{Ce}, that is narrower than $\Gamma_{Ce\text{-}Th}$. Earlier magnetic scattering work on polycrystalline γ-Ce suggests a value of Γ_{Ce} that is roughly half as large as $\Gamma_{Ce\text{-}Th}$ (37). (These polycrystalline measurements were corrected for phonon scattering in a manner similar to the procedure used for $Ce_{0.74}Th_{0.26}$.) The value for Γ_{Ce} estimated from the present data, however, appears to be even less than the former Γ_{Ce} value by as much as 50-60%. At present, this feature of the magnetic scattering of γ-Ce

has been compared only qualitatively with former measurements. A more rigorous comparison between the present γ-Ce data and former γ-Ce and $Ce_{0.74}Th_{0.26}$ results will be made when additional data for γ-Ce are obtained and an accurate background correction is applied.

The corrections used for the polycrystalline γ-Ce and $Ce_{0.74}Th_{0.26}$ data are reasonable approximations incorporated to yield estimates for the one-phonon and background contributions to the total scattering. However, the single crystal data obtained in the present experiment will be amenable to a more accurate correction procedure after additional data are obtained. The supplementary data will be measured in collaboration with Dr. R. M. Nicklow of Oak Ridge National Laboratory. The proposed correction procedure and the extra data required to perform this correction are discussed in Appendix D.

Summary

The phonon and magnetic measurements of the present experiment have produced the following significant results concerning the lattice dynamical and magnetic properties of γ-Ce.

- The phonon spectrum is relatively soft, which is consistent with results obtained for $CeSn_3$.
- The L [110] and T [111] branches of the dispersion curve are anomalous.
- The c_{11} and c_{44} elastic constants are quite close in value.
- No discrete magnetic excitations were observed.
- The magnetic scattering is qualitatively similar to the results from $Ce_{0.74}Th_{0.26}$, however, $\Gamma_{Ce} < \Gamma_{Ce\text{-}Th}$.

The various lattice dynamical and magnetic similarities among γ-Ce, $CeSn_3$, and $Ce_{0.74}Th_{0.26}$ are particularly intriguing since $CeSn_3$ and $Ce_{0.74}Th_{0.26}$ are mixed valence compounds. Therefore, a complete theoretical description of the observed properties of Ce and its compounds may provide a basis for understanding a whole class of mixed valence materials.

APPENDIX A

The symmetry reduction of the independent interatomic force constants for two to eight neighbors in an fcc crystal is presented below. The various neighbor positions are illustrated in Figure A.1 for reference.

The second nearest neighbor from the origin is the nearest atom along the cube edge i.e., at $\ell_2 = (1,0,0)$. There are eight symmetry operations that leave this "bond" invariant and eight that reverse it as listed below.

"Invariant" Operations

1) Identity.
$$\begin{pmatrix} 1 & 0 & 0 \\ 0 & 1 & 0 \\ 0 & 0 & 1 \end{pmatrix}$$

2) Reflection in the (010) plane.
$$\begin{pmatrix} 1 & 0 & 0 \\ 0 & -1 & 0 \\ 0 & 0 & 1 \end{pmatrix}$$

3) Reflection in the (001) plane.
$$\begin{pmatrix} 1 & 0 & 0 \\ 0 & 1 & 0 \\ 0 & 0 & -1 \end{pmatrix}$$

4) Reflection in the (011) plane.
$$\begin{pmatrix} 1 & 0 & 0 \\ 0 & 0 & -1 \\ 0 & -1 & 0 \end{pmatrix}$$

5) 2-fold rotation about the bond axis.
$$\begin{pmatrix} 1 & 0 & 0 \\ 0 & -1 & 0 \\ 0 & 0 & -1 \end{pmatrix}$$

6) Counterclockwise (CCW) 4-fold rotation about the bond axis.
$$\begin{pmatrix} 1 & 0 & 0 \\ 0 & 0 & -1 \\ 0 & 1 & 0 \end{pmatrix}$$

7) Clockwise (CW) 4-fold rotation about the bond axis.
$$\begin{pmatrix} 1 & 0 & 0 \\ 0 & 0 & 1 \\ 0 & -1 & 0 \end{pmatrix}$$

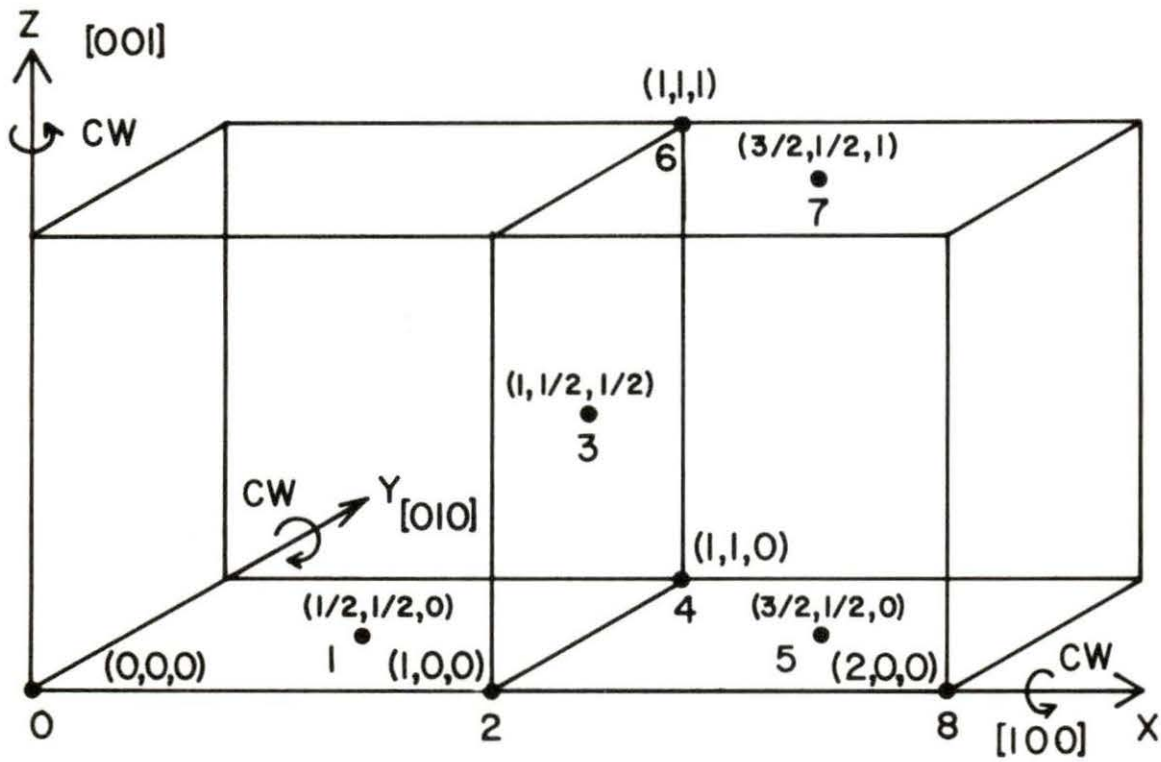

Figure A.1. N-th neighbor positions in a monatomic fcc lattice for 1-8 neighbors. Clockwise rotation directions about each axis are also indicated

8) CCW 4-fold rotation about the bond axis, followed by reflection in the (001) plane.

$$\begin{pmatrix} 1 & 0 & 0 \\ 0 & 0 & 1 \\ 0 & 1 & 0 \end{pmatrix}$$

"Reversal" Operations

1) Inversion.

$$\begin{pmatrix} -1 & 0 & 0 \\ 0 & -1 & 0 \\ 0 & 0 & -1 \end{pmatrix}$$

2) 2-fold rotation about the [010] direction.

$$\begin{pmatrix} -1 & 0 & 0 \\ 0 & 1 & 0 \\ 0 & 0 & -1 \end{pmatrix}$$

3) 2-fold rotation about the [001] direction.

$$\begin{pmatrix} -1 & 0 & 0 \\ 0 & -1 & 0 \\ 0 & 0 & 1 \end{pmatrix}$$

4) 2-fold rotation about the [011] direction.

$$\begin{pmatrix} -1 & 0 & 0 \\ 0 & 0 & 1 \\ 0 & 1 & 0 \end{pmatrix}$$

5) Reflection in the (100) plane.

$$\begin{pmatrix} -1 & 0 & 0 \\ 0 & 1 & 0 \\ 0 & 0 & 1 \end{pmatrix}$$

6) CW 4-fold rotation about the bond axis, followed by reflection in the (100) plane.

$$\begin{pmatrix} -1 & 0 & 0 \\ 0 & 0 & 1 \\ 0 & -1 & 0 \end{pmatrix}$$

7) CCW 4-fold rotation about the bond axis, followed by reflection in the (100) plane.

$$\begin{pmatrix} -1 & 0 & 0 \\ 0 & 0 & -1 \\ 0 & 1 & 0 \end{pmatrix}$$

8) CCW 4-fold rotation about the bond axis, followed by a 2-fold rotation about the (001) axis.

$$\begin{pmatrix} -1 & 0 & 0 \\ 0 & 0 & -1 \\ 0 & -1 & 0 \end{pmatrix}$$

The number of independent interatomic force constants for the second neighbor therefore becomes [Equation (1.45)]

$$N_2 = \frac{1}{16}\{[(3)^2 + 7(1)^2] + [6(3) + 2(-1)]\}$$
$$N_2 = 2 \qquad \text{(A.1)}$$

Here the first square bracket is the sum of the squares of the characters of the "invariant" operations, and the second square bracket is the sum of the characters of the "squares" of the reversal operations. From Equation (A.1) there are only two independent interatomic force constants for the second neighbor. Applying the CCW 4-fold rotation about the bond axis one obtains,

$$\varphi(000,\ 100)=\begin{pmatrix}1&0&0\\0&0&-1\\0&1&0\end{pmatrix}\begin{pmatrix}xx&xx&xz\\xy&yy&yz\\zy&yz&zz\end{pmatrix}\begin{pmatrix}1&0&0\\0&0&1\\0&-1&0\end{pmatrix}$$

$$\varphi(000,\ 100)=\begin{pmatrix}xx&-xz&xy\\-xz&zz&-yz\\xy&-yz&yy\end{pmatrix} \quad . \tag{A.2}$$

Comparing the original matrix with the transformed matrix yields the following results; xy = -xz and xy = xz, therefore xy = xz = 0; yy = zz; -yz = yz = 0. Therefore, the interatomic force constant matrix for second neighbors becomes,

$$\varphi(000,\ 100) = \begin{pmatrix}xx&0&0\\0&yy&0\\0&0&yy\end{pmatrix} \quad . \tag{A.3}$$

The third nearest neighbor to the origin is located at $\ell_3 = (1, \frac{1}{2}, \frac{1}{2})$. There is only one symmetry operation other than the identity that leaves this position unchanged with respect to the origin as listed below.

"Invariant" Operations

1) Identity.

2) CW 4-fold rotation about the [100] direction, followed by reflection in the (010) plane. $\begin{pmatrix} 1 & 0 & 0 \\ 0 & 0 & 1 \\ 0 & 1 & 0 \end{pmatrix}$

"Reversal" Operations

1) Inversion

2) CW 4-fold rotation about the [100] direction, followed by a 2-fold rotation about the [010] direction. $\begin{pmatrix} -1 & 0 & 0 \\ 0 & 0 & -1 \\ 0 & -1 & 0 \end{pmatrix}$

Thus, Equation (1.45) becomes

$$N_3 = \tfrac{1}{4}\{[(3)^2 + (1)^2] + [3 + 3]\}$$
$$N_3 = 4 \quad , \tag{A.4}$$

indicating that there are four independent interatomic force constants for the third neighbor. Applying the above 4-fold rotation and reflection, one obtains,

$$\varphi(000, 1\tfrac{1}{2}\tfrac{1}{2}) = \begin{pmatrix} 1 & 0 & 0 \\ 0 & 0 & 1 \\ 0 & 1 & 0 \end{pmatrix} \begin{pmatrix} xx & xy & xz \\ xy & yy & yz \\ xy & yz & zz \end{pmatrix} \begin{pmatrix} 1 & 0 & 0 \\ 0 & 0 & 1 \\ 0 & 1 & 0 \end{pmatrix}$$

$$\varphi(000, 1\tfrac{1}{2}\tfrac{1}{2}) = \begin{pmatrix} xx & xz & xy \\ xz & zz & yz \\ xy & yz & yy \end{pmatrix} \quad . \tag{A.5}$$

Comparison to the original matrix reveals that xz = xy and yy = zz. Therefore, the interatomic force constant matrix for the third neighbor

becomes

$$\varphi(000,\ 1\tfrac{1}{2}\tfrac{1}{2}) = \begin{pmatrix} xx & xz & xz \\ xz & yy & yz \\ xz & yz & yy \end{pmatrix} \quad . \tag{A.6}$$

The "bond" between the fourth neighbor and the atom at the origin in forms a face diagonal of the cubic unit cell. Therefore, the fourth neighbor lies along the same line as the first neighbor, only at twice the distance, $\ell_4 = (1,1,0)$. Thus, the symmetry operations that leave the fourth neighbor position invariant with respect to the origin are exactly the same as those that leave the first neighbor "bond" unchanged (see Chapter I, Symmetry Considerations). Hence the independent interatomic force constants for the fourth neighbor are the same as for the first neighbor and one may write

$$\varphi(000,\ 110) = \begin{pmatrix} xx & xy & 0 \\ xy & xx & 0 \\ 0 & 0 & zz \end{pmatrix} \quad . \tag{A.7}$$

The fifth neighbor is located at $\ell = (\frac{3}{2},\ \frac{1}{2},\ 0)$ as shown in Figure (A.1). Here there is only one operation that leaves the bond invariant besides the identity.

"Invariant" Operations

1) Identity.

2) Reflection in the (001) plane. $\begin{pmatrix} 1 & 0 & 0 \\ 0 & 1 & 0 \\ 0 & 0 & -1 \end{pmatrix}$

"Reversal" Operations

1) Inversion

2) 2-fold rotation about the [001] direction. $\begin{pmatrix} -1 & 0 & 0 \\ 0 & -1 & 0 \\ 0 & 0 & 1 \end{pmatrix}$

Equation (1.45) becomes

$$N = \tfrac{1}{4}\{(3)^2 + (1)^2] + [3 + 3]\}$$

$$N = 4 \qquad \text{(A.8)}$$

for fifth neighbors. Application of the above reflection to the interatomic force constant matrix yields

$$\varphi(000, \tfrac{3}{2}\tfrac{1}{2}0) = \begin{pmatrix} 1 & 0 & 0 \\ 0 & 1 & 0 \\ 0 & 0 & -1 \end{pmatrix}\begin{pmatrix} xx & xy & xz \\ xy & yy & yz \\ xz & yz & zz \end{pmatrix}\begin{pmatrix} 1 & 0 & 0 \\ 0 & 1 & 0 \\ 0 & 0 & -1 \end{pmatrix}$$

$$\varphi(000, \tfrac{3}{2}\tfrac{1}{2}0) = \begin{pmatrix} xx & xy & -xz \\ xy & yy & -yz \\ -xz & -yz & zz \end{pmatrix} . \qquad \text{(A.9)}$$

Therefore, $xz = 0$ and $yz = 0$, and the matrix becomes

$$\varphi(000, \tfrac{3}{2}\tfrac{1}{2}0) = \begin{pmatrix} xx & xy & 0 \\ xy & yy & 0 \\ 0 & 0 & zz \end{pmatrix} . \qquad \text{(A.10)}$$

The body diagonal of the cubic unit cell connects the atom at the origin with the sixth neighbor. Therefore $\ell_6 = (1,1,1)$. Here there are four "invariant" and four "reversal" operations as listed below.

"Invariant" Operations

1) Identity.

2) CCW 3-fold rotation about the bond axis. $\begin{pmatrix} 0 & 0 & 1 \\ 1 & 0 & 0 \\ 0 & 1 & 0 \end{pmatrix}$

3) CW 3-fold rotation about the bond axis. $\begin{pmatrix} 0 & 1 & 0 \\ 0 & 0 & 1 \\ 1 & 0 & 0 \end{pmatrix}$

4) Reflection in the $(1\bar{1}0)$ plane. $\begin{pmatrix} 0 & 1 & 0 \\ 1 & 0 & 0 \\ 0 & 0 & 1 \end{pmatrix}$

"Reversal" Operations

1) Inversion

2) CCW 3-fold rotation about the bond axis, followed by inversion. $\begin{pmatrix} 0 & 0 & -1 \\ -1 & 0 & 0 \\ 0 & -1 & 0 \end{pmatrix}$

3) CW 3-fold rotation about the bond axis, followed by inversion. $\begin{pmatrix} 0 & -1 & 0 \\ 0 & 0 & -1 \\ -1 & 0 & 0 \end{pmatrix}$

4) 2-fold rotation about the $[1\bar{1}0]$ direction. $\begin{pmatrix} 0 & -1 & 0 \\ -1 & 0 & 0 \\ 0 & 0 & -1 \end{pmatrix}$

Thus, for the sixth neighbor Equation (1.45) yields,

$$N = \frac{1}{8} \{[(3)^2 + (1)^2] + [3 + 3]\}$$

$$N = 2 \quad . \tag{A.11}$$

Applying the CCW 3-fold rotation one obtains

$$\varphi(000, 111) = \begin{pmatrix} 0 & 0 & 1 \\ 1 & 0 & 0 \\ 0 & 1 & 0 \end{pmatrix} \begin{pmatrix} xx & xy & xz \\ xy & yy & yz \\ xz & yz & zz \end{pmatrix} \begin{pmatrix} 0 & 1 & 0 \\ 0 & 0 & 1 \\ 1 & 0 & 0 \end{pmatrix}$$

$$\varphi(000,\ 111) = \begin{pmatrix} zz & xz & yz \\ xz & xx & xy \\ yz & xy & yy \end{pmatrix} \quad . \tag{A.12}$$

Therefore, xx = zz, xz = xy = yz, and yy = xx. Thus, the matrix of independent interatomic force constants becomes

$$\varphi(000,\ 111) = \begin{pmatrix} xx & yz & yz \\ yz & xx & yz \\ yz & yz & xx \end{pmatrix} \quad . \tag{A.13}$$

The seventh nearest neighbor is located at $\ell_7 = (\frac{3}{2},\ 1,\ \frac{1}{2})$, as shown in Figure (A.1). There are no symmetry operations which leave this bond invariant or reversed, other than the identity and inversion, respectively. Therefore, from Equation (1.45),

$$N = \tfrac{1}{2}\{(3)^2 + 3\}$$

$$N = 6 \quad . \tag{A.14}$$

Thus, the matrix for seventh neighbors cannot be simplified beyond the reduction obtained from permutation symmetry as discussed in Chapter I.

$$\varphi(000, \tfrac{3}{2},\ 1,\ \tfrac{1}{2}) = \begin{pmatrix} xx & xy & xz \\ xy & yy & yz \\ xz & yz & zz \end{pmatrix} \tag{A.15}$$

The eighth neighbor is located at $\ell = (2,0,0)$, which is along the cube edge and at twice the distance of the second neighbor. Therefore, all the symmetry operations which leave the second neighbor bond invariant also leave the eighth neighbor bond invariant. Therefore, from

Equation (A.3),

$$\varphi(000,\ 200) = \begin{pmatrix} xx & 0 & 0 \\ 0 & yy & 0 \\ 0 & 0 & yy \end{pmatrix} \quad . \tag{A.16}$$

APPENDIX B

Data taken at Ames Laboratory are tabulated in this appendix. Several phonons obtained with the first small γ-Ce crystal are listed in Table B.1. The scattering from this sample was very weak and contaminated from higher order processes, therefore, these data are subject to large errors. As previously mentioned, a great deal of the Mitsubishi data obtained from the second sample was also ambiguous due to spurious structure in the scans. Measurements performed with the Triax identified the phonon scattering in these ambiguous regions. Therefore, Table B.2 presents only that Mitsubishi data from the second sample which was later confirmed as phonon scattering. The Triax data itself is presented in Table B.3. No errors are listed for any of the data in this Appendix as they were not used in the analysis. All measurements listed here were performed with neutron energy loss except those indicated by a superscript "a" which were energy gain measurements.

Table B.1. Mitsubishi data from the first sample

Branch	$\vec{q}$ (ξ)	ν (THz)	$\vec{\tau}$
L [111]	.05	.4	111
	.10	.88	111
	.15	1.35	111
T [111]	.1	.53	002
	.2	1.03	002

Table B.2. Mitsubishi data from the second sample

Branch	$\vec{q}$ (ξ)	ν (THz)	$\vec{\tau}$
L [001]	.1	.35	002
	.2	.78	002
	.3	1.20	002
	.4	1.55[a]	002
	.5	1.88[a]	002
	.6	2.20[a]	002
	.7	2.45[a]	002
	.8	2.73[a]	002
T [001]	.2	.55	111
	.3	.96[a]	220
	.4	1.25[a]	220
	.5	1.50[a]	220
	.6	1.70[a]	220
	.7	1.90[a]	220
	.8	2.00[a]	220
L [110]	.1	.62	220
	.2	1.25	220
T_2 [110]	.1	.45	002
	.2	.95	002
	.3	1.40	002
	.4	1.80	002
	.5	2.25[a]	002
L [111]	.2	1.7	111
	.3	2.25[a]	111
T [111]	.1	.50	002
	.2	.75	002
	.3	.93	002
	.4	.82	002
	.5	.75	002

[a]Phonons taken with a neutron energy gain process. All other data listed were obtained with a neutron energy loss process.

Table B.3. Triax data from the second sample sample

Branch	$\vec{q}$ (ξ)	ν (THz)	$\vec{\tau}$
L [001]	.2	.76	002
	.3	1.15	002
	.4	1.51	002
	.6	2.10	002
	.7	2.45	002
T [001]	.3	.985	220
	.4	1.285	220
	.5	1.50	220
	.6	1.735	220
	.7	1.90	220
	1.0	2.00	220
L [110]	.1	.60	220
	.2	1.28	220
	.3	1.735	220
	.4	2.09	220
	.5	2.20	220
	.6	2.20	220
	.7	2.10	220
	.9	2.04	220
T_2 [110]	.1	.45	002
	.2	.95	002
	.3	1.40	002
	.4	1.82	002
	.5	2.15	002
	.6	2.35	002
L [111]	.1	.88	111
	.2	1.65	111
T [111]	.1	.40	002
	.2	.77	002
	.3	.95	002
	.4	.875	002
	.5	.77	002

APPENDIX C

This appendix contains listings of the AFC's and elastic constants generated by various n-th neighbor fitting procedures. The densities of states generated from various sets of AFC's are also presented graphically. A key to the tables is given below.

Table C.1) 4NN Fit #1 - general tensor fit.

4NN Fit #2 - axially symmetric fit, weight = 100.

6NN Fit #1 - modified tensor fit, two axially symmetric conditions: $3(5XX) - 3(5YY) - 8(5XY) = 0$

$(5XX) - 9(5YY) + 8(5ZZ) = 0$

6NN Fit #2 - modified tensor fit, 1XY and 1ZZ fixed from values given by 4NN Fit #1.

6NN Fit #3 - axially symmetric fit, weight = 100.

Table C.2) 8NN Fit #1 - modified tensor fit, axially symmetric conditions listed in Table 3.3.

8NN Fit #2 - modified tensor fit, axially symmetric conditions listed in Table 3.3.

8NN Fit #3 - modified tensor fit, AFC's fixed listed in Table 3.3.

8NN Fit #4 - modified tensor fit, AFC's fixed listed in Table 3.3.

8NN Fit #5 - axially symmetric fit, weight = 100.

Each density of states graph was generated by the set of AFC's which was produced by the fitting procedure designated in the figure caption.

Table C.1. AFC's and elastic constants produced by various 4NN and 6NN fitting procedures

AFC	Value (10^4 dynes/cm)				
	4NN Fit #1	4NN Fit #2	6NN Fit #1	6NN Fit #2	6NN Fit #3
1XX	0.50005	0.47576	0.42557	0.44847	0.44023
1ZZ	-0.06055	0.00289	-0.01475	-0.06055	-0.03568
1XY	0.48640	0.46400	0.48532	0.48640	0.46919
2XX	-0.28760	-0.22032	-0.24278	-0.33739	-0.28168
2YY	0.03582	-0.02704	0.00675	0.05256	0.01302
3XX	0.02644	-0.01262	-0.00612	0.03968	0.01276
3YY	-0.00486	0.01008	0.04433	0.02142	0.03205
3YZ	-0.05901	-0.03720	-0.03726	-0.03726	-0.02034
3XZ	0.00082	-0.00876	0.00446	0.00446	-0.00007
4XX	-0.00378	0.01867	-0.00001	-0.02291	0.00228
4ZZ	0.00911	-0.00884	-0.00460	0.04120	0.01636
4XY	0.00129	0.01611	-0.02495	-0.02603	-0.01124
5XX	-	-	0.02032	0.02032	0.01677
5YY	-	-	-0.00618	0.01672	-0.00520
5ZZ	-	-	-0.00949	-0.03240	-0.00846
5XY	-	-	0.00994	0.01048	0.00854
6XX	-	-	-0.02986	-0.02986	-0.03298
6YZ	-	-	-0.00289	-0.00289	-0.00677
Elastic Constants	Value (10^{12} dynes/cm^2)				
c_{11}	.22738	.23236	.23579	.23579	.22990
c_{44}	.20800	.20907	.18129	.18129	.18316
c_{12}	.08659	.08854	.11569	.11569	.11145
$(c_{11}- c_{12}+ c_{44})/3$	.11626	.11763	.10046	.10046	.10054
$(c_{11}+2c_{12}+4c_{44})/3$	.41805	.41523	.39745	.39745	.39514
$(c_{11}- c_{12})/2$	.07040	.07191	.06005	.06005	.05923
$(c_{11}+ c_{12}+2c_{44})/2$	.36498	.36952	.35704	.35704	.35383

Table C.2. AFC's and elastic constants produced by various 8NN fitting procedures

AFC	Value (10^4 dynes/cm)				
	8NN Fit #1	8NN Fit #2	8NN Fit #3	8NN Fit #4	8NN Fit #5
1XX	0.47237	0.41188	0.44847	0.45906	0.44419
1ZZ	-0.08721	0.03377	-0.03941	-0.06059	-0.03885
1XY	0.44955	0.49491	0.48640	0.48640	0.47537
2XX	-0.31061	-0.24004	-0.35876	-0.35876	-0.27709
2YY	0.02849	-0.00680	0.05256	0.05256	0.02874
3XX	0.04096	-0.03718	0.02909	0.03968	0.02254
3YY	0.02046	0.05953	0.02639	0.02110	0.03232
3YZ	-0.04848	-0.04848	-0.03726	-0.03726	-0.00708
3XZ	0.00663	0.00663	0.00446	0.00446	0.00215
4XX	-0.01327	0.00437	-0.02531	-0.02531	-0.00458
4ZZ	0.03369	-0.00159	0.05777	0.05777	0.01246
4XY	0.02206	-0.02331	-0.00609	-0.00609	-0.00036
5XX	0.00434	0.04719	0.04028	0.02969	0.01267
5YY	0.00002	-0.01762	0.01206	0.01206	-0.01151
5ZZ	-0.00052	-0.02572	-0.04849	-0.03790	-0.01476
5XY	0.00162	0.02430	0.02005	0.02005	0.00983
6XX	-0.02288	-0.02288	-0.02288	-0.02288	-0.02996
6YZ	0.00989	0.00989	-0.00568	-0.00568	-0.03114
7XX	0.00695	-0.01448	-0.01102	-0.00573	0.00184
7YY	-0.00866	0.01276	0.00931	0.00401	-0.00125
7ZZ	-0.00517	-0.00517	-0.00517	-0.00517	-0.00037
7YZ	-0.00233	-0.00233	-0.00015	-0.00015	-0.00011
7XZ	-0.00349	-0.00349	0.00212	0.00212	0.01514
7XY	-0.00698	-0.00698	-0.00698	-0.00698	-0.00407
8XX	0.00045	0.00045	0.00045	0.00045	0.00018
8YY	0.01145	0.01145	0.01145	0.01145	0.01666
Elastic Constants	**Value (10^{12} dynes/cm^2)**				
c_{11}	.23888	.23888	.23888	.23888	.23981
c_{44}	.18605	.18605	.18605	.18605	.19433
c_{12}	.08890	.08890	.08890	.08890	.09235
$(c_{11}- c_{12}+ c_{44})/3$	.11201	.11201	.11201	.11201	.11393
$(c_{11}+2c_{12}+4c_{44})/3$	.38695	.38695	.38695	.38695	.40060
$(c_{11}- c_{12})/2$	.07499	.07499	.07499	.07499	.07373
$(c_{11}+ c_{12}+2c_{44})/2$	.34993	.34993	.34993	.34993	.36040

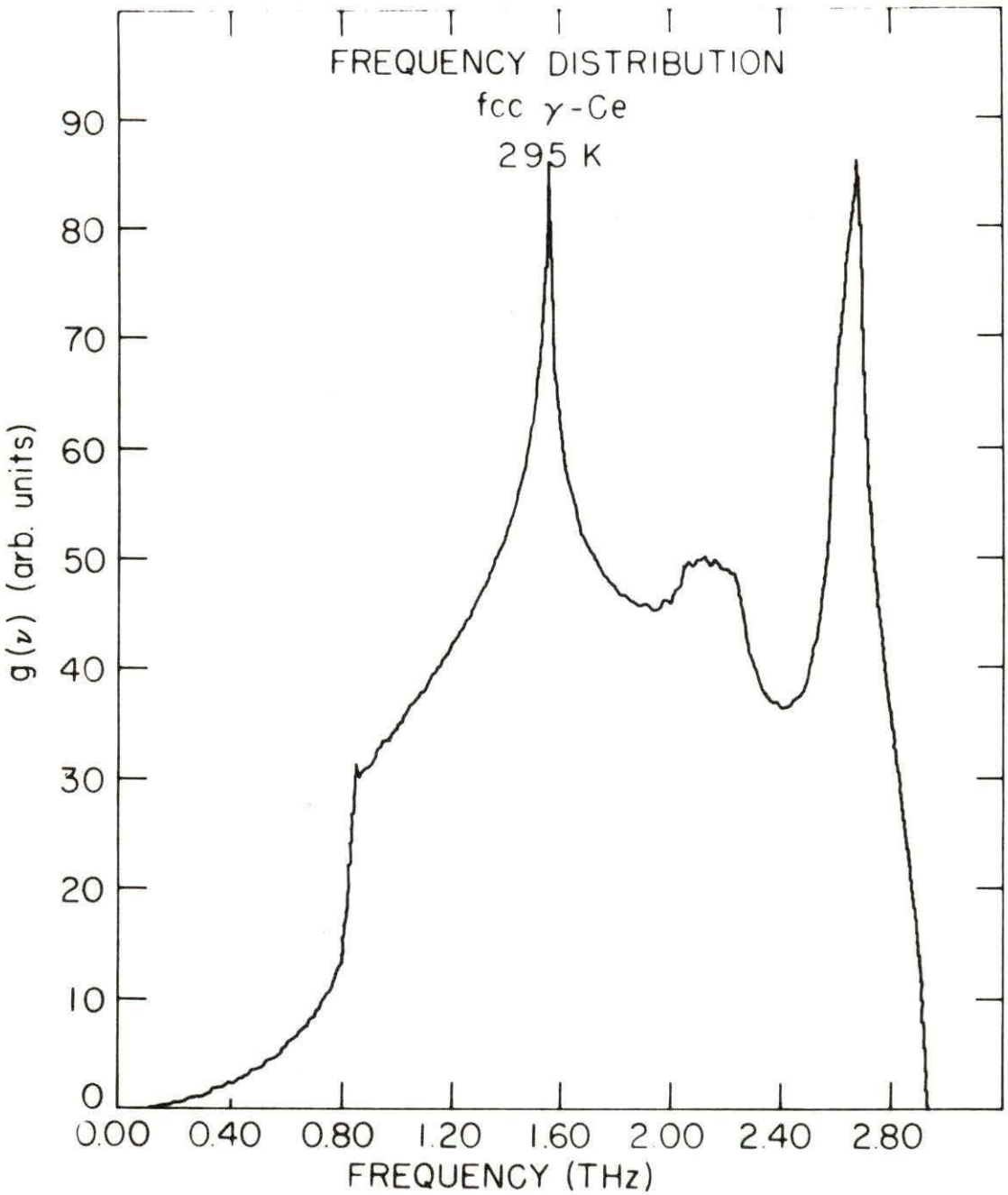

Figure C.1. Density of states calculated from AFC's given by 4NN Fit #1

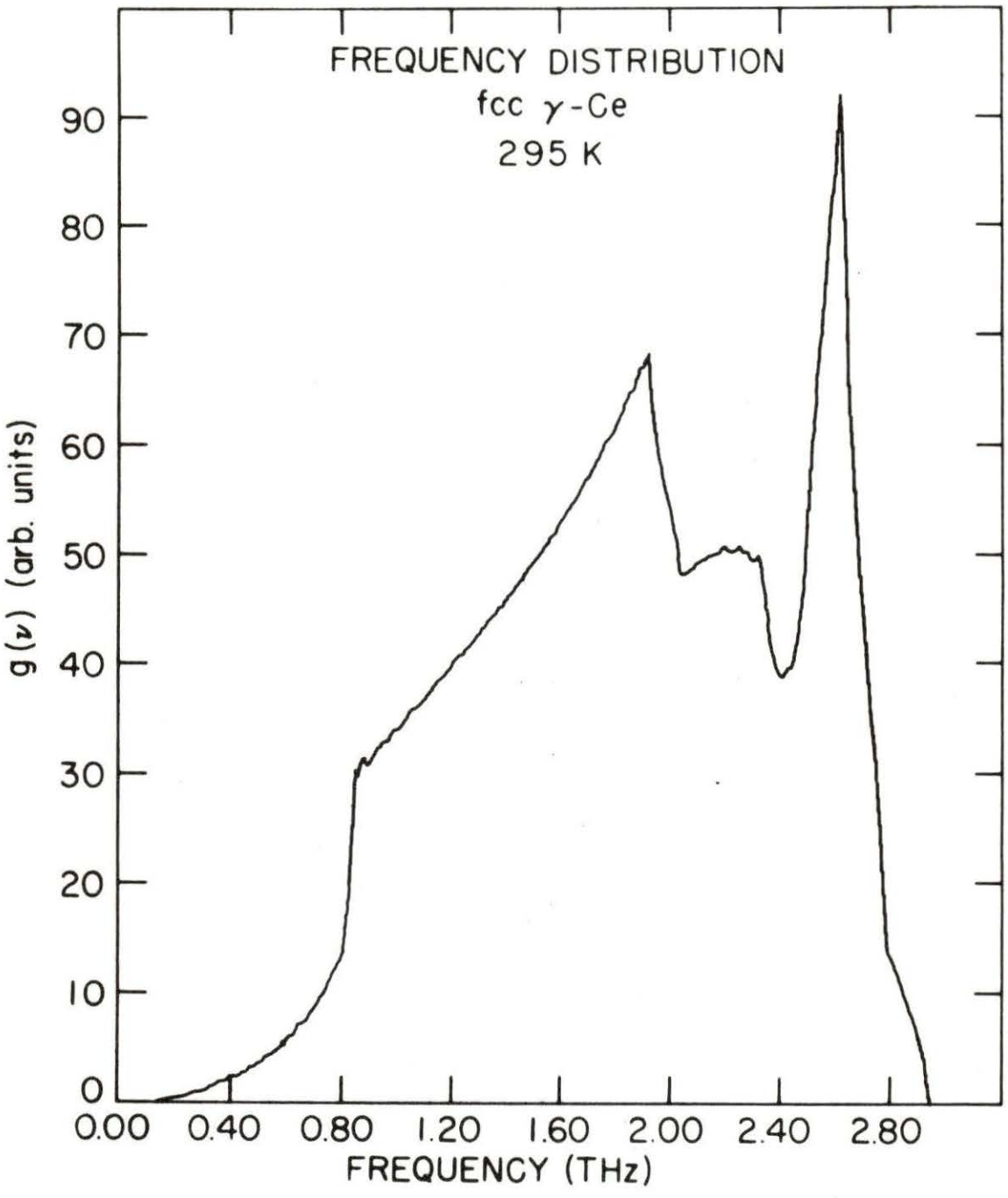

Figure C.2. Density of states calculated from AFC's given by 4NN Fit #2

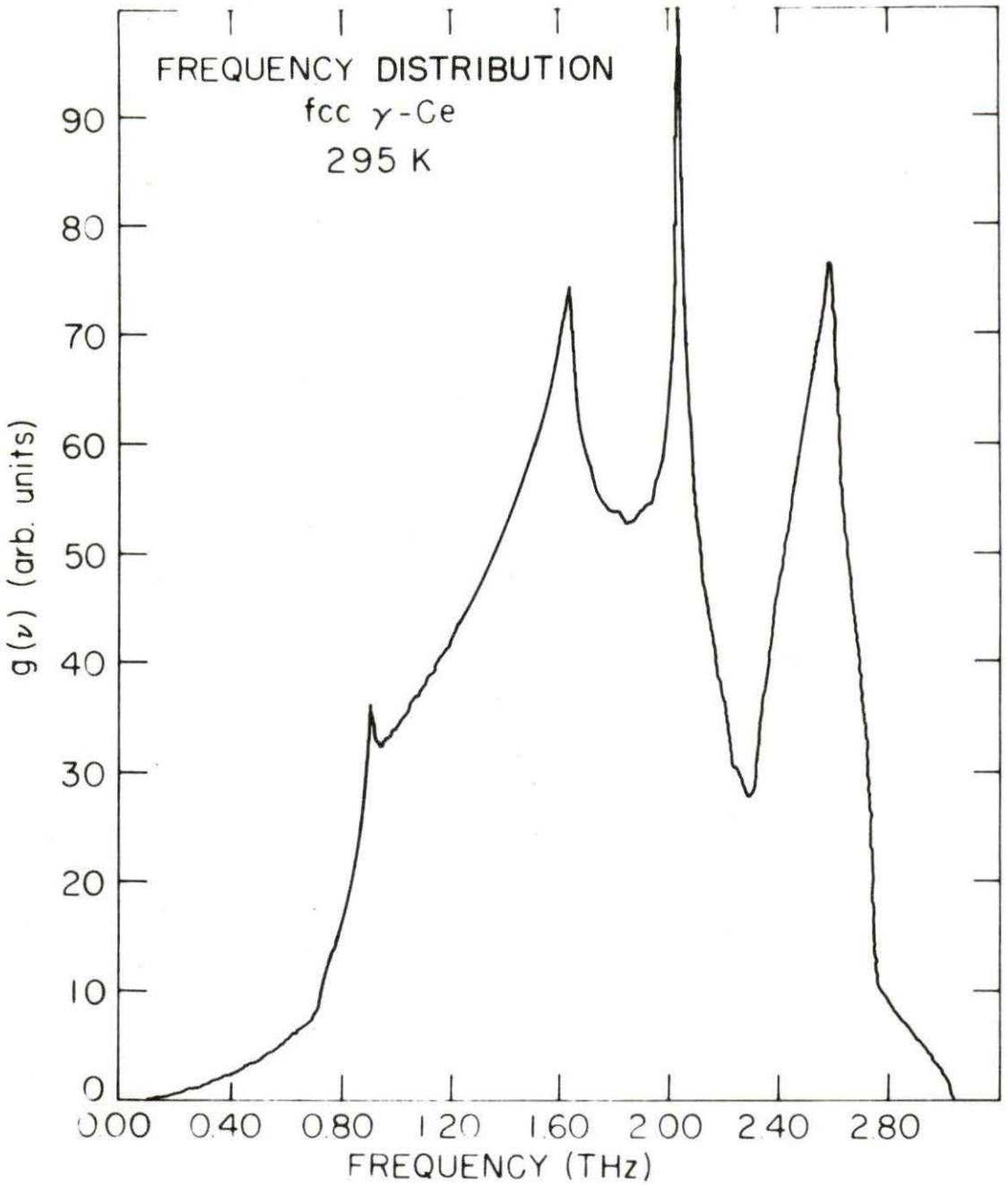

Figure C.3. Density of states calculated from AFC's given by 6NN Fit #1

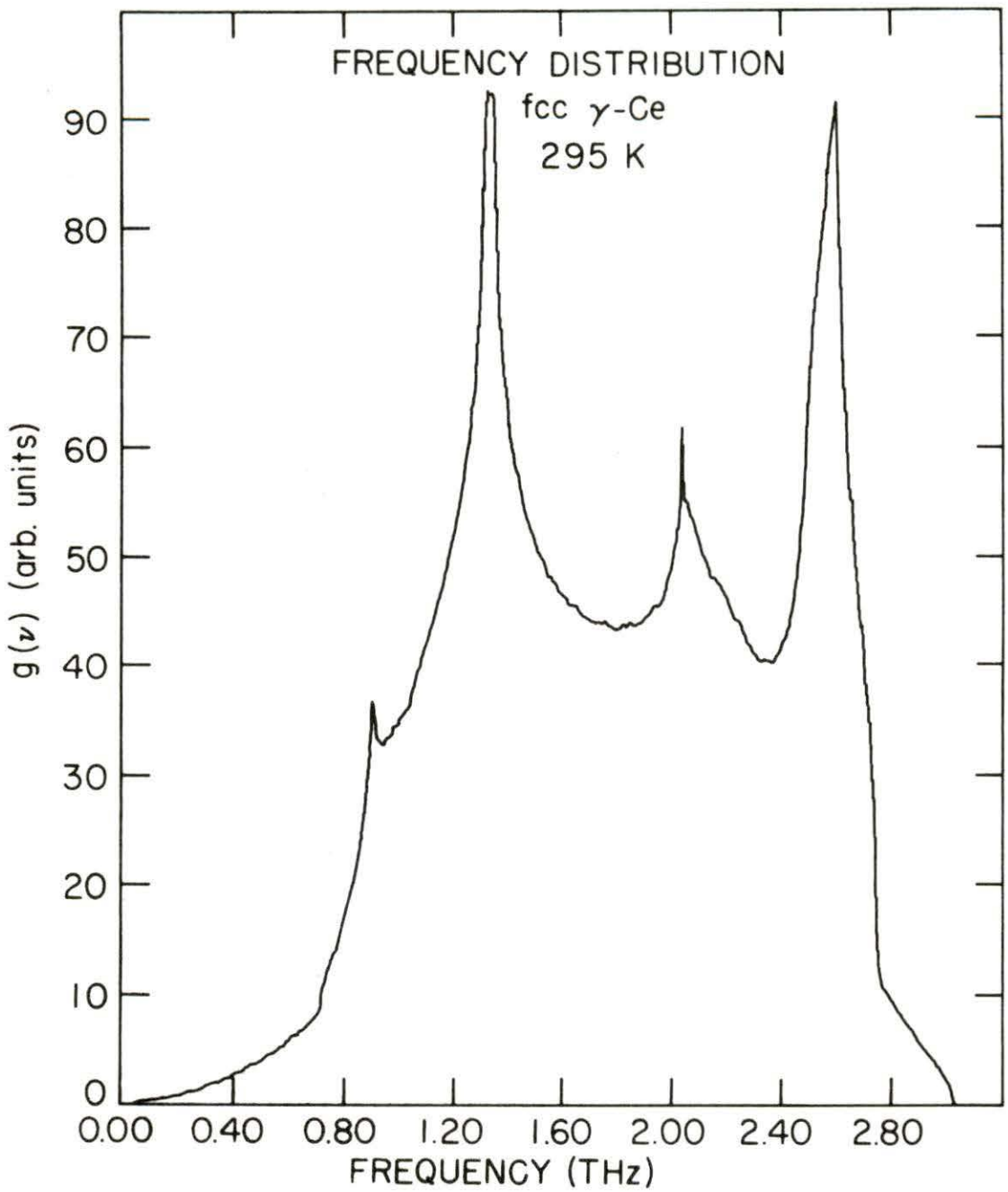

Figure C.4. Density of states calculated from AFC's given by 6NN Fit #2

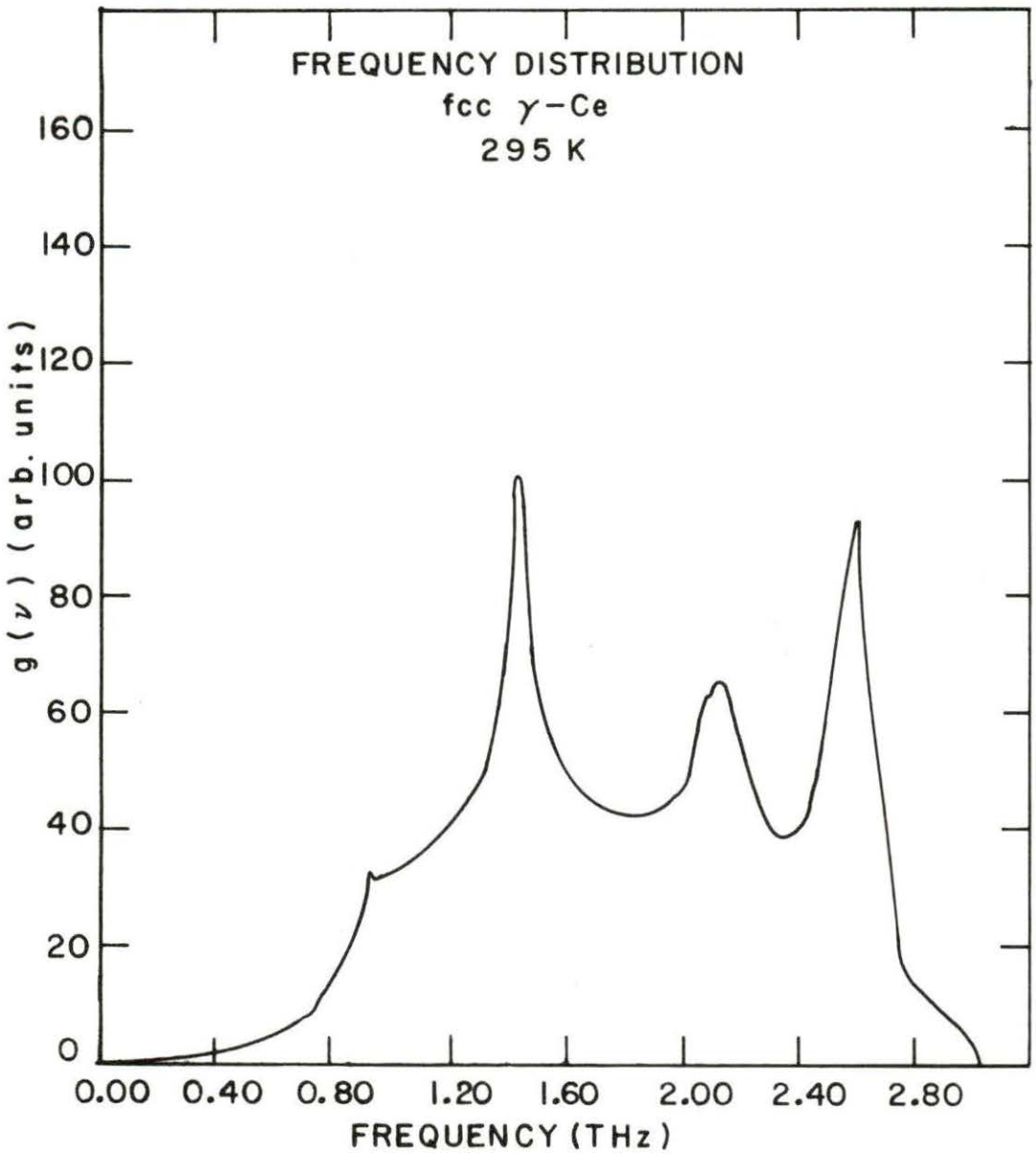

Figure C.5. Density of states calculated from AFC's given by 8NN Fit #1

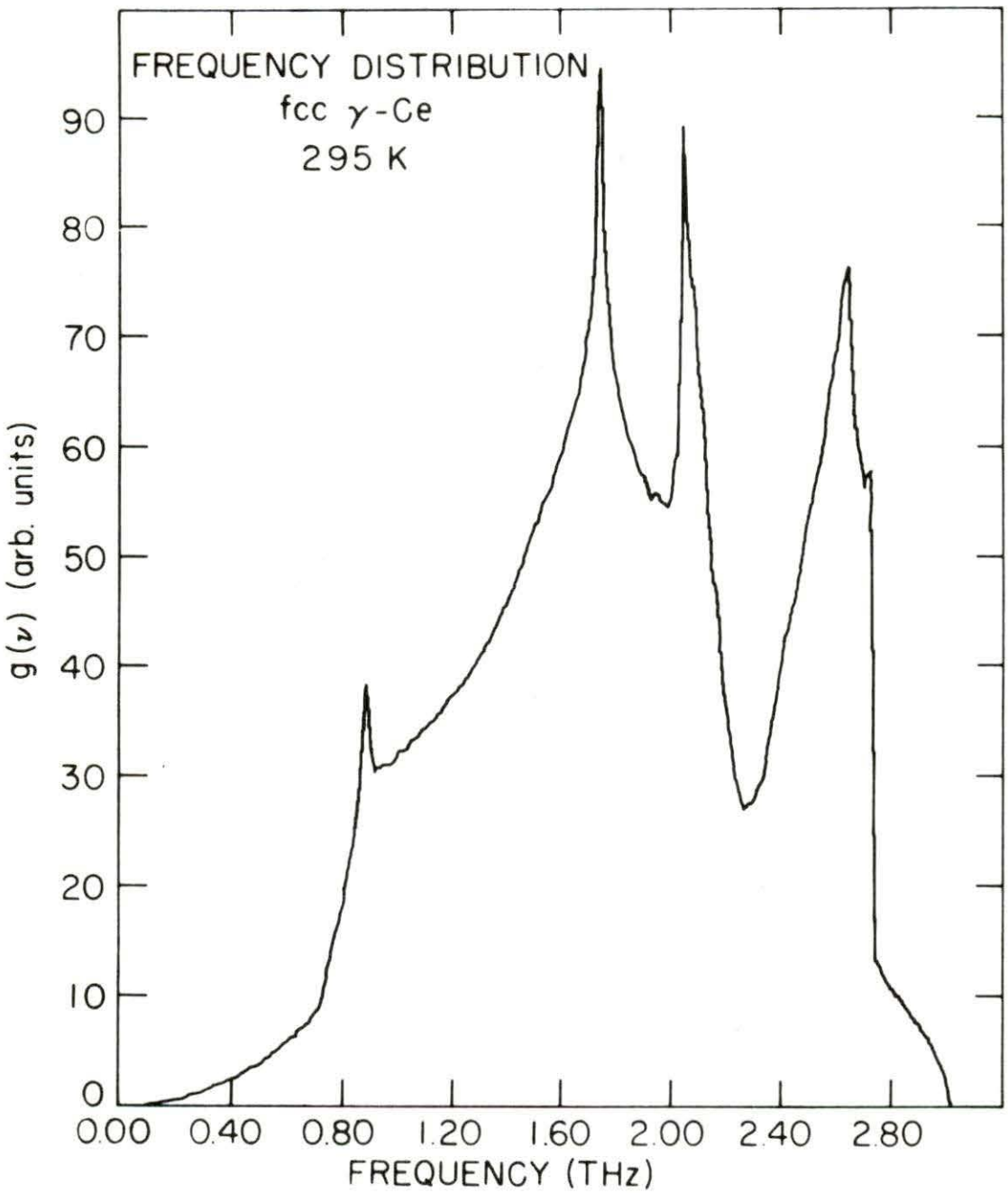

Figure C.6. Density of states calculated from AFC's given by 8NN Fit #2

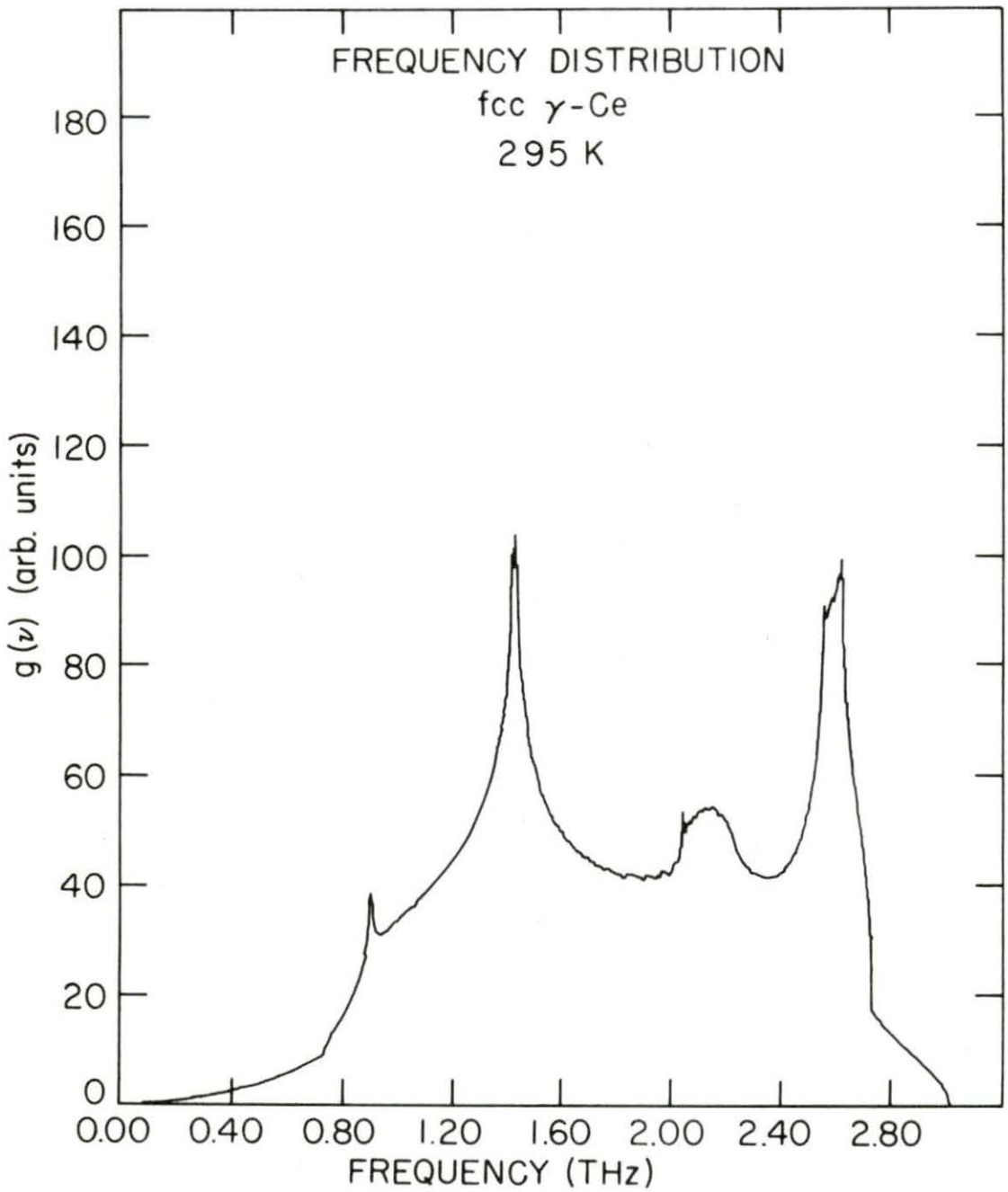

Figure C.7. Density of states calculated from AFC's given by 8NN Fit #3

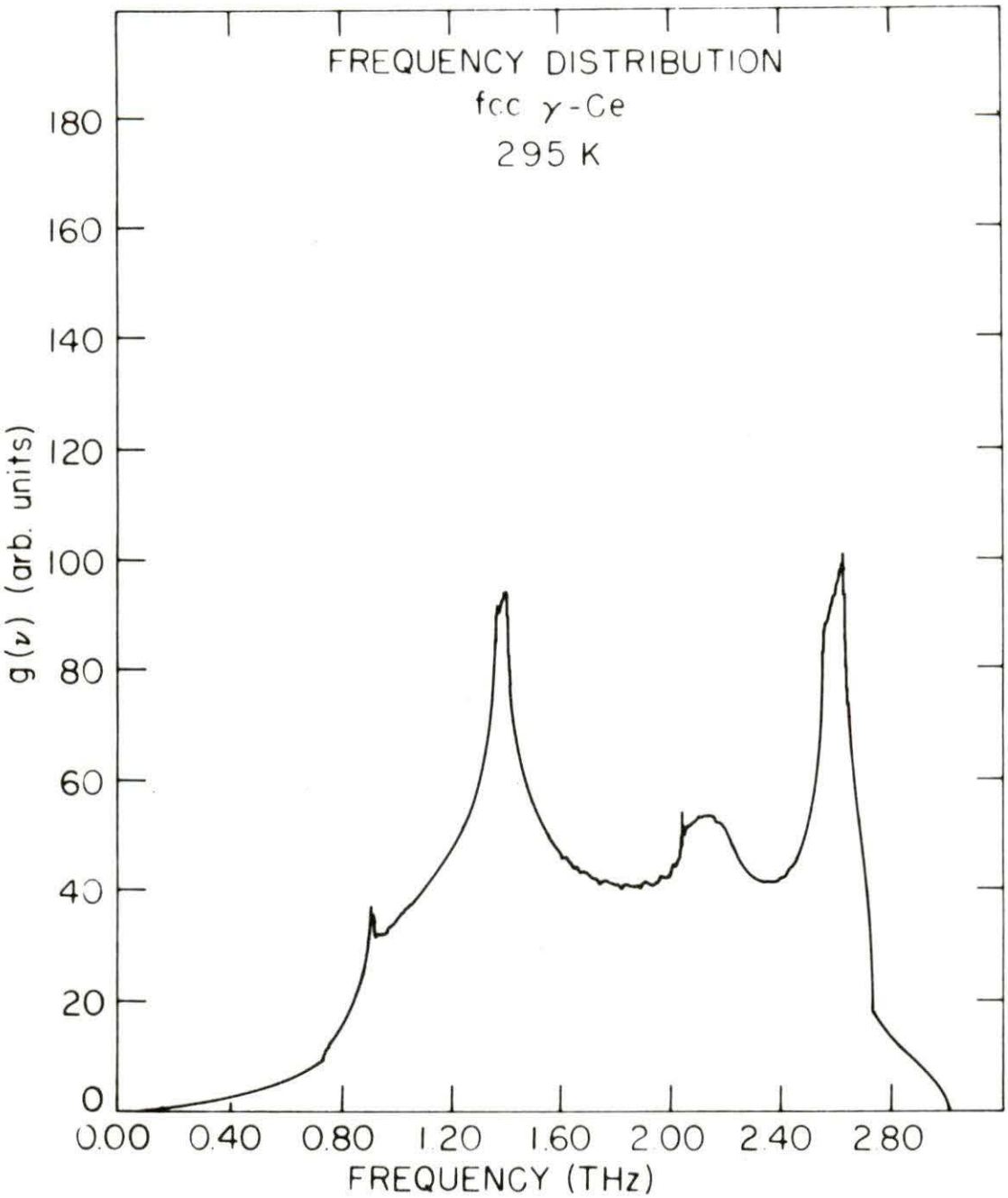

Figure C.8. Density of states calculated from AFC's given by 8NN Fit #4

APPENDIX D

In order to isolate the contribution of magnetic scattering to the total intensity obtained from inelastic neutron scattering measurements, it is necessary to apply an appropriate correction. The correction procedure which has been proposed for the magnetic measurements performed in the present experiment is presented below.

As previously discussed in Chapter I, there are incoherent and coherent contributions to the nuclear scattering cross section for neutrons. Each of these contributions contains terms due to elastic, one-phonon, and multiphonon processes. The contribution of each of these three terms to the differential incoherent cross section is given below in Equation (D.1)[1] (33). A similar expression for the differential coherent cross section is obtained by replacing σ_{incoh} with σ_{coh} in Equation (D.1).

$$\left(\frac{d^2\sigma}{d\Omega dE'}\right)_{incoh} = \frac{N\,\sigma_{incoh}}{4\pi}\,\frac{K'}{K_o}\,e^{-2W(\vec{Q})} \qquad (D.1)$$

$$\times\left[\delta(\hbar\omega) + \frac{\hbar^2 q^2}{2M_k}\,\frac{g(\omega)}{\omega}\,\{1 + n(\omega)\}\right.$$

$$\left. + \frac{1}{\hbar\Delta}\,e^{-\omega/[\Delta^2\,\gamma(0)]}\,F(x,y)\right]$$

---

[1] This equation is obtained in the 'Gaussian' approximation. In general, the scattering intensity becomes more and more dominated by multiphonon processes as the incident energy increases. Therefore, in the 'Gaussian' approximation the multiphonon term in the cross section is given in a form which has the correct asymptotic behavior at high energies.

Reading from left to right in the square brackets, the first term represents the elastic contribution, the next term is the one-phonon contribution, and the last term is the multiphonon contribution to the total incoherent scattering cross section. The various parameters of Equation (D.1) which have not been previously defined in the context of the present work are defined below.

N = number of scattering nuclei

$$\gamma(0) = \frac{4M_k\, W(\vec{Q})}{\hbar q^2}$$

$$\Delta^2 = \frac{4\mathcal{E}}{3\hbar\,\gamma(0)} - \frac{1}{\gamma^2(0)}$$, where $\mathcal{E}$ is the mean kinetic energy per atom given by

$$\mathcal{E} = \frac{3}{2}\int_0^\infty d\omega\; g(\omega)\;\hbar\omega\;\{n(\omega) + \frac{1}{2}\}$$

$$x = \omega/\Delta$$

$$y = 2W\, e^{\left(\frac{-1}{2\Delta^2\,\gamma^2(0)}\right)}$$

$$F(x,y) = \sum_{p=2}^{\infty} \frac{1}{p!(2\pi p)^{\frac{1}{2}}}\; y^p\; e^{\left(\frac{-x^2}{2p}\right)}$$

The elastic contribution to the coherent and incoherent cross sections can be avoided by measuring the scattering at finite energy transfer. For single crystal measurements, the one phonon

contribution can also be avoided by measuring the scattering at "zone center" Q values as previously discussed. Therefore, to correct single crystal magnetic inelastic scattering data for nuclear scattering contributions, one must evaluate only the multiphonon terms of Equation (D.1) and of the corresponding coherent cross section equation. (The function, F(x,y), has been tabulated in Reference (33)).

Knowing the behavior of the multiphonon scattering contribution as a function of Q and energy transfer, one can normalize the background scattering intensity by measuring the scattering intensity at very large Q values. For appropriately large Q values the magnetic form factor is essentially zero (Figure 3.9) so that the magnetic scattering can be neglected. Thus, the total scattering intensity observed at the designated large Q value can be ascribed to multiphonon processes and experimental background.

Therefore, the additional magnetic measurements which will be performed on γ-Ce will complete the experimental curve of Figure 3.11, and provide the above background normalization. An accurate correction will then be applied to all of the magnetic scattering data which have been obtained and a complete analysis of the magnetic scattering of γ-Ce will be performed.

BIBLIOGRAPHY

1. D. C. Koskenmaki and K. A. Gschneidner, Jr., in Handbook on the Physics and Chemistry of Rare Earths, edited by K. A. Gschneidner, Jr. and L. Eyring (North-Holland Publishing Co., Amsterdam, to be published).

2. W. H. Zachariasen and F. H. Ellinger, The Crystal Structures of Cerium Metal at High Pressure, Los Alamos Scientific Laboratory Report No. LA-6251 (1976).

3. F. H. Spedding, J. J. Hanak, and A. H. Dane, J. Less-Common Metals 3, 110 (1961).

4. A. W. Hull, Phys. Rev. 18, 88 (1921).

5. A. W. Lawson and T.-Y. Tang, Phys. Rev. 76, 301 (1949).

6. A. F. Schuch and J. H. Sturdivant, J. Chem. Phys. 18, 145 (1950).

7. C. J. McHargue, H. L. Yakel, Jr., and L. K. Jetter, Acta Cryst. 10, 832 (1957).

8. L. Y. Adams and B. L. Davis, Proc. Nat. Acad. Sci. U.S. 48, 982 (1962).

9. B. J. Beaudry and P. E. Palmer, J. Less-Common Metals 34, 225 (1974).

10. G. E. Bacon, Neutron Diffraction (Oxford University Press, London, 1975).

11. R. Hultgren et al., Selected Values of the Thermodynamic Properties of the Elements (American Society for Metals, Metals Park, Ohio, 1973).

12. C. J. McHargue and H. L. Yakel, Jr., Acta Met. 8, 637 (1960).

13. K. A. Gschneidner, Jr., R. O. Elliot, and R. R. McDonald, J. Phys. Chem. Solids 23, 555 (1962).

14. M. S. Rashid and C. J. Altstetter, Trans. Met. Soc. AIME 236, 1649 (1966).

15. N. T. Panousis and K. A. Gschneidner, Jr., Solid State Commun. 8, 1779 (1974).

16. D. C. Koskimaki, K. A. Gschneidner, Jr., and N. T. Panousis, J. Crystal Growth 22, 225 (1974).

17. K. A. Gschneidner, Jr. and R. Smoluchowski, J. Less-Common Metals 6, 354 (1963).

18. D. R. Gustafson, J. D. McNutt, and L. O. Roellig, Phys. Rev. 183, 435 (1969).

19. O. D. McMasters, G. E. Holland, and K. A. Gschneidner, Jr. (to be published in J. Crystal Growth 44 (1978)).

20. C. Stassis, C.-K. Loong, G. R. Kline, O. D. McMasters, and K. A. Gschneidner, Jr., J. Appl. Phys. 49, 2113 (1978).

21. C. Stassis, Department of Physics, Iowa State University (private communication).

22. M. Born and K. Huang, Dynamical Theory of Crystal Lattices (Oxford University Press, London, 1954).

23. J. M. Ziman, Electrons and Phonons (Oxford University Press, London, 1960).

24. G. V. Chester, Adv. Phys. 10, 357 (1961).

25. B. N. Brockhouse, in Inelastic Scattering of Neutrons by Solids and Liquids (International Atomic Energy Agency, Vienna, 1961).

26. K. E. Larsson, S. Holmrydana, and U. Dahlborg, in Inelastic Scattering of Neturons by Solids and Liquids (International Atomic Energy Agency, Vienna, 1961).

27. C. Stassis, G. L. Kline, W. A. Kamitakahara, and S. K. Sinha, Phys. Rev. B 17, 1130 (1978).

28. L. Brillouin, Wave Propogation in Periodic Structure (Dover Publications, New York, 1953).

29. G. Venkataraman, L. A. Feldkamp, and V. C. Sahni, Dynamics of Perfect Crystals (MIT Press, Cambridge, 1975).

30. M. Lax, Symmetry Principles in Solid State and Molecular Physics (Wiley-Interscience, New York, 1974).

31. B. N. Brockhouse, E. D. Hollman, and S. C. Ng, Atomic Vibrations in Metals and Alloys Studied by Neutron Spectroscopy, AIMME Conf. Proc. (1967).

32. W. M. Lomer and G. G. Low, in Thermal Neutron Scattering, edited by P. A. Egelstaff (Academic Press, New York, 1965).

33. W. Marshall and S. W. Lovesy, Theory of Thermal Neutron Scattering (Oxford University Press, London, 1971).

34. B. Jacrot and T. Riste, in Thermal Neutron Scattering, edited by P. A. Egelstaff (Academic Press, New York, 1965).

35. B. N. Brockhouse, in Phonons in Perfect Lattices and Lattices With Point Imperfections, edited by R. W. H. Stevenson (Oliver and Boyd, London, 1966).

36. A. H. Millhouse and A. Furrer, Solid State Commun. 15, 1303 (1974).

37. B. D. Rainford, B. Buras, and B. Lebech, Physica 86-88B, 41 (1977).

38. S. M. Shapiro, J. D. Axe, R. J. Birgeneau, J. M. Lawrence, and R. D. Parks, Phys. Rev. 16B, 2225 (1977).

39. G. L. Squires, Arkiv För Fysik 25, 21 (1962).

40. G. Dolling and A. D. B. Woods, in Thermal Neutron Scattering, edited by P. A. Egelstaff (Academic Press, New York, 1965).

41. C. Kittel, Introduction to Solid State Physics (Wiley, 4th Ed., New York, 1971).

42. G. Gilat and L. J. Raubenheimer, Phys. Rev. 144, 390 (1966).

43. E. C. Svensson, B. N. Brockhouse, and J. M. Rowe, Phys. Rev. 155, 619 (1967).

44. F. A. Lindemann, Phys. Zeits. 11, 609 (1910).

45. R. A. Reese, S. K. Sinha, and D. T. Peterson, Phys. Rev. 8B, 1332 (1973).

46. F. F. Voronov, L. F. Vereshchagin, and V. A. Goncharova, Dokl. Akad. Nauk SSSR 135, 1104 (1960) [transl.: Sov. Phys.-Doklady 135, 1280 (1960)].

47. M. Rosen, Phys. Rev. 181, 932 (1969).

48. S. M. Shapiro and S. C. Moss, Phys. Rev. 15B, 2726 (1977).

49. M. Rosen, Phys. Rev. Lett. 19, 695 (1967).

50. J. F. Smith, C. E. Carlson, and F. H. Spedding, Trans. AIME 209, 1212 (1957).

51. L. D. Landau and E. M. Lifshitz, Theory of Elasticity (Pergamon Press, New York, 1970).

52. W. Voigt, Lehrbuch der Kristalphysik (Teubner, Leipzig, 1928).

53. A. Reuss, Z. Angew. Math. Mech. 9, 55 (1929).

54. F. Barson, S. Legvold, and F. H. Spedding, Phys. Rev. 105, 418 (1957).

55. F. H. Spedding, J. J. McKeown, and A. H. Daane, J. Phys. Chem. 64, 289 (1960).

56. H. B. Huntington, Solid State Phys. 7, 213 (1958).

57. K. A. Gschneidner, Jr., in Rare Earth Research III, edited by L. Eyring (Gordon and Breach, New York, 1965).

58. S. Arajs and R. V. Colvin, J. Less-Common Metals 4, 159 (1962).

ACKNOWLEDGMENTS

The author wishes to thank Dr. C. Stassis for his tireless guidance and assistance in the course of this work. The author is also indebted to Dr. B. Harmon for many helpful discussions during the analysis of the data and interpretation of results.

Appreciation is extended to Dr. K. A. Gschneidner, Jr. and O. D. McMasters for providing the γ-Ce crystal, and to Ames Laboratory and Oak Ridge National Laboratory for the use of their facilities. The assistance of Dr. R. M. Nicklow of ORNL is also gratefully acknowledged.

Sincere appreciation is given to Lesley Swope for her excellent preparation of the manuscript and Jerel Zarestky for his assistance with the figures.

Finally, the author wishes to express her deepest thanks to her family and her congregation for their unceasing love and support, and to Jesus Christ for his abiding Spirit of strength and assurance, and his abundant love.